Measurement of the very-forward photon production in 13 TeV proton-proton collisions at the LHC

Yuya Makino
Department of Science
Nagoya University

A thesis submitted for the degree of
Doctor of Science

May, 2017

Abstract

A key to resolving the mystery of ultrahigh energy cosmic rays is the measurement of the mass composition by air shower experiments. However, the interpretation of the observed data strongly relies on the choice of the hadronic interaction models used in the air shower simulations to compare with the data. The uncertainty arising from the interaction models has been one of the largest systematic uncertainties in the mass composition measurements.

The Large Hadron Collider forward experiment (LHCf) measures the very forward rapidity region of hadron collisions at the LHC. Since the bulk of the energy flow concentrates on the forward rapidity region, LHCf has the capability to verify the interaction models in the phase space relevant to the air shower development. In particular, at $\sqrt{s}$ =13 TeV, the peak of the energy flow moves forward in the pseudorapidity range covered by LHCf in contrast to previous runs at the LHC owing to Lorentz boost. The detectors, conversely, have to face the serious radiation problem which is expected to be 30 Gy/nb^{-1}. Therefore, we have developed the upgraded LHCf detectors with Gd_2SiO_5 (GSO) scintillator for the 13 TeV collisions. The performance of the upgraded detectors for $\sqrt{s}$ =13 TeV operation is evaluated after the dedicated beam tests in Heavy Ion Accelerator in Chiba (HIMAC) and the CERN Super Proton Synchrotron (SPS) in 2012–2015. Energy and position resolutions of the upgraded LHCf detectors are confirmed to be 3 % and better than 200 μm for 200 GeV photons, respectively, and meet the requirement of the experiment at $\sqrt{s}$ =13 TeV.

In June 2015, LHCf had succeeded to complete the measurement of the proton-proton $\sqrt{s}$ =13 TeV collisions at the LHC with the integrated luminosity of 10 nb^{-1}. The analysis flow of the inclusive photon events is established after the dedicated studies such as the multihit-identification algorithm and the spectrum unfolding. The systematic uncertainty of the spectrum measurement at 13 TeV has been reduced comparing to the previous analysis owing to the dedicated calibration at the SPS.

The measured photon energy spectra at $\eta > 8.52$ are compared with the modern hadronic interaction models widely used in the air shower experiments. The pre/post-LHC models of EPOS, QGSJET and SIBYLL are carefully compared with the measured results. The model predictions of the photon production are examined not only in terms of the energy spectrum but also the pseudorapidity dependence of the energy flow.

Eventually, EPOS-LHC reproduces the best forward rapidity photon production at $\sqrt{s}$ =13 TeV. The results indicate that the difference of the depth of the shower maximum predicted by the models can be explained by model uncertainty in the very forward rapidity photon production. This work remarks that the uncertainty on the mass composition measurement in the air shower experiments is expected to be reduced after further retuning of the hadronic interaction models with the forward photon measurement at $\sqrt{s}$ =13 TeV.

Contents

Chapter 1

Introduction

1.1 Cosmic-rays

Since the beginning of the 20th century, a number of cosmic-ray observations have been revealing the nature of the universe extending the energy higher and higher. The energy spectrum of the cosmic rays observed by several experiments so far is shown in Fig. 1.1. The energy spectrum follows a power-law having the index of -2.7 in perspective. Recent cosmic ray observations have been revealing the detailed features in the spectrum. The spectrum becomes softer at $10^{15.6}$ eV, and this particular region is the so-called *knee* which is associated with the acceleration limit of protons at the astrophysical objects in the galaxy. Supernova remnant (SNR) is a strong candidate for the source of the galactic cosmic rays [2]. While detail mechanism of cosmic-ray acceleration is yet unknown, the maximum energy of the accelerated particle is proportional to rigidity so as to be confined within the source. Therefore, the contribution of galactic cosmic rays continues up to the energy of the acceleration limit of irons at the galactic accelerators [3] known as the *2nd knee* at $10^{17.2}$ eV.

The observations and the associated theories have supported that there is a transition of the contribution in the cosmic-ray spectrum from galactic to extragalactic between the *2nd knee* and the *ankle* at $10^{18.7}$ eV. Among the extragalactic cosmic rays, the ones above approximately 10^{18} eV are called ultrahigh-energy cosmic rays (UHECRs). Only limited number of astrophysical objects with a huge volume and/or the intense magnetic field is considered to have the capability of accelerating particles to UHECRs so far. Despite the decades of efforts from the experimental and the theoretical sides, none of the astrophysical objects including active galactic nuclei (AGN) and gamma-ray bursts (GRBs) has been confirmed as the origin of the UHECRs.

1.1.1 Ultrahigh-energy cosmic rays

The measurement of UHECRs is the probe to understand the most energetic phenomena in the universe. Due to the very small flux, a level of 1 event/km^2/yr above

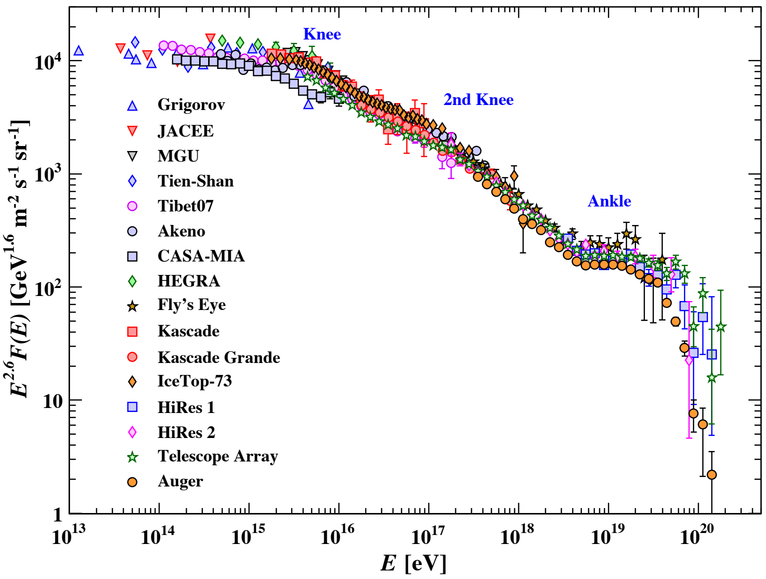

Figure 1.1: Cosmic-ray spectrum observed by several experiments ([1] and references therein).

10^{19} eV, the observation of UHECRs has been developed by large-area air shower arrays such as Akeno Giant Air Shower Array (AGASA) [4] from 1990's. Over the last decade, Telescope Array [5] and Pierre Auger Observatory[6] have been leading the observation of UHECRs with the detection areas of 800 km^2 and 3,000 km^2, respectively. One of the achievements from these experiments is, for instance, confirmation of the suppression of the flux at $10^{19.5}$ eV [7, 8]. Historically the suppression had been predicted by Zatsepin and Kuzmin [9], and Greisen [10] after the discovery of the cosmic microwave background (CMB) [11]. The cross section of the photo-pion production,

$$p + \gamma \rightarrow n + \pi^+ (\text{or} \;\; p + \pi^0), \tag{1.1}$$

increases dramatically up to nearly 500 μb and has a peak around 300 MeV of laboratory beam momentum due to the resonance of $\Delta^+(1232)$ before descending thereafter to 100 μb. The collision energy of the interaction between UHECRs and the CMB photons corresponds to indeed that of the resonance. Therefore, the cosmic rays above certain energy are not able to propagate through the universe without losing their energies. It leads the steep cutoff in the cosmic-ray spectrum observed at the Earth, known as the *GZK cutoff*. There are several astrophysical models to explain the observational results of UHECRs. Information on the mass composition at the highest energy region of cosmic rays is a crucial tool to constrain the existing astrophysical models assuming different acceleration mechanism and scenarios [12].

The precise energy spectra observed by Auger and Telescope Array enable us to start a discussion of the origin of UHECRs. Further understanding of the acceleration mechanism and the origin of UHECRs strongly depends on the reliable mass composition measurement. However, there is an underlying difficulty in the mass composition measurement of air shower experiments.

1.1.2 Mass composition measurement by the air shower experiments

Mass composition measurement in the air shower experiments is performed using the difference of the depth of the shower maximum in the atmosphere depending on the mass number. A parameter, X_{max} [g/cm^2], which represents the depth of the shower maximum is widely used in the air shower experiments so far. In this context, a larger X_{max} corresponds to a deeper shower development. In a simplified picture, the air shower development of nucleus primaries is considered as a superposition of nucleons, each of which carries a part, perhaps equally divided by mass number, of the primary energy. It naturally follows that heavy-primary induced showers have smaller X_{max}, while proton-induced showers with the same primary energy lead larger X_{max}. The difference of the air shower development of proton from iron primaries is demonstrated in Fig. 1.2. Under the condition of equal primary energies, a proton-induced shower shows a clear and deep-penetrating development, whereas a rapid development is observed in an iron-induced shower as shown in Fig. 1.2.

X_{max} is obtained experimentally by Fluorescence Detector (FD) ([5] for example) which observes fluorescence lights induced by charged particles in the air shower. The yield of fluorescence is proportional to the energy deposition of the electromagnetic (EM) component in the air shower which carries 90 % of the primary energy. X_{max} is obtained from the longitudinal profile of the measured dE/dx in the atmosphere. The observed average shower maximum depth $\langle X_{max} \rangle$ at the certain energy range is then compared with the results of the air shower simulations because the mass number is not uniquely determined by given X_{max}. The experiments need an interpretation relied on the air shower simulation to obtain the mass composition of the primaries.

Figure 1.3 shows the mean depth of the shower maximum measured by Telescope Array and Pierre Auger Observatory. The observed $\langle X_{max} \rangle$ at each energy is compared with the MC predictions for pure proton and iron primaries indicated by the lines representing several hadronic interaction models used in the air shower simulations. According to the recent studies from both experiments, Telescope Array states that *"a light, nearly protonic, composition is in good agreement with data"* [14], while Auger states that *"data suggests that the flux of cosmic rays is composed of predominantly light nuclei at around* $10^{18.3}$ eV *and that the fraction of heavy nuclei is increasing up to energies of* $10^{19.6}$ eV*"* [15]. Despite the inconsistent interpretations

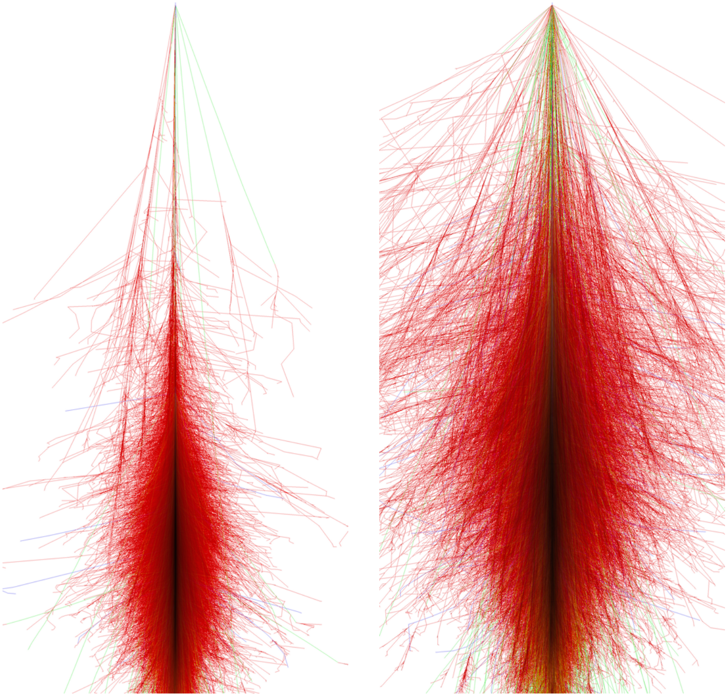
(a) Proton 10^{13} eV (b) Iron 10^{13} eV

Figure 1.2: Composition dependence of the air shower development [13]. a) 10^{13} eV proton primary and b) 10^{13} eV iron primary.

of the data, the working group from Telescope Array and Auger concluded that the data of two experiments are in good agreement within the current uncertainties [16] as shown in Fig. 1.4. The underlying problem on the interpretation of the observed $\langle X_{max} \rangle$ comes from the hadronic interaction models [12]. As is indicated in Fig. 1.3, the interpretation of the $\langle X_{max} \rangle$ strongly depends on the choice of the model to compare with the observed data. In fact, the interpretations of both experiments [14, 15] are based on the different interaction models.

The air shower simulation requires a hadronic interaction model to describe the interactions in the atmosphere. Most of the hadronic interactions induced by cosmic rays and associated secondaries are *soft* interactions where a momentum transfer is small and perturbative-QCD calculation is not applicable. Therefore, the air shower simulation relies on a phenomenological model to calculate the cross section and the particle production in the air shower. Each interaction model provides different predictions of X_{max}, and none of them might be correct. The interaction models used in the air shower experiments have been only tested in the low-energy accelerators, in which the phase space relevant to the air shower development was not fully covered [12].

Further understanding of UHECRs by the air shower experiments depends on the improvement of the interaction models reducing the band of the X_{max} prediction

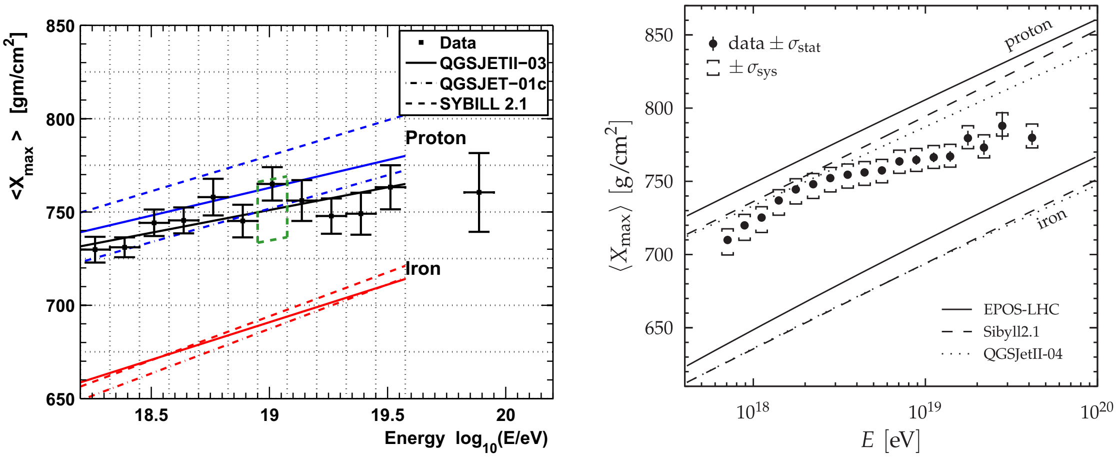

(a) Telescope Array (b) Pierre Auger

Figure 1.3: Mean of X_{max} measured by a) Telescope Array [14] and b) Pierre Auger Observatory [15]. The lines on the top and bottom of the data points denote the model predictions of pure proton and iron, respectively.

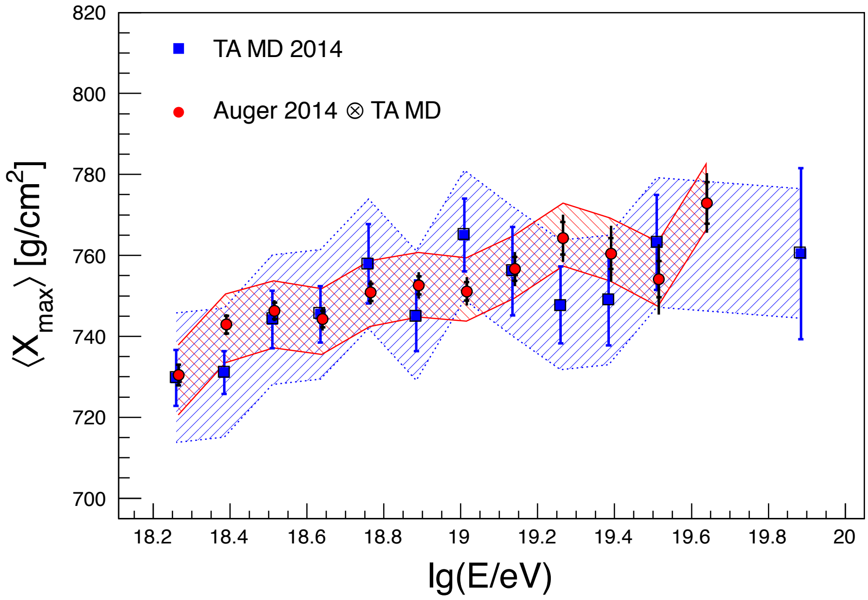

Figure 1.4: Comparison of $\langle X_{max} \rangle$ as measured with Telescope Array and the folded $\langle X_{max} \rangle$ of Auger [16].

bracketed by the models. The interaction models must be tested at the highest energy hadron collider, namely the Large Hadron Collider (LHC) at CERN.

1.2 Hadronic interaction in air shower development

1.2.1 Hadronic interaction models used in the air shower experiments

The hadronic interaction models have been developed with the studies of theories to explain high-energy hadron scatterings at the accelerators. In the early phase, one of the important concepts of the description of hadron scattering was Feynman scaling [18], which states that the invariant cross-section expressed in $x_F = p_l/(\sqrt{s}/2)$ and p_t becomes independent of the collision energy $\sqrt{s}$ at the high energy regime ($s \gg m_p$), where p_l, p_t, and m_p denote longitudinal momentum, transverse momentum, and proton mass, respectively. However the experiments at the Intersecting Storage Rings (ISR) revealed that the violation of the Feynman scaling in rapidity density distribution [19], $1/\sigma\,(d\sigma/d\eta)$ where the pseudorapidity $\eta = -\ln[\tan(\frac{\theta}{2})]$ (θ is a collision angle with respect to the beam axis). The observed cross sections and multiplicities increased with the collision energy.

The minijet model [21, 22] was proposed to give an interpretation to the observed results in ISR and even in air shower experiments which measure higher energy collisions compared to ISR. To explain the rapid increase of the cross section, the theory adopted the concept of second interaction process where individual partons from the colliding hadrons interact each other [20]. Since the minijet model was designed to reproduce the hard interaction, the contribution of the soft hadronic process described in the minijet model was considered to be independent of the energy.

The interaction models widely used in the cosmic-ray experiments recently, EPOS [24], QGSJET [25], SIBYLL [26], and DPMJET [27] are all based on the Gribov-Regge theory [23]. The theory takes a phenomenological approach to describe the soft hadronic process in the high energy. The theory has the capability of reproducing the data results by the energy-dependent behavior of cross sections for the soft processes [20]. There are features in those interaction models for the calculation of the cross-sections and the particle productions. For example, SIBYLL based on the dual-parton model uses the minijet model for the hard interaction unlike the other models, and SIBYLL has the energy-dependent cutoff of the transverse momentum to restrict the calculation of the minijet corss section [26]. EPOS-LHC adopted the parton-based Gribov-Regge theory [29] which allows consistent calculation of the cross-sections and the particle production taking into account the energy conservation [24].

The interaction models used in the last decades, EPOS1.99, QGSJETII-03, and

SIBYLL2.1, for instance, are based on the data before the LHC, such as the results from the colliders up to Tevatron (especially parton density functions at HERA) and the other results from fixed-target experiments and so on. Here we call these models as "pre-LHC" models. There is a considerably large gap between the collision energies achieved by the previous colliders and the UHECRs region.

1.2.2 Post-LHC models

After the tuning of the models with the observed data at the LHC, EPOS-LHC, QGSJETII-04, and SIBYLL2.3 are now available. Those models were calibrated with the measurement at the LHC, such as inelastic cross section and multiplicity and so on. They are the so-called "post-LHC" models. Figure 1.5 shows the inelastic cross section measurements of proton–(anti)proton collisions at the various collision energies and the comparison with the model predictions. The left and right figures represent the measured cross sections compared with the pre-LHC and the post-LHC models, respectively. Very large discrepancies are found among the pre-LHC model predictions, roughly 1.4 times difference between SIBYLL2.1 and EPOS1.99 at $\sqrt{s} = 2 \times 10^5$ GeV which corresponds to 10^{20} eV in the laboratory frame for instance. The inelastic cross section is relevant to the observed X_{max} because it is directly connected to the development of the air shower. Eventually, the discrepancy between the model predictions in the inelastic cross section brings a large uncertainty in the X_{max} [30]. The inelastic cross sections at the LHC energies calculated by the post-LHC models are well tuned with the data as shown in Fig. 1.5. More importantly, they show significantly good agreement at the highest energy after extrapolation. The difference becomes less than 1 % between SIBYLL2.3 and EPOS-LHC at $\sqrt{s} = 2 \times 10^5$ GeV. Another improvement of the model predictions is observed in the multiplicity. Figure 1.6 shows the observed multiplicity at the central pseudorapidity region, $\eta = 0$, with those of the pre/post-LHC models as well as Fig. 1.5. Owing to tuning with the LHC data, uncertainty arising from the model predictions was reduced very much in the UHECR region.

The observed energy dependence of average X_{max}, namely the elongation rate, is again compared with the post-LHC models. Figure 1.7 shows the observed results compared with EPOS-LHC, QGJETII-04, and SIBYLL2.3. In the 10^{18}–10^{20} eV region, agreement of the elongation rate among the post-LHC models is remarkably improved. Especially QGSJETII-03, a pre-LHC version of the QGSJET, had a particularly slower elongation rate along the cosmic-ray energy, but now QGSJETII-04 shows quite similar trend as the other post-LHC models predict. The elongation rates by the post-LHC models demonstrate that the LHC has the capability to reduce the uncertainty of the mass composition measurement of the air shower experiments. However, there is still a discrepancy, approximately 40 g/cm^2 at 10^{20} eV, among the model predictions. As for the post-LHC models, EPOS-LHC, QGSJETII-04, and

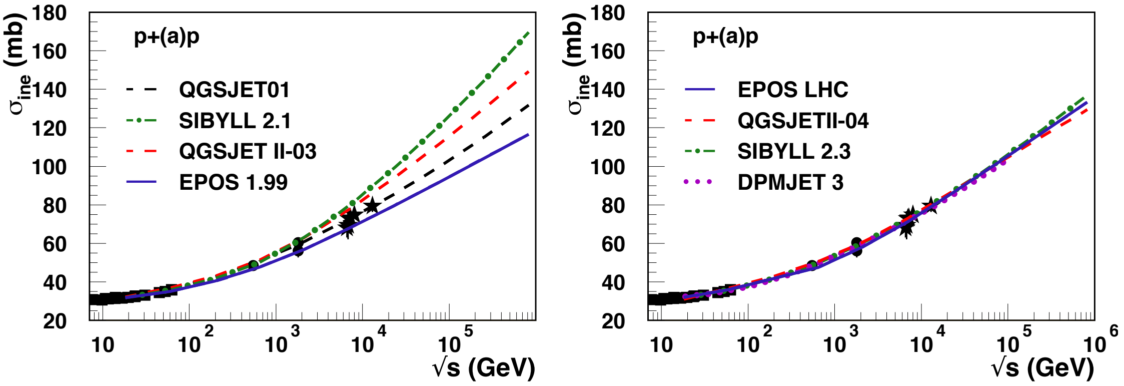

Figure 1.5: Inelastic cross sections of proton–(anti)proton collisions at various collision energies and the comparison with (left) the pre-LHC models and (right) post-LHC models [31].

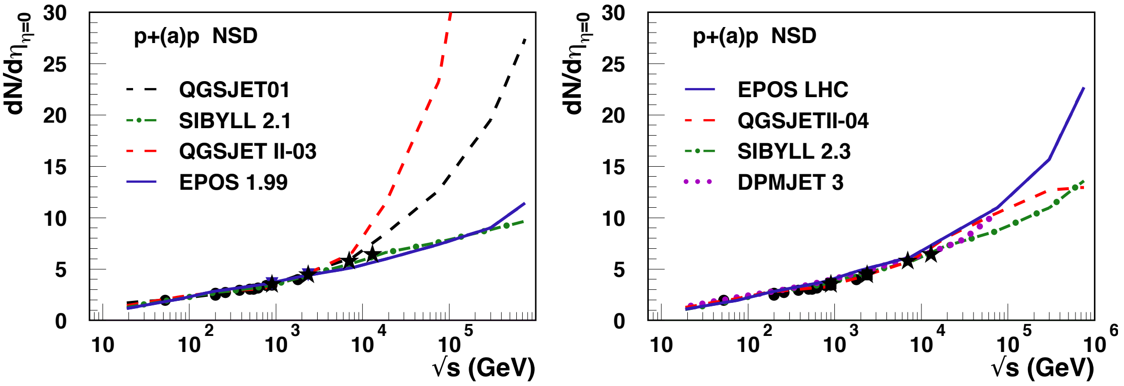

Figure 1.6: Multiplicity of the central pseudorapidity region ($\eta = 0$) of proton–(anti)proton collisions at various collision energies and the comparison with (left) the pre-LHC models and (right) post-LHC models [31].

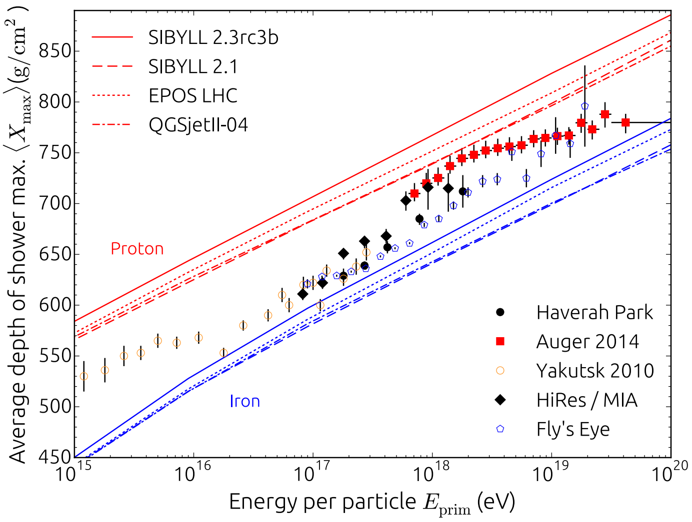

Figure 1.7: Averaged shower maximum by several air shower experiments together with the post-LHC model predictions ([32] and references therein).

SIBYLL2.3 are re-tuned with only the measurement in the central rapidity region. Remaining possibility to reduce the systematic uncertainty of the mass composition measurement is to further investigate the forward rapidity regions of the hadron collisions at the LHC.

1.3 Very-forward measurement at the LHC

1.3.1 Very-forward rapidity region and the air shower development

The forward measurement has an important role in the air shower development. Figure 1.8 shows the pseudorapidity dependence of the multiplicity and the energy flow in p–p $\sqrt{s} = 13$ TeV collisions. In this work, the energy flow is defined as the total energy of the particles generated in the given η region, thus $dE/d\eta$. At the LHC the types of the detectors can be classified as the central detectors ($|\eta| < 5$) such as the ones in the ATLAS [33] and the CMS [34] experiments, the dedicated forward detectors ($5.2 < |\eta| < 6.6$) like the CASTOR calorimeter of the CMS experiment, and the very-forward detectors ($|\eta| > 8.4$) represented by Large Hadron Collider forward (LHCf) [35] and roman pot detectors which measure scattered beam protons. As shown in Fig. 1.8(a), secondary particles generated in a hadron collision concentrate on the central rapidity region, while the multiplicity drastically decreases as $|\eta|$ increases. On the other hand, in Fig. 1.8(b), the energy flow of the secondaries dominates over the forward region, which is interpreted as those particles emitted into the forward regions are the most energetic secondaries in hadron collisions. Accord-

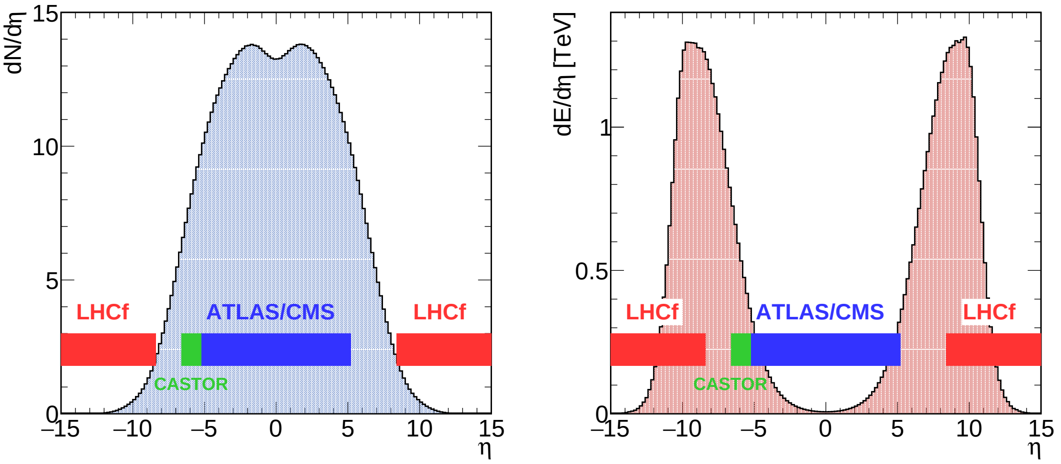

(a) Multiplicity

(b) Energy flow

Figure 1.8: Pseudorapidity dependence of a) the multiplicity and b) the energy flow of the all secondaries at p–p $\sqrt{s} = 13$ TeV collisions. The acceptances of experiments are shown in the bands, in which solid and broken lines in each plot represent all the particles.

ing to the prediction by QGSJETII-04, 53.1% of the total energy flow concentrated on $|\eta| > 8.4$ in p–p $\sqrt{s} = 13$ TeV. The whole air shower development relies on the way the energy is transferred from the primary to secondaries. Therefore, the precise particle production of the interaction models in the phase space where secondaries carry a large fraction of the primary energy is required for the reliable description of the air shower development.

Figure 1.9 shows the fraction of the contribution of the particles emitted in each angle of the initial interaction for a 10^{17} eV proton primary [36]. Each $\Delta\eta$ region represents the acceptances of the experiments at the LHC. The result clearly indicates that the contribution from the very-forward rapidity region dominates the development of the EM component of the air shower owing to the fraction of the carried energy. However, the post-LHC models are re-tuned with the experimental results observed at $|\eta| < 3$ where the data explains only 5 % of the resulting observed paritcles [36]. Therefore, it is necessary to test the models in the very-forward rapidity region.

The relation between the energy flow and the air shower development has been often discussed in terms of *inelasticity* which is the fraction of the primary energy taken by secondaries except for the most energetic secondary particle. Ulrich et al. [30] concluded that the longitudinal development of the air shower depends on cross section and less strongly on inelasticity. If one considers that the air shower observed by FDs is dominantly formed by the EM component which consists of photons (electrons) mainly decayed from π^0, the energy flow into the EM component in a hadron

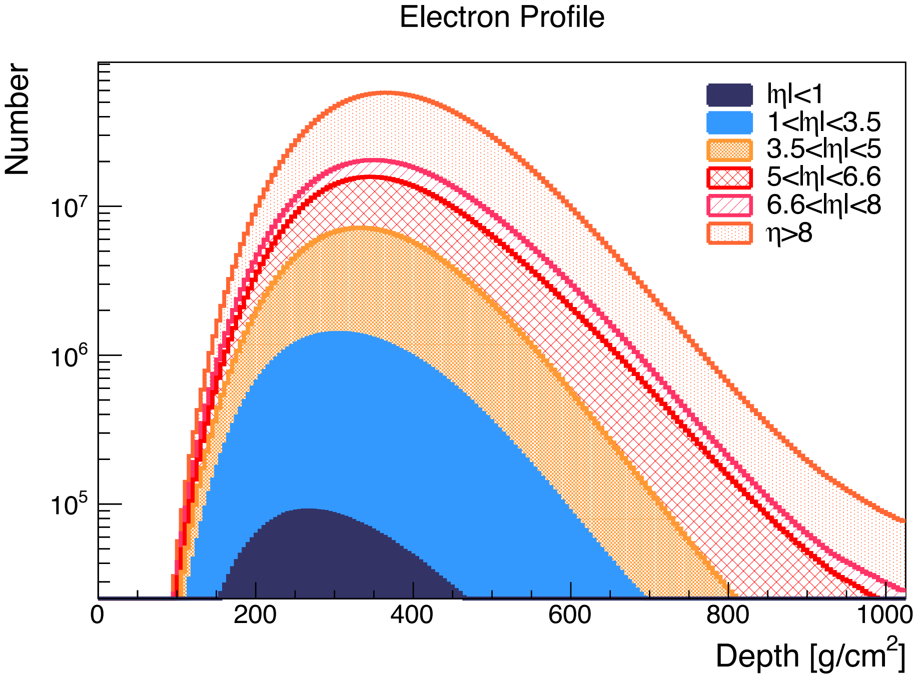

Figure 1.9: Longitudinal profile of number of electrons in a proton-induced air shower with 10^{17} eV primary energy [36]. The fraction of each η range is determined by the contribution of the particles emitted in each angles in the initial inelastic collisions. Pseudorapidity is calculated in the center-of-mass frame of the collision.

collision could be a more sensitive observable rather than inelasticity. Especially we should measure such photon energy flow in the very-forward rapidity region.

1.3.2 The LHCf experiment

The LHCf experiment is the only experiment dedicated for the precise measurement of the EM component in the very-forward rapidity region at the LHC. As for the EM component, the very-forward photon production has been measured by the LHCf experiment so far at $\sqrt{s}$ =0.9 TeV [37] and 7 TeV [38] p–p collisions. The very-forward neutral pion production has been measured at $\sqrt{s}$ = 2.76 TeV, and 7 TeV p–p collisions and $\sqrt{s_{NN}}$ = 5.02 TeV p–Pb collisions [39, 40, 41]. Figure 1.10 shows the inclusive photon spectra measured at $\sqrt{s}$ =0.9 TeV and 7 TeV. The spectra were calculated at $\eta > 10.15$ and $9.46 > \eta > 8.77$ for $\sqrt{s}$ =0.9 TeV, and $\eta > 10.45$ and $8.99 > \eta > 8.81$ for $\sqrt{s}$ =7 TeV collisions The results disfavor hard spectral shapes of DPMJET3.04 [27] and PYTHIA8.145 [28] for both $\sqrt{s}$ =0.9 TeV and 7 TeV. Even the interaction models widely used in the last decade in the air shower experiments, such as QGSJETII-03, EPOS1.99, and SIBYLL2.1 do not reproduce the LHCf data. For instance, QGSJETII-03 predicts overall lower photon yield than the LHCf data for both regions, particularly $8.99 > \eta > 8.81$, in $\sqrt{s}$ =7 TeV. The results conclude that none of the models lies within the errors of the LHCf data over the entire energy range at $\sqrt{s}$ =0.9 TeV and 7 TeV.

The data taken at $\sqrt{s}$ =13 TeV with LHCf gives us a great opportunity for the verification of the interaction models. This is firstly because that the data at $\sqrt{s}$ =13 TeV is capable of verifying the interaction models at the highest collision energy ever, corresponding 10^{17} eV in the laboratory frame. Furthermore, the advantage of the data at $\sqrt{s}$ =13 TeV with LHCf is large detection efficiency of the energy flow. Figure 1.11 shows the photon energy flow distributions at p–p $\sqrt{s}$ = 0.9 TeV, 7 TeV, and 13 TeV by QGSJETII-04. Photon energy flow distributions shift toward higher η as the collision energy increases. In the previous LHCf analyses at $\sqrt{s}$ =0.9 TeV and 7 TeV, photon production at $\eta > 8.77$ and $\eta > 8.81$ have been measured, respectively. With these η acceptances, post-LHC models predict 0.2–0.3 % and 9–10 % of the detection efficiency of the photon energy flow for 0.9 TeV and 7 TeV, respectively. Because of the limitation of the coverage, the analysis focusing on the energy flow has not been studied in the previous collisions. LHCf has completed the measurement in 13 TeV runs at the LHC in 2015 with the acceptance of $\eta > 8.4$ using a dedicated beam condition. The acceptance of the LHCf experiment at 13 TeV runs, $\eta > 8.4$ is indicated by a hashed blue-region in Fig. 1.11. It leads that 26–35 % of the whole photon energy flow in a hadron collision can be covered by the LHCf experiment. Such large coverage of the energy flow in 13 TeV is only possible for the very-forward experiment represented by LHCf because none of the experiments at the LHC covers $8.4 > \eta > 6.6$.

1.3.3 Experimental considerations for the measurement at p–p $\sqrt{s}$ =13 TeV collisions

In order to accomplish the very-forward experiment at p–p $\sqrt{s}$ =13 TeV at the LHC, practically we had to deal with the problems that were not influential in the previous collision energies.

One is the irradiation problem to the detector in such high energy collisions. For instance, comparing to 7 TeV collisions, the irradiation level increases approximately eight times higher, under the same condition of the luminosity. Especially the radiation dose problem is serious for the calorimetric detector locating the very-forward region because the energy flow concentrates there rather than the other η regions as demonstrated in Fig. 1.8(b). Therefore, the LHCf detector for $\sqrt{s}$ =13 TeV must be high radiation tolerance for the precise measurement. Previous studies have proved that the Gd_2SiO_5 (GSO) scintillator is suitable for the detector for $\sqrt{s}$ = 13 TeV collisions from both the radiation hardness and the optical properties [42].

In addition to the radiation problem, the very-forward measurement at p–p $\sqrt{s}$ = 13 TeV is challenging also for the analysis point of view. Despite modest increase of the multiplicity of the secondaries at the central region from the previous collision

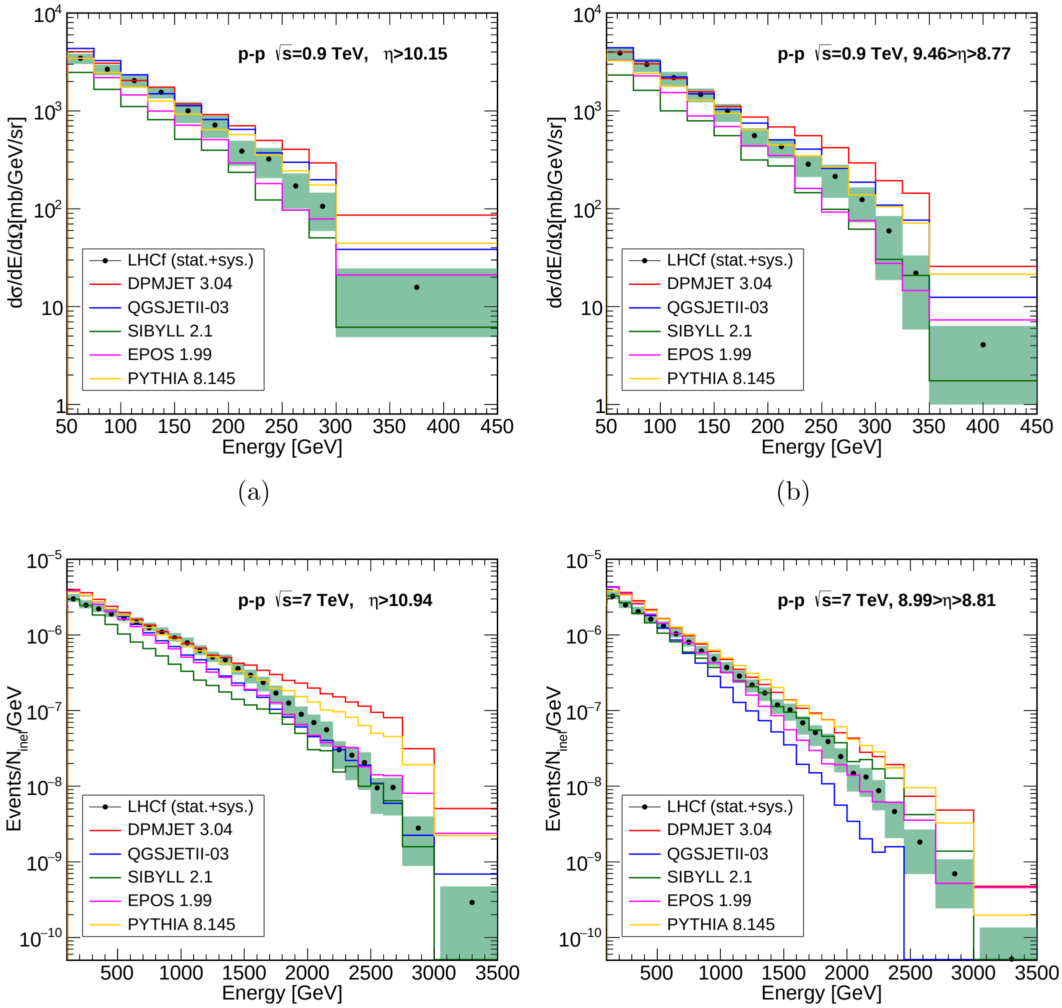

(a) (b)

(c) (d)

Figure 1.10: Photon spectra previously measured by the LHCf experiment. The top plots denote the single photon spectra at a) $\eta > 10.15$ and b) $9.46 > \eta > 8.77$ in p–p $\sqrt{s} = 0.9$ TeV collisions [37], while the bottom plots denote the single photon spectra at c) $\eta > 10.45$ and d) $8.99 > \eta > 8.81$ in p–p $\sqrt{s} = 7$ TeV collisions [38]. The uncertainties arising from the luminosity are not shown on the plots. All plots are revised from the papers, but the changes are only about the appearance.

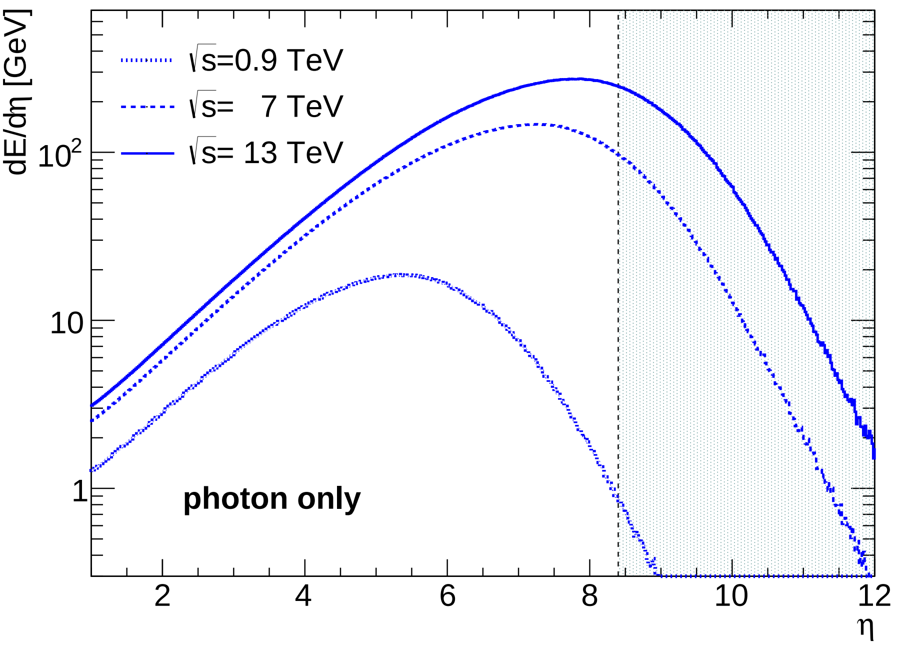

Figure 1.11: Pseudorapidity dependence of the photon energy flow in p–p $\sqrt{s}$ =0.9–13 TeV collisions. The interaction model used here is QGSJETII-04.

energies as shown in Fig. 1.6, Lorentz boost makes the multiplicity in the forward region very high. It implies that a certain fraction of the observed events is expected as multi-hit events where two or more particles enter the detector simultaneously. Multi-hit events have been simply cut in the spectrum calculations in the previous analyses because the contributions of such events were small [37, 38]. In this study, an alternative approach is taken in order to obtain the inclusive photon spectrum without the biases of the analysis nor the detector responses. This is particularly important for the comparison with the model predictions because we do not have to compute the full detector simulations for each interaction models, which usually takes a lot of computing time to obtain statistically-enough data.

1.4 Framework of this thesis

In this thesis, the photon production in the very-forward pseudorapidity region at 13 TeV is verified experimentally in terms of the energy spectrum and the energy flow, and the results are compared with the MC predictions by several hadronic interaction models used in the air shower experiments.

In Chap. 2, the very-forward pseudorapidity measurement with the LHCf experiment is introduced. Firstly the details of the upgraded LHCf detectors with a high-radiation tolerance for p–p $\sqrt{s}$ =13 TeV is explained. In addition to the description of the detector structure, the basic properties of the new sensors used in the upgraded LHCf detectors are explained with the results obtained at beam tests in 2011–2014 using heavy ion beams. We also discuss the reconstruction principle of particle information with the LHCf detectors and η coverage of the LHCf experiment at p–p $\sqrt{s}$ =13 TeV in this chapter.

In Chap. 3, the beam test results of the upgraded LHCf detectors such as the calibration and the performance study for EM shower measurement are discussed. The test was performed with use of 100–250 GeV electron and 150–250 GeV muon beams at the CERN Super Proton Synchrotron in 2015. The upgraded LHCf detectors have been designed to improve radiation tolerance, although the optical properties of GSO are not suitable for the LHCf detectors. Therefore, we have to evaluate all the performance, such as energy and position resolutions, of the upgraded detectors with respective to the requirement for $\sqrt{s}$ =13 TeV. The agreement between the measured detector responses and those of the detector simulation is carefully examined as well.

In Chap. 4, details of the forward measurement with the LHCf detectors at p–p $\sqrt{s}$ =13 TeV at LHC in 2015 are introduced. Inclusive photon spectra at $8.99 > \eta > 8.81$ and $\eta > 10.94$ are calculated, and the obtained spectra are compared with the MC predictions of the various hadronic interaction models. We perform dedicated studies for 13 TeV analysis such as the multi-hit identification algorithm. We estimate systematic uncertainties on the spectrum calculations arising from the detector response, the analysis biases, and the beam conditions during the runs. The spectrum unfolding technique is introduced firstly in the LHCf photon analysis in order to compare the model predictions with the unbiased measured results.

In Chap. 5, the η-acceptance is enlarged from $8.99 > \eta > 8.81$ to $9.22 > \eta > 8.52$ in order to discuss the photon production in terms of the energy-flow. Photon energy flows are calculated by the energy spectra measured at each η region, and the obtained η dependence of the photon energy flow is compared with those of the post-LHC model predictions. We discuss the impact of this work on the UHECR physics in this chapter.

In Chap. 6, the results of this work is summarized.

Chapter 2

The LHCf experiment

2.1 The Large Hadron Collider

The Large Hadron Collider (LHC) [43] is the world's largest hadron collider in CERN, Switzerland. The LHC consists of two circular beam pipes with a circumference of 26.7 km. The LHC and the CERN accelerator complex are designed to accelerate the proton beams up to 7 TeV.

Figure 2.1 shows the CERN accelerator complex in which the proton beams are accelerated in stages to achieve the high energy collision at the LHC. Proton beams injected from the Linac2 are accelerated by the Proton Synchrotron Booster, the Proton Synchrotron, and the Super Proton Synchrotron (SPS) from 50 MeV to 450 GeV. Then, proton beams entering the LHC rings from the SPS are accelerated up to 7 TeV with having "bunch" structures, which are clusters of protons. The bunches of clockwise and counter-clockwise proton beams are designed to collide at the Interaction Points (IPs), which are IP1, IP2, IP5, and IP8. By design, a collision energy reaches $\sqrt{s}$=14 TeV which is equivalent to the interaction of a 10^{17} eV proton and a proton at rest.

2.2 The LHCf experiment

The LHCf experiment [35] measures the very-forward particle production covering $|\eta| > 8.4$ at the LHC since 2009. The LHCf detectors locate at ±140 m from IP1, in which the ATLAS experiment locates at the central rapidity region. LHCf has already reported energy spectra of the forward photons, neutral pions and neutrons at $\sqrt{s}$ = 900 GeV, 2.76 TeV, and 7 TeV p–p collisions and $\sqrt{s_{NN}}$ = 5.02 TeV and 8 TeV p–Pb collisions [37, 38, 39, 40, 41, 44]. The main target of the experiment is the measurement in proton-proton $\sqrt{s}$=13 TeV collisions in 2015.

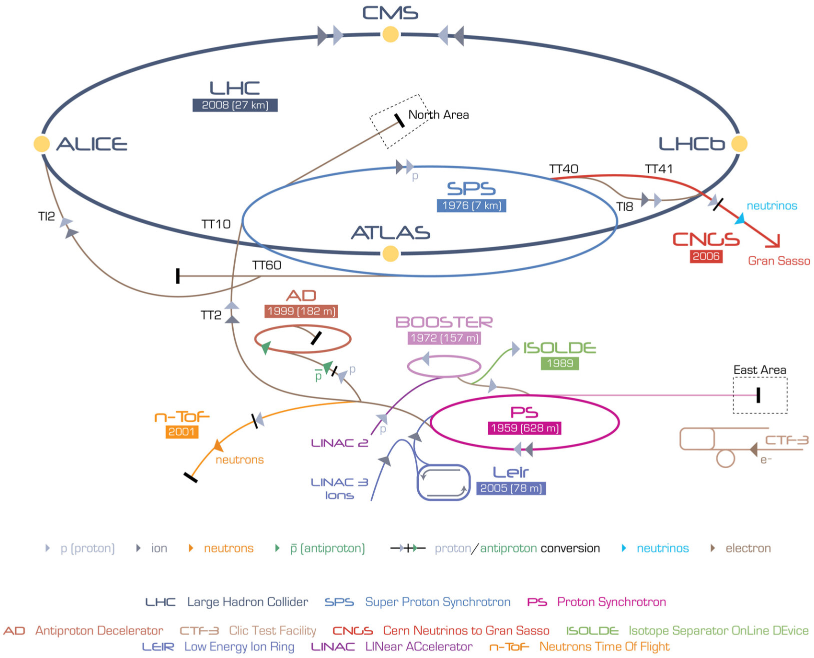

Figure 2.1: The Large Hadron Collider (LHC) and the CERN accelerator complex. The LHCf experiment shares the interaction point with the ATLAS experiment. (Image credit:CERN)

2.3 The upgraded LHCf detectors for pp 13 TeV collisions

2.3.1 Previous detectors and upgrading

The LHCf detectors are sampling and imaging calorimeters using tungsten as the absorber to measure the most energetic secondary particles generated in the hadron collisions. The LHCf detectors measure neutral particles, such as photons and neutrons. Each of two independent detectors, named Arm1 and Arm2, has two calorimeters. The sizes of the calorimeters transverse to the beam direction are 20 mm×20 mm and 40 mm×40 mm in Arm1 and 25 mm×25 mm and 32 mm×32 mm in Arm2.

The previous detectors used before $\sqrt{s} = 13$ TeV p–p collision consist of the plastic scintillators (EJ-260; Eljen Technology) as the sampling layers. The previous Arm1 also used SciFi (SCSF-38; KURARAY) as the shower imaging sensor. It has been estimated that the integrated radiation dose to the calorimeter will be up to approximately 300 Gy after collecting statistically enough data (10 nb^{-1}) in the operation at 13 TeV proton–proton collisions. With this integrated dose, the light yield of EJ-260 immediately starts degrading before finishing the operation. To minimize the degradation due to the radiation effect to the scintillators, Gd_2SiO_5 (GSO; Hitachi Chemical) scintillators have been chosen as the sensors for the new detectors. GSO is known as one of the best inorganic scintillators from the point of view of irradiation tolerance. GSO is able to maintain its light yield up to the radiation of 10^6 Gy [45], whereas that of EJ-260 is 10^2 Gy [35]. In addition, photon yield, the peak emission wavelength, and the decay constant of this scintillator are similar to those of EJ-260; therefore, the modification of the readout system is minimized. The properties of the GSO scintillator have been tested by the accelerator with heavy ion beams at the Heavy Ion Medical Accelerator in Chiba (HIMAC) and confirmed that GSO meets our requirements. The details of these tests are reported elsewhere [42].

2.3.2 The upgraded detectors

Although the basic design of the calorimeter, including 16 sampling layers and four position-sensitive layers interleaved in the tungsten absorbers is not changed, each component has been replaced with the one which consists of the GSO scintillator. As the imaging layers, the GSO-bars are also used [46]. Position-sensitive layers for Arm2, the silicon strip sensors are also upgraded: the bonding scheme of the microstrips is changed to reduce the signal pulse height and avoid saturation of the front-end electronics with the higher energy deposit expected at 13 TeV; furthermore, the longitudinal configuration inside a calorimeter is changed to improve the performance of the EM shower measurement. Figures 2.2 and 2.3 show the longitudinal structure of the calorimeters and the pictures during the construction, respectively. The first half part of the calorimeter is mainly used for the measurement of the EM shower development with use of the sampling layers prepared at every two radiation lengths (X_0). On the other hand, the sampling step for the layers deeper than the 12th is equipped every 4 X_0. The total radiation length of the calorimeter is 44 X_0, thus the EM showers stop their development in the middle of the calorimeter. The calorimeters are designed especially for the EM shower measurement. With this configuration, the measured energy deposition in the calorimeter reaches about 3 % of the incident energy for photons above 100 GeV.

2.3.3 The GSO-plate layers

The 16 layers of GSO-plate are sandwiched in a calorimeter tower as the sampling layer. Each layer of the GSO-plate consists of a GSO scintillator with 1 mm thickness. Each scintillator tile is covered with a reflecting film (Enhanced Specular Reflector; 3M). The emitted light from the scintillator is collected by a quartz light guide attached at a side of the scintillator and read out by the photomultiplier tube (PMT, HAMAMATSU R7400) via acrylic clear optical fibers. The scintillator, the light guide, and the optical fibers are coupled with the optical cement. The GSO-plate layers are supported with an acrylic holders. A sketch of the GSO-plate layers is shown in Fig. 2.4. Since the light guide is attached to one side of the scintillator, it

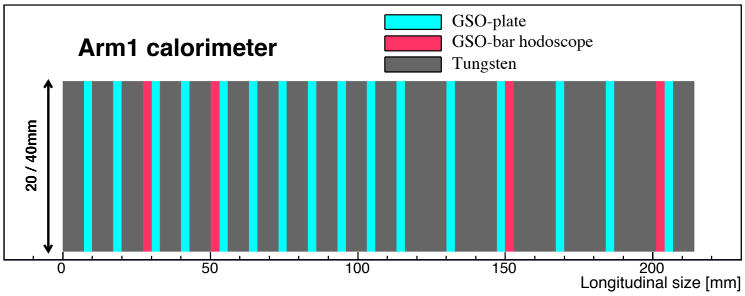

(a) Arm1

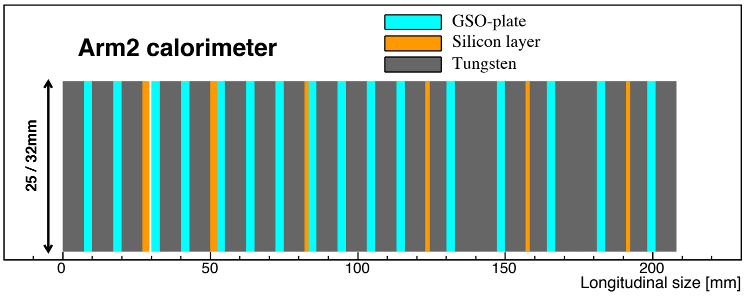

(b) Arm2

Figure 2.2: The longitudinal structure of the LHCf calorimeters. In both figures, grey and light blue parts represent tungsten and GSO-plate layers, respectively. GSO-bar hodoscope for Arm1 and the silicon strip detector for Arm2 are shown in red and orange, respectively. Particles enter from the left side of each figure.

(a) Arm1 (b) Arm2

Figure 2.3: The photos of Arm1 and Arm2 detectors. Side panels and readout cables are not attached in these figures for the appearance. The Arm2 detector is lying sideways.

causes position dependence of the light collection efficiency. Especially, in the case of the Arm1 40 mm calorimeter, read out the light guide and fibers are attached with a certain angle due to the constraint of space of the detector housing. The properties of the position dependence of the light yield of all layers have to be understood based on the experimental data as discussed in Sec.2.6.1.

2.3.4 The GSO-bar hodoscope

The upgraded Arm1 detector has four layers of the GSO-bar hodoscope which enable us to measure the lateral distribution of the shower particles. The GSO-bar, bar-shape GSO scintillator, has dimensions of the cross-section of 1 mm×1 mm and the length of 20 mm or 40 mm depending on the calorimeter tower. The GSO-bar is not covered with any coatings or cladding materials [46]. One layer of the GSO-bar hodoscope consists of two orthogonally aligned belts. Each belt consists of 20 GSO-bars with 20 mm length and 40 GSO-bars with 40 mm length for the 20 mm and 40 mm calorimeters, respectively as shown in Fig. 2.5. The GSO-bar belts are covered by mirror-like optical enhancement film (enhanced specular reflector, 3M Company) to screen two belts optically, and are packed in a black acrylic holder. The signals from the four layers of the GSO-bar hodoscopes with 480 channels are read out by eight PMTs with 64-anode sections (HAMAMATSU H7546, hereafter MAPMT) through 0.71 mm diameter silica-fuzed optical fibers. It is important to mention

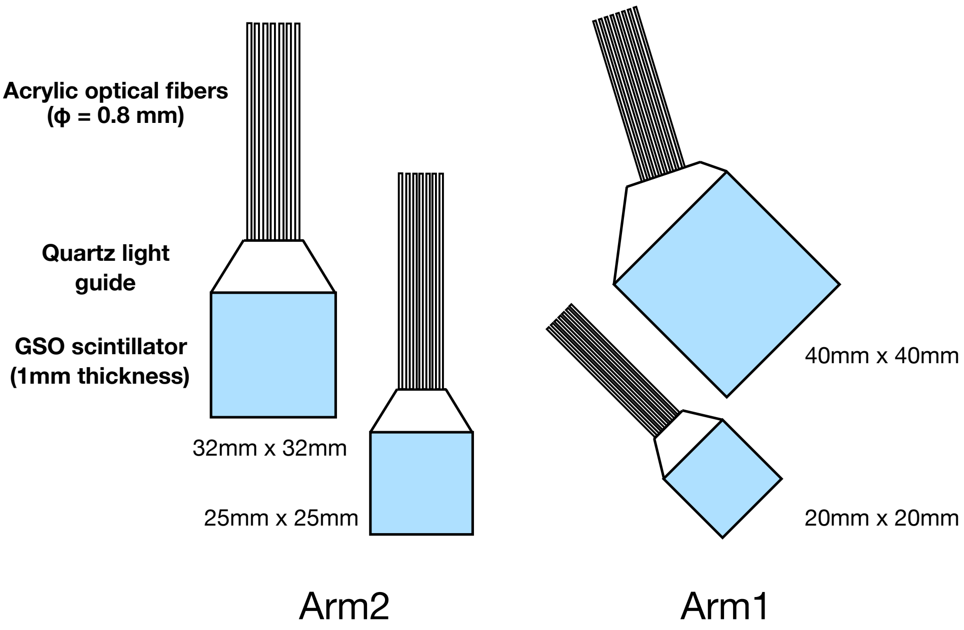

Figure 2.4: A sketch of GSO-plate layers. Because of the constraint of the detector width, read-out light guide and fibers of Arm1 large tower are not attached perpendicular to a side of the scintillator.

that each GSO-bar in the bundle structure is not screened optically. Consequently, crosstalk effect among adjacent channels is inevitable. Details of the crosstalk effect are discussed in Sec. 2.6.2. The configuration of the four layers of GSO-bar hodoscope, placed in 6, 10, 30 and 42 X_0, is optimized for the EM and the hadron shower measurements. Two layers are located at the earlier position of the calorimeter where EM showers develop and the others are located in the deeper positions. A GSO-bar hodoscope layer before the assembly of the Arm1 detector is shown in Fig. 2.6.

Considering the radiation hardness of the silicon detector, we have decided to keep the silicon strip detector [48] as the position sensitive layer for Arm2 for the upgrade of the detector. A plane of silicon detector consists of the strips with 80 μm-pitch and the surface area of 64 mm × 64 mm, which covers all the calorimeter area of the Arm2 detector. Despite 80 μm of the pitch, only every other channels are used to reduce the data size. The position resolution of the silicon strip detector for the EM showers has been found to be 50 μm by the accelerator test.

2.4 Zero-degree measurement at the LHC

2.4.1 Experiment at the TAN

Figure 2.7 shows the geometry of the IP1 at the LHC. The LHCf detectors locate at ±140 m away from the interaction point. The Arm1 and Arm2 detectors are installed

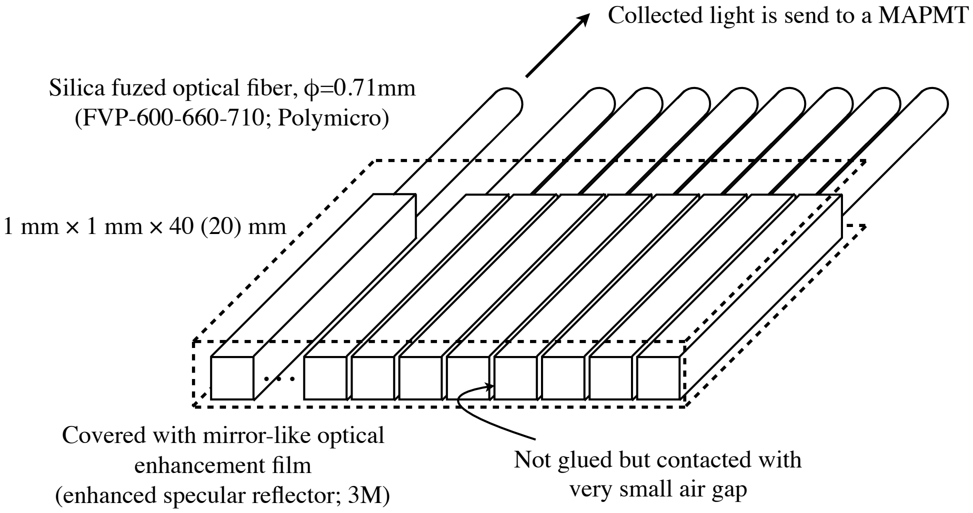

Figure 2.5: Schematic view of a belt structure of the GSO-bar hodoscope. The GSO-bars are not coated and aligned without any glue, but contacted with thin air gap. The belt of GSO-bars is covered with a mirror-like optical enhancement film.

Figure 2.6: A completed one layer of the GSO-bar hodoscope. Fibers from the GSO-bars are bundled with epoxy glue.

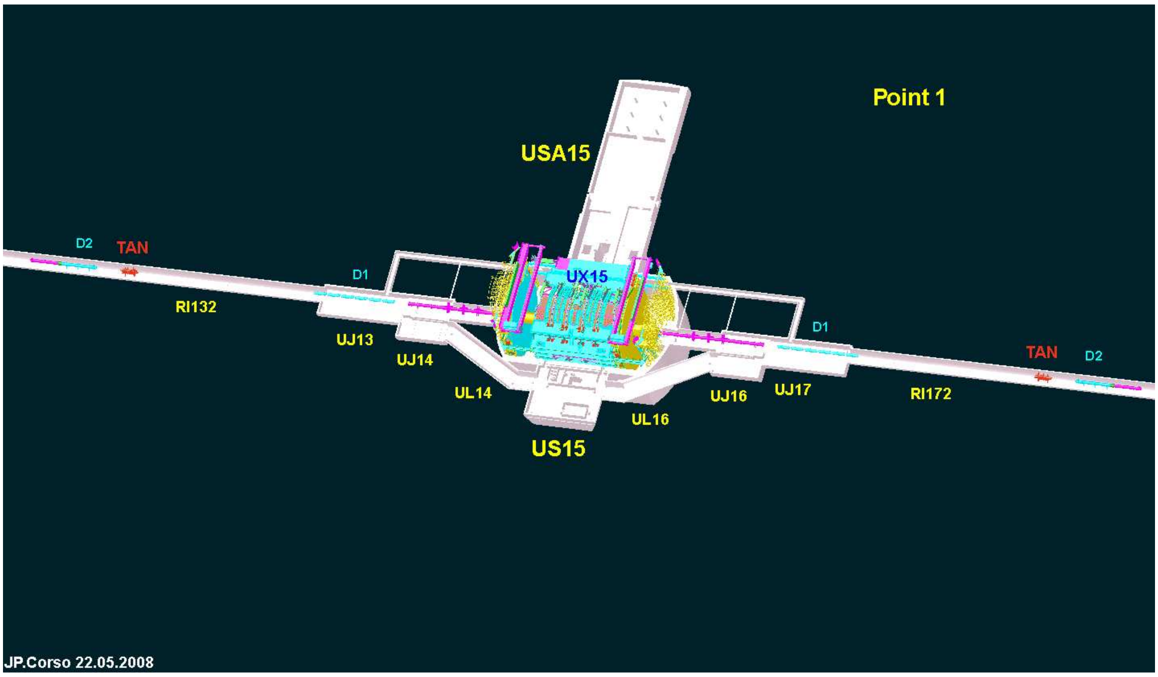

Figure 2.7: Geometry of the IP1 at the LHC. The structure locating at the center is the ATLAS detector surrounding the interaction point mostly. The LHCf detectors are installed inside the TAN, locating either side of 140 m from the interaction point, indicated in red.

in the TANs at the R132 and R172 sections, respectively. Beams collide at the center of the Fig. 2.7, where the ATLAS detector covers large fraction of the phase space of scattered particles.

The LHCf detectors are installed in the experimental slots, which are the gaps between the beam pipes in the TANs. Figure 2.8 shows the sketch of the detectors and the structures inside the TAN, and the installation of the Arm1 detector in the TAN slot in December 2014. The detectors locating at the experimental slots of the TAN are able to measure the neutral particles emitted into the zero-degree in hadron collisions, while charged particles are swept away due to the dipole magnet between the interaction point and the TAN.

2.4.2 Analog signal handling

Considering the radiation damages to the DAQ systems at the TAN, most of digitization processes are performed at the counting room (USA15) adjacent to the interaction point as shown in Fig. 2.7. Communications, such as signal receiving or triggering, have to be performed through 200 m cables connecting the detectors at the TAN region and the counting room in USA15.

The signals from the PMTs of the detector are firstly amplified (×4.8) at the TAN region before being sent them via 200 m cables. After reaching to the counting

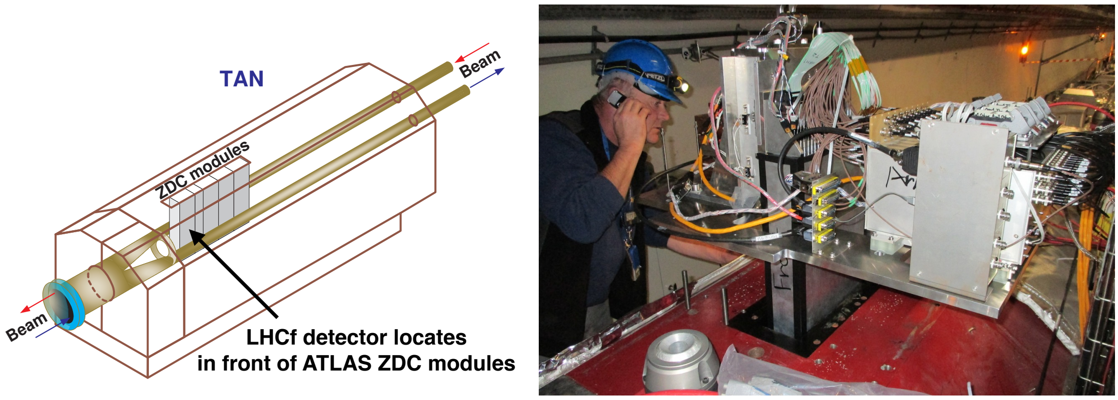

(a) TAN (b) LHCf Arm1 being installed into the TAN slot

Figure 2.8: a) The beam pipe configuration at the TAN ([47], partially revised by the author) and b) the LHCf Arm1 detector being installed into the experimental slot of the TAN.

lack at USA15, the signals enter the linear fanout modules with two output channels (N-SE820; Technoland) providing signals amplified by the factor of one or four. The amplified signals are fed to the low-pass filter with a cut-off at 100 MHz before entering the discriminator module (V814; CAEN). The hit signal of each sampling layer is generated if the signal height is above the pre-determined threshold level of 13 mV for all channels. Hit information of all channels is registered in the logic boards (V1495; CAEN and GPIO GN0324; GND), which are synchronized with the 40 MHz clock provided by the LHC to trigger the data recording. The other signals, which are not amplified by the fanout modules, are digitized by the QDC boards (V965, CAEN) with 12 bits in two different dynamic ranges, 0.2 and 0.025 pC/ADC counts. More details can be found elsewhere [35]. The front-end PCs and the readout/logic modules communicate each other through the VME-PC bus interface (Bit3; SBS Technologies).

2.4.3 Trigger system

The data acquisition of the LHCf experiment is triggered by a shower-like signal detected by the calorimeters synchronized with the beam timing signal provided by the LHC machine. The LHC has the beam pick-up detectors locating 170 m at both sides of each interaction point, which send the beam timing signals (BPTX) to the experiments. The revolution frequency (11 kHz) and the filling scheme of the beams determine the rate of BPTX. The BPTX signals provided by the LHC are used as the first level trigger (L1T) of the LHCf experiment. The secondaries generated in a p–p 13 TeV inelastic collision enter either of the detectors with a probability of 15 %. If either of the calorimeter detects a shower-like signal which coincides with L1T, the system issues the second level trigger (L2T). Here shower-like signal is defined as the

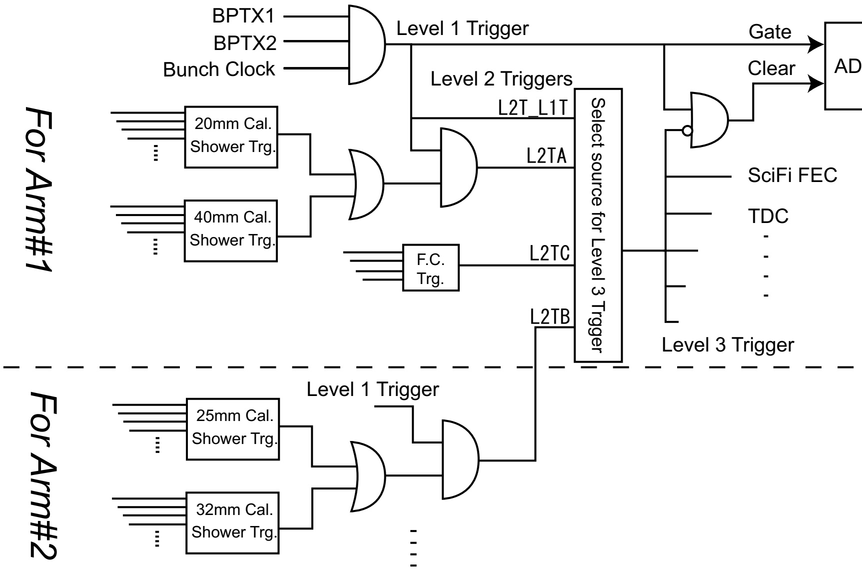

Figure 2.9: The schematic diagram of the DAQ system at the LHC.

events having three successive sampling-layers with signals above the thresholds in the calorimeter. The detection efficiency of the detector for photon events depends on the noise level of each channel, and eventually is 100 % above 200 GeV photons in the case of p–p 13TeV collisions. More details can be found in Chap. 4. L2T trigger generates the third level trigger (L3T) which starts the data recording of the event unless the readout system is busy. The DAQ speed is limited by the data recording of the position-sensitive layers which have large number of channels to read. The maximum DAQ rate of the Arm1 detector is approximately 1 kHz. All the DAQ system is controlled by Maximum Integration Data Acquisition System (MIDAS) [49], and the more detailed configuration can be found in [35]. The DAQ is remotely operated from the control room on the ground level of IP1.

2.4.4 Detector coverage

Locating the detectors in the experimental slots of the TAN provides us an unique opportunity to measure the very forward particles of hadron scatterings including the zero-degree. The obstruction of mechanical structures between detectors and the interaction point limits the lower side of η-acceptance of LHCf.

Figure. 2.10 shows the cross-sections at each detector positions. In both figures, squares filled with grey represent the cross-section of calorimeters of Arm1 and Arm2. Stars locating at the centers of both pictures denote a beam center which is zero-degree of the hadron scattering. Lower side of the η-acceptance is limited by the projection of the elliptical vacuum pipes around the dipole magnets at the TAN shown in the blue circles in the figures. The LHC has the capability to collide beams with vertical "crossing angle". It results in the shift of the beam center at the TAN position, 140 m away from the interaction point. Thus the η-acceptance of LHCf detectors can be extended in such case. For 13 TeV operation, beams collide with a crossing angle of 145 μrad, resulting shift of the beam center by 20.45 mm downward at the TAN. Since the LHCf detectors can be moved vertically by a manipulator controlled remotely, the detector vertical positions are adjusted to locate the beam center at the centers of smaller calorimeters of Arm1 and Arm2. By this configuration, LHCf is able to measure the secondary neutral particles in pseudorapidity range of $\eta > 8.4$.

2.5 Reconstruction methods

Before discussing details of the calibration and the performance studies, we briefly introduce the photon reconstruction methods of the LHCf calorimeters and the calibration coefficients to be determined in the further section.

The incident energy, E, of a particle entering the calorimeter is calculated by the summation of the energy deposited in the calorimeter, S, as

$$E = J(S), \tag{2.1}$$

where J represents a conversion function which is determined by the detector simulation. J is a nearly linear function within the energy range of the LHCf experiment. The summation of the energy deposited in the calorimeter is defined as

$$S = \sum_{i=2}^{13} dE_i \, d_i \, \lambda_i, \tag{2.2}$$

where dE_i is the energy deposition at the i-th sampling layer. Only the energy depositions of the limited layers, from the 2nd to the 13th, are integrated because the contributions of the other layers are negligible. Coefficients d_i represent difference in the sampling steps, which are two and four radiation lengths for earlier and deeper layers, respectively, as illustrated in Fig. 2.2. $d_i = 1$ for i from 1 to 11 and $d_i = 2$ for the other deeper layers. Since the analog signals are sent to the counting room via 200 m coaxial cables, attenuation of the signals must be taken into account in the energy measurement. The attenuation correction factor λ_i is associated with the length of the cable, which varies depending on the channels. Here the energy deposited at each layer is given by

$$dE_i = \frac{1}{F_i(x, y)} C_i \, q_i \tag{2.3}$$

where C_i is the conversion factor by which measured charge q_i is converted to the energy deposition. Nonuniformity of the light collection and the geometrical shower

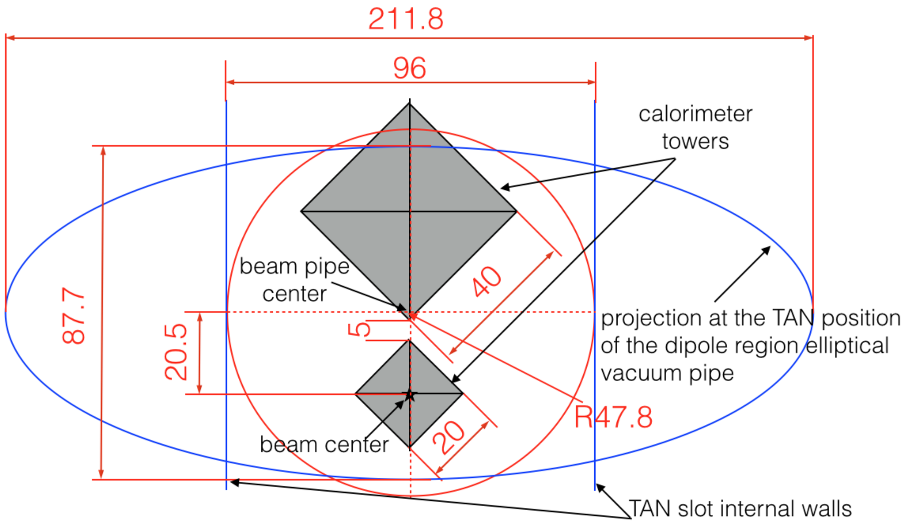

(a) Arm1 side

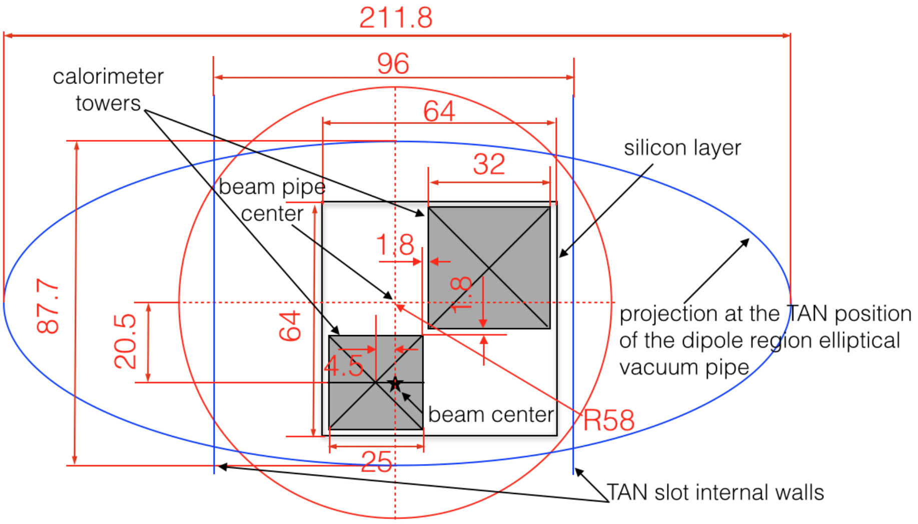

(b) Arm2 side

Figure 2.10: Cross-section at the detector positions and projections of the beam pipe and relating materials for a) Arm1 and b) Arm2. Here vertical crossing angle of 145 μrad is assumed.

leakage effects of the GSO-plate layers are corrected simultaneously according to the reconstructed hit position x and y. $F(x, y)$ is introduced in Sec. 2.6.1, and is energy independent within our requirement. Overall calibration, the measurements of C_i and λ_i, and the performance of the energy reconstruction for EM showers are discussed in Sec. 3.2.

The incident position of the incoming particle, x and y, in Eq.2.3 of Arm1 is calculated by the lateral shower distributions observed at each layer of the GSO-bar hodoscope. The energy depositions of the GSO-bar hodoscope are calculated as

$$\begin{pmatrix} dE_1 \\ \vdots \\ dE_j \\ \vdots \\ dE_N \end{pmatrix} = \Gamma \begin{pmatrix} C_1^{\text{GSO-bar}} \, q_1 \\ \vdots \\ C_j^{\text{GSO-bar}} \, q_j \\ \vdots \\ C_N^{\text{GSO-bar}} \, q_N \end{pmatrix}, \tag{2.4}$$

where q_j and dE_j are the measured charge information and the energy deposited in j-th channel of the GSO-bar hodoscope, respectively. The range of j is $1 \leq j \leq 20(40)$ for the 20(40) mm calorimeter. Γ denotes the correction matrix for the crosstalk effect as discussed in Sec.2.3.4 and $C_j^{\text{GSO-bar}}$ represent the conversion factors for each channel of the GSO-bar hodoscope. In Eq.2.4, subscripts for types of the calorimeter tower (20/40mm), the layer number (1–4), the direction (x/y) are not shown for simplicity. Therefore, we have to determine $C_j^{\text{GSO-bar}}$ of 480 channels in the beam test. The absolute calibration of the GSO-bar hodoscope and its shower imaging performance are discussed in Sec. 3.2.2 and 3.3.3.

2.6 Beam tests in HIMAC

Properties and the basic performance of the new sensors, GSO-plate and GSO-bar hodoscope are tested at Heavy Ion Medical Accelerator in Chiba (HIMAC). Nonuniformity of light yield is measured in November 2011 for Arm1 and July 2013 for Arm2. Measurement of the crosstalk effect of GSO-bar hodoscope is performed in June 2012 and February 2014. In these beam tests, 400 MeV per nucleon carbon beams are used in order to obtain a large amount of energy deposits, 44 MeV for 1 mm thickness of GSO in each of channel. Carbon beams are collimated in diameter of 3 mm with the aluminum collimator. Tungsten layers in the calorimeter towers are removed to avoid cascade showers and fragmentations in such a way as to obtain calibration data for the light collection efficiency depending on the incident position of the incoming particles for all GSO-plate layers. The setup of HIMAC beam tests is shown in Fig. 2.11. A two-axis movable table attached the detector enable us to

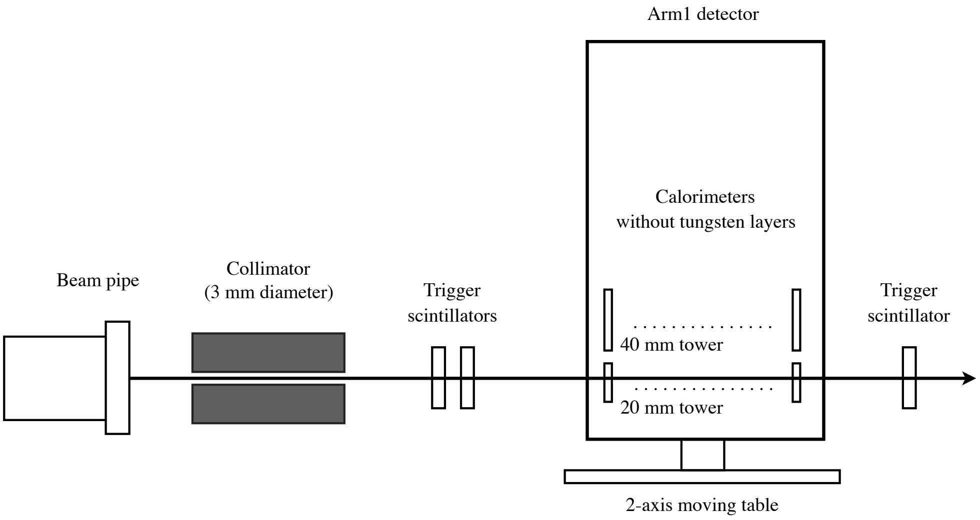

Figure 2.11: Experimental setup of the HIMAC beam test in June 2012 for Arm1. Beams exiting from the beam pipe end are collimated into a diameter of 3 mm. Tungsten absorbers in the calorimeter towers are removed to let particles penetrate the calorimeter towers. The detector is attached with a two-axis movable table to scan all the calorimeter surface.

expose the beams to all the detective area of the calorimeters. Although we have done several beam tests in HIMAC, set-ups are essentially same.

2.6.1 Position dependence of the light collection of the GSO-plate layers

The position dependence of the light yield are determined experimentally in the HIMAC beam tests. Figure 2.12(a) shows the measured collection efficiency map of the 5th layer of the Arm1 40 mm calorimeter. Here the position dependence is observed as ±30 % relative to the center of the calorimeter. To correct the position dependence of measured energy deposit, the convolution of nonuniformity of the light collection and the lateral spread of the cascade shower is required. Thus the obtained nonuniformity maps of the light yield observed in Fig. 2.12(a) are included in the detector simulation. The response maps, where the nonuniformity of the light collection and the lateral spread of showers are included, are obtained by performing the simulation with 10^6 events of 150 GeV electrons exposing both of the calorimeters in Arm1. Figure 2.12(b) represents the response map for a cascade shower in the 5th layer of Arm1 large tower as an example. The measured energy deposition is expected to be smaller due to the “geometrical shower leakage effect” when the incident position is close to the edge of the calorimeter. This is because a part of particles in a shower exits the calorimeters. The response map shown in Fig. 2.12(b) basically follows the feature expected by the shower leakage effect, but the clear position dependence owing to

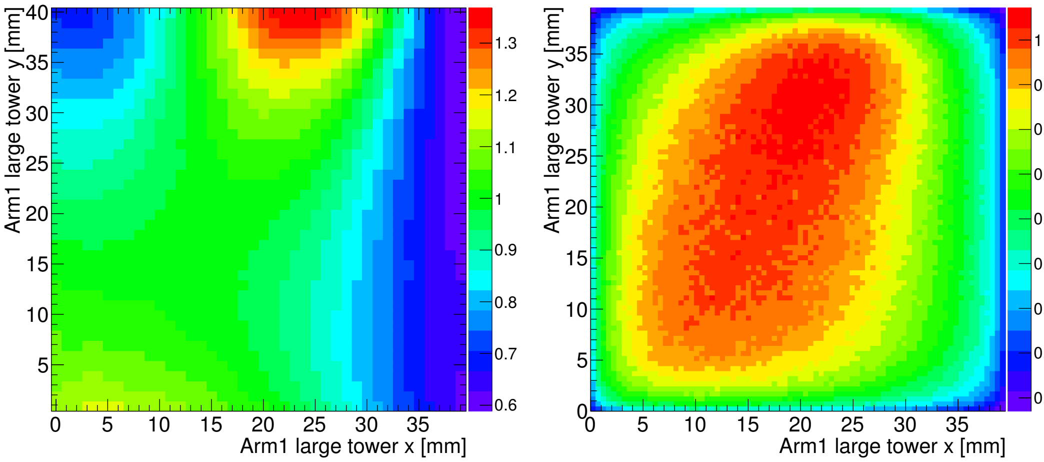

(a) Nonuniformity of the light collection efficiency

(b) Position dependence of the measured energy deposition

Figure 2.12: An example of a) nonuniformity of the light collection efficiency depending on the incident position measured at HIMAC and b) the position dependence of the measured energy deposit for EM cascade showers simulated with 150 GeV electrons, where the results of (a) are included in the detector simulation. In both figures, the results of 5th layer of the Arm1 40 mm calorimeter are plotted and signals are normalized to the center values. Horizontal and vertical axes represent the x and y coordinates of the Arm1 40 mm calorimeter (40 mm × 40 mm). Since the direction of the read-out of the light is not perpendicular to the edge of the GSO scintillator, asymmetry can be seen in the Arm1 large tower.

nonuniformity of the scintillator is still observed in the map. The obtained response maps for each layer are used as $F_i(x, y)$ in Eq.2.3. All measured nonuniformity maps are shown in Fig. A.1 and A.2 in Appendix A.

2.6.2 Crosstalk on the GSO-bar hodoscope

GSO-bars have no cladding materials different from SciFi as described in Sec. 2.3.4, hence the GSO-bar hodoscope has non-negligible crosstalk between neighboring GSO-bars. Crosstalk also occurs at the MAPMT input surface by the leakage of light to neighboring pixels from the fiber end. Crosstalk effect in the GSO-bar bundle is not a problem for single shower case from the point view of position resolution, because the effect just makes lateral distribution smeared. On the other hand, when two (or more) particles enter the calorimeter, smeared lateral distributions make the identification of each shower difficult, especially when the energies of two particles is largely asymmetric. Thus we must understand the response of the GSO-bar hodoscope against the crosstalk effect to deal with such multi-hit events.

The channel in which beam passes is easily identified because the expected energy

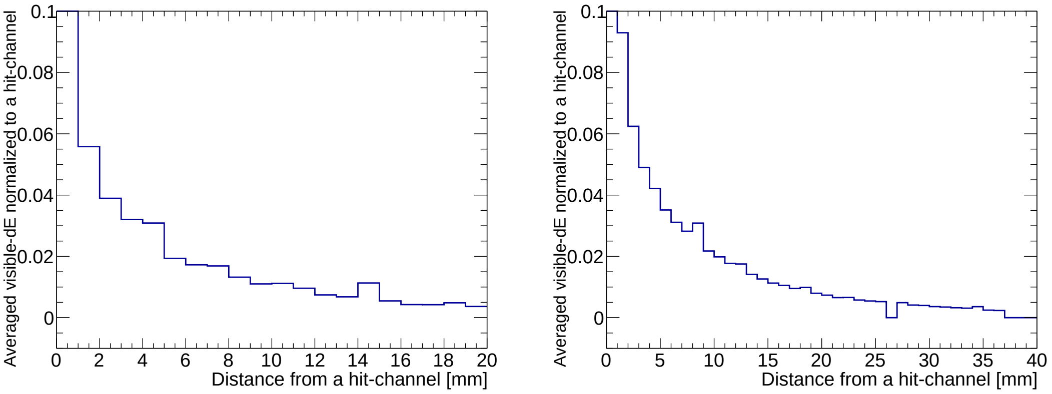

(a) Arm1 small tower

(b) Arm1 large tower

Figure 2.13: Averaged crosstalk response of the 20 and 40 mm tower measured at HIMAC with use of heavy ion beams. Vertical axis represents the energy deposition in each channel normalized to the beam-hit channel. Horizontal axis is the distance from the beam-hit channel.

deposition in each channel is enough high, approximately 44 MeV. The responses of the adjacent channels of the beam hit channels are then measured. Figure 2.13 shows the averaged crosstalk response for the GSO-bar hodoscope, where the amount of crosstalk is shown as a function of the distance from the beam-hit channel. Averaged crosstalk responses 9 % and 6 % adjacent to the beam-hit channel are observed in the GSO-bar hodoscope of the 20 mm and 40 mm calorimeters, respectively.

Crosstalk matrices for the correction of each lateral distribution, Γ in Eq.2.4, are determined by the averaged responses. Even though the crosstalk response is not uniform for each channel, the averaged crosstalk response is used in the following analysis. The previous works have confirmed that crosstalk correction with use of the averaged responses shows performance as good as those with channel-by-channel response matrices by comparing the lateral shower profile with these two crosstalk correction methods.

Chapter 3

Calibration and performance studies of the upgraded detectors

Dedicated beam tests have been performed at the CERN SPS for the calibration and performance studies of the upgraded detectors. All the calibration and performance studies are performed within the energy range which SPS can provide, while LHCf detectors are expected to measure the particles up to 6500 GeV at the maximum. Therefore, the agreement of the detector responses between the measured data and detector simulation is also examined carefully.

3.1 Experimental setup of the SPS H4 beam test

The beam test of the upgraded LHCf detectors was performed at the T2-H4 beam line in the SPS North area, CERN in 30th July to 11th August 2015. The Arm1 and Arm2 detectors are installed in aluminum boxes within which the temperature inside is controlled with a chiller. All operations are carried out under a temperature-stable condition of the detectors, i.e, variation is less than 0.1 °C per hour. To minimize materials in front of the detectors, a small window on the upstream panel of the aluminum box is made and it is covered with a thin paper. Figure 3.1 shows the setup of the beam line. The detectors and electronics are located on the movable stage which moves along the plane perpendicular to the beam axis in order to scan the entire calorimeter surface. On the stage, a micro-strip silicon tracker (ADAMO, [50]) is placed in front of the detectors in order to determine the position of incident particles. The performance of the ADAMO tracker has been studied experimentally and its position resolution is better than 30 μm.

Electron beams in the energy range from 100 GeV to 250 GeV are used for the test of the energy dependence of the gain calibration associated with C_i in Eq. 2.3 and linearity measurement of the calorimeters. 150 GeV electron beams are used for the scanning of the calorimeters. The all area of the calorimeters is exposed

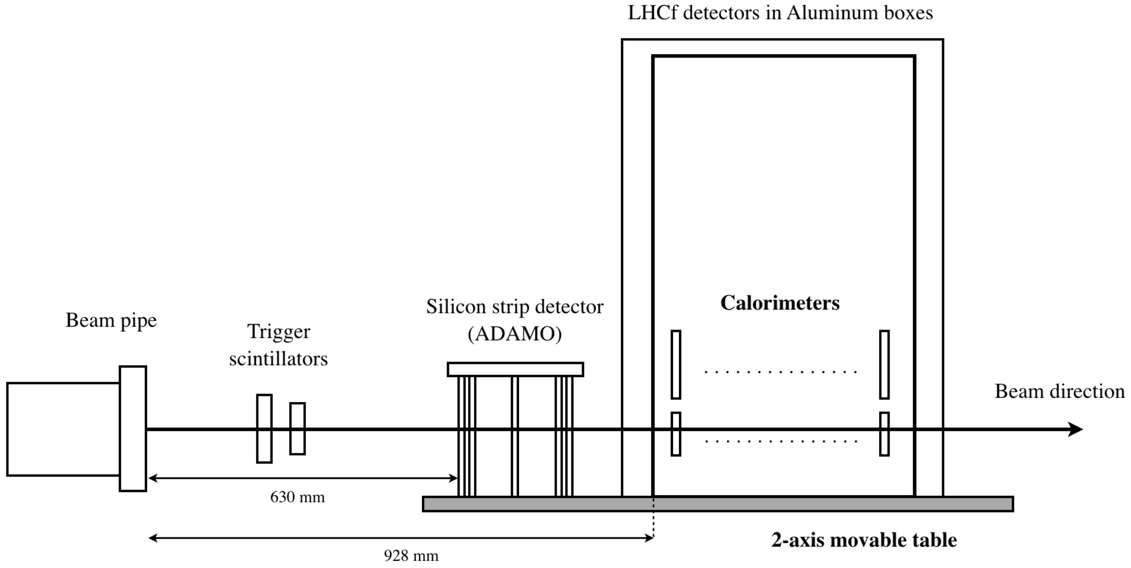

Figure 3.1: The detector setup at the beam line. Beams enter to the detector from the left side. The detectors are kept under stable thermal condition inside the aluminum boxes and the silicon strip particle tracker is located on the movable table to expose whole area of the calorimeters to beam.

to understand the position dependence of the response. Square trigger-scintillators of size 20 mm and 30 mm are installed between the table and the beam pipe. A coincidence of these scintillator signals is used to trigger the data acquisition. The typical spreads of the electron and muon beams are smaller than 20 mm. Tens of thousands of triggered events are collected for each energy and hundreds of thousands of triggered events are collected by the position scanning in order to cover all area of the calorimeter acceptances. Even though the purity of delivered electron beams are good, we eliminated the contamination, such as charged pions, by using the information of the longitudinal development of cascade showers in a calorimeter. We use the method for EM/hadron shower seperation as well as that for the LHC analysis, and the details are introduced in Chap. 4. The periods of the Arm2 and Arm1 data taking are separated in time in the first and second halves, respectively, during the two weeks of the beam time. Therefore, the level of the contamination in the beams are not always identical for both detectors.

3.2 Calibration of the upgraded detectors

3.2.1 Absolute gain calibration of the GSO-plate layers

In order to estimate the energy deposited in each layer from the measured charge by the ADC units, the charge distributions of each sampling GSO layer with mono-energetic electron and muon beams are compared with the prediction by MC simulations. Cosmos 7.633 [51] and EPICS 9.15 [52] packages are used for the MC simulations. The entire experimental setup including last 12 meters of the beam pipe is implemented in the MC geometry.

Electron data are used to determine the conversion factors between the ADC units and the real energy deposit (in GeV) in the 2nd-10th layers where EM showers are sufficiently developed. The energy deposits of MC events are scaled by a factor C_i and noise fluctuations are added to each channel according to the measured pedestal fluctuations during the test.

The scaled MC distributions (in ADC units) are then compared with the energy deposit distributions of the data using a minimum chi-square test. Events where the particle is injected near the edge of the calorimeters are rejected to reduce the effect of position-dependent light collection efficiency of the GSO scintillators and of lateral shower leakage. The events in a 4(8) mm × 4(8) mm square around the center of the 20(40) mm calorimeter of Arm1 are selected, and the events in a 5(10) mm × 5(10) mm square around the center of the 25(32) mm calorimeter of Arm2 are selected. In addition, only bins with content above 30 % of the maximum bin are used in the χ^2 test to avoid the tail components of the distribution. MC distributions are normalized to the area within those used in the χ^2 test. χ^2 is defined as

$$\chi^2_{C_i} = \sum \left(\frac{N_{data} - N_{C_i,MC}}{\sqrt{\sigma^2_{data} + \sigma^2_{MC}}} \right)^2 , \tag{3.1}$$

where N_{data} and $N_{C_i,MC}$ represent the number of content in each bin of the data and the scaled MC with C_i, respectively. σ_{data} and σ_{MC} are corresponding statistical errors. Degree of freedom distributed around 30 depending on the layers. Figure 3.2 and 3.3 show the data and MC histograms with the best-fit parameters set for Arm1 and Arm2, respectively, with electron beams of 200 GeV. The MC distributions of all layers reproduce well the data distributions. The results of the χ^2 test which returns the best in each layer are summarized in Tab.3.1.

The factors C_i, which give minimum χ^2 for each layer, are defined as conversion factors. The conversion factors are calculated with various electron beam energies from 100 to 250 GeV to estimate the systematic error associated with this method.

For deeper layers where the energy deposit of electron-induced showers is not sufficient, muon data are used to measure the conversion factors. Information from

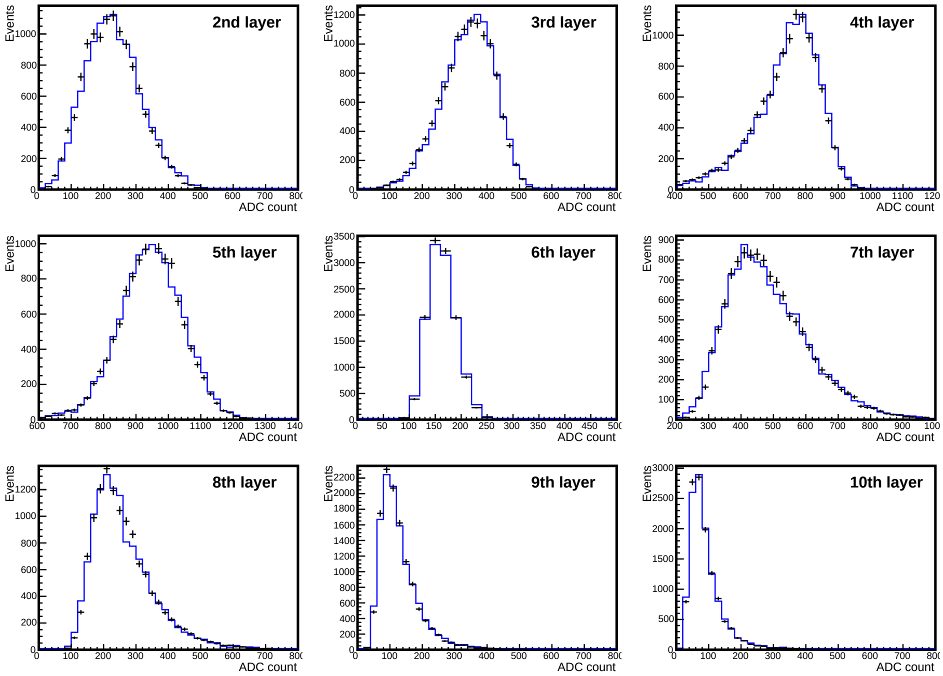

(a) Electron, Arm1 20 mm calorimeter

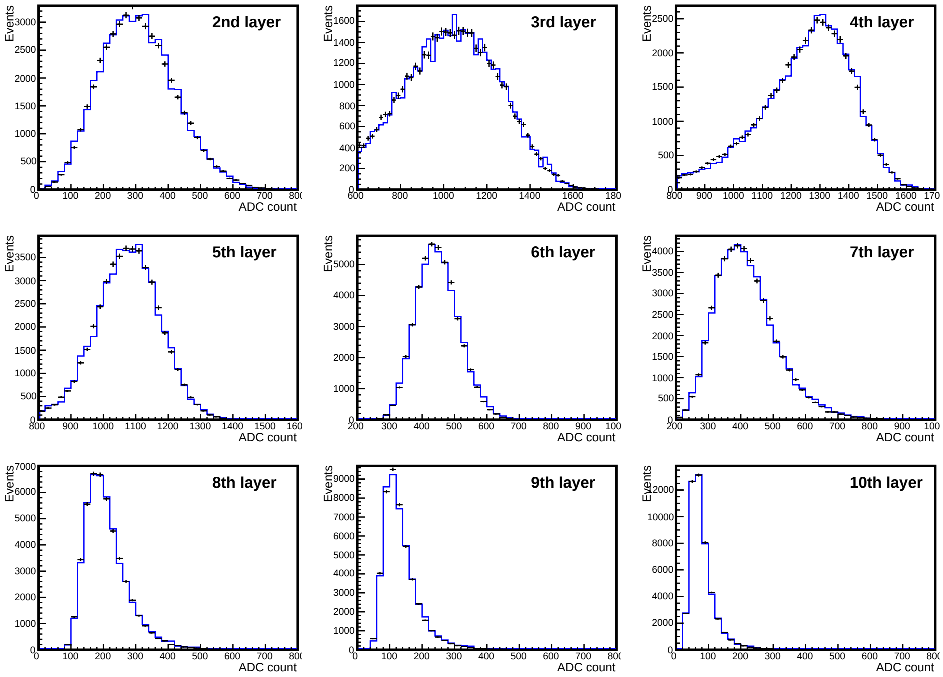

(b) Electron, Arm1 40 mm calorimeter

Figure 3.2: The energy deposit distributions of the experimental data (black points) and simulation (blue line) of the 2nd to the 10th layer of the Arm1 a) 20 mm and b) 40 mm calorimeters. The simulation distributions shown here are those having the minimum-chi-square parameters set. Injected particles are 200 GeV electrons. The horizontal axis represents the ADC counts. The area of each MC distribution is normalized to the area of the corresponding data distribution.

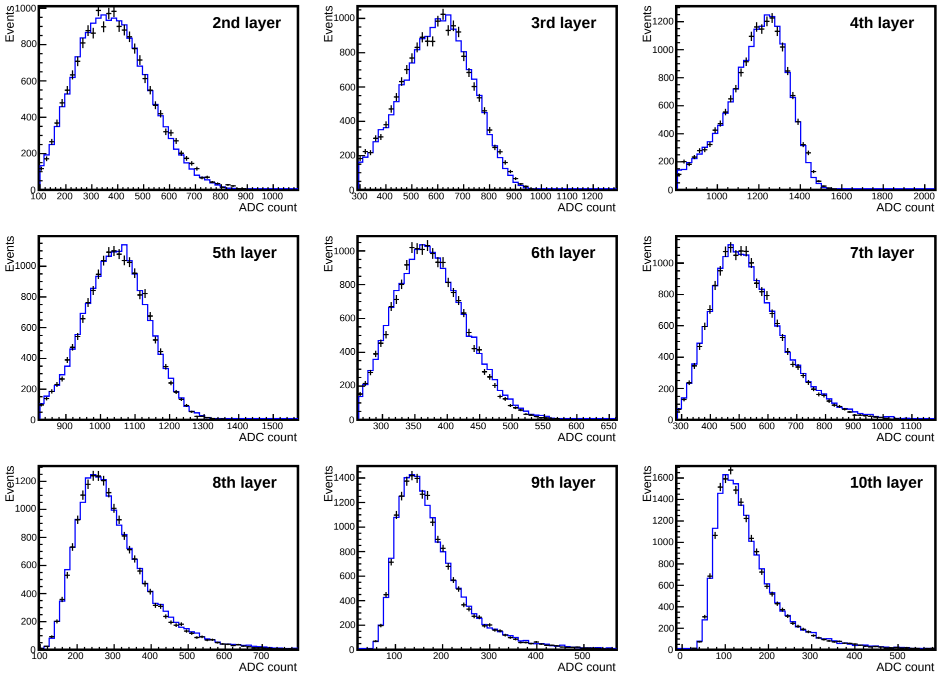

(a) Electron, Arm2 25 mm calorimeter

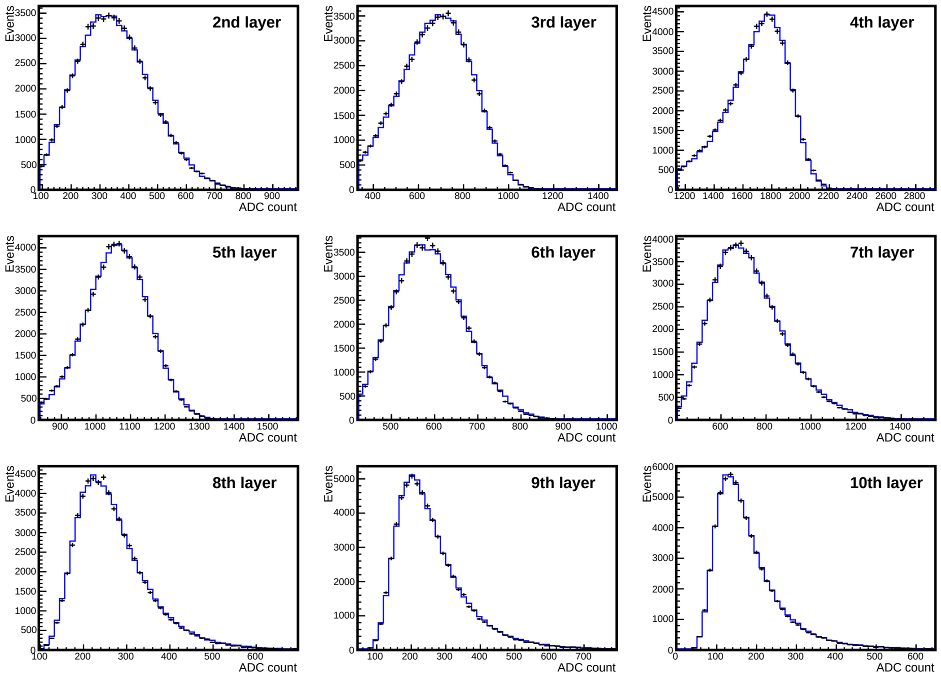

(b) Electron, Arm2 32 mm calorimeter

Figure 3.3: The energy deposit distributions of the experimental data (black points) and simulation (blue line) of the 2nd to the 10th layer of the Arm2 a) 25 mm and b) 32 mm calorimeters. The simulation distributions shown here are those having the minimum-chi-square parameters set. Injected particles are 200 GeV electrons. The horizontal axis represents the ADC counts. The area of each MC distribution is normalized to the area of the corresponding data distribution.

Table 3.1: Minimum χ^2 and DOF of the best fit parameter set for 200 GeV electrons

(a) Arm1 20 mm calorimeter

layer	χ^2	DOF	Prob.
2	54.708	32	0.007
3	21.478	30	0.872
4	51.859	31	0.011
5	32.275	34	0.552
6	37.320	39	0.547
7	32.124	42	0.865
8	31.163	26	0.222
9	27.336	30	0.606
10	51.606	45	0.231

(b) Arm1 40 mm calorimeter

layer	χ^2	DOF	Prob.
2	47.992	45	0.352
3	41.596	46	0.657
4	9.3058	26	0.999
5	48.942	37	0.091
6	43.025	48	0.676
7	24.644	32	0.820
8	30.919	39	0.819
9	25.037	29	0.676
10	40.319	36	0.285

position-sensitive layers is used to extract penetrating events and reject pion contamination. The average number of photoelectrons generated by muons is also set as a free parameter to correctly reproduce the width of the data distribution. The smearing of the distributions follows the Poisson distribution taking the number of photoelectron as the mean value. The resolution of the charge distribution generated from a photoelectron in the PMT is considered by applying a Gaussian smearing. The resolution is fixed at 30 % in this analysis. Best-fit parameters are determined using a χ^2 test also for the muon case. Figures 3.4 and 3.5 show the data and MC histograms with the best-fit parameters set of Arm1 and Arm2, respectively. Since the muon measurements of Arm1 and Arm2 are performed under the different beam condition, pion contamination which passed the event selection makes the tail component in the data distributions only for Arm2 as seen in Fig. 3.5. In order to avoid the influence of the tails in the chi-square test, only bins with content above 30 % of the maximum bin are compared as well as the electron case. Eventually the MC distributions of all layers show good agreement with the data distributions around the peaks. In this beam test, we are not able to aquire the data of the first layer of the Arm1 20 mm calorimeter, thus the conversion factor for this layer is calculated by the data taken in 2014 under the condition essentially same as this test.

Although we can determine the factors for all layers using muon data, the precision of the calibration by electron data is better than that by the muon data, owing to the higher energy deposit. The conversion factor error ΔC_i is defined as the range satisfying $\Delta\chi^2 = |\chi^2 - \chi^2_{min}| < 1$ for electron beam (one free parameter in the fit) and $\Delta\chi^2 = |\chi^2 - \chi^2_{min}| < 2.3$ for muon beam (two free parameters). The minimum χ^2 and associated degree of freedom (DOF) of the Arm1 20 mm and 40 mm calorimeters, for instance, are summarized in Tab. 3.2.

The calibration factors determined with different electron beam energies and with muon beam are compared. Since the applied high voltages for the PMTs are 600 V and

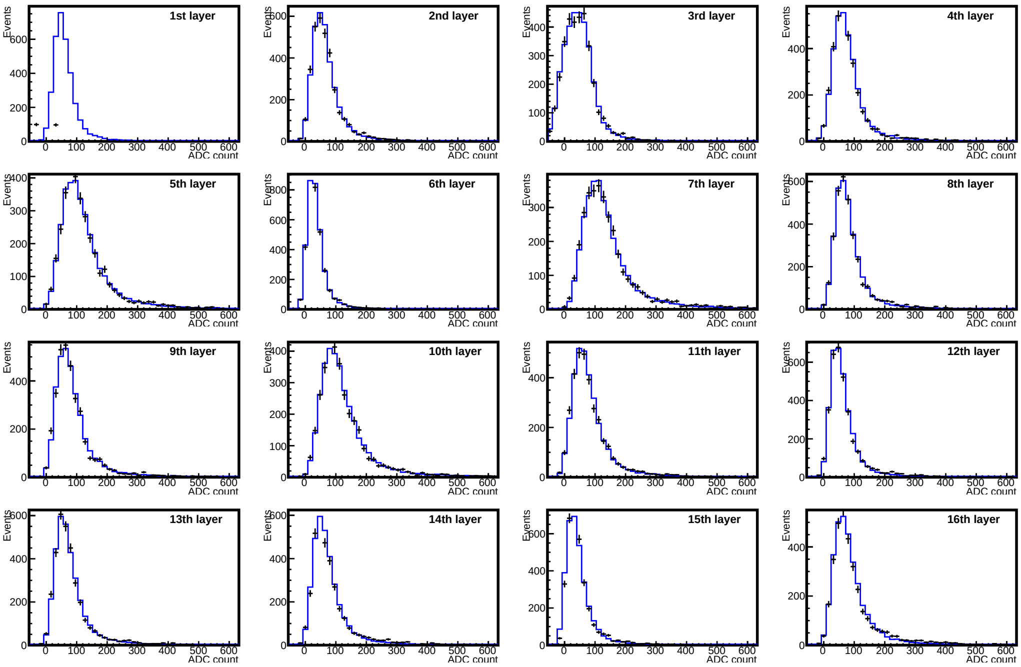

(a) Muon, Arm1 20 mm calorimeter

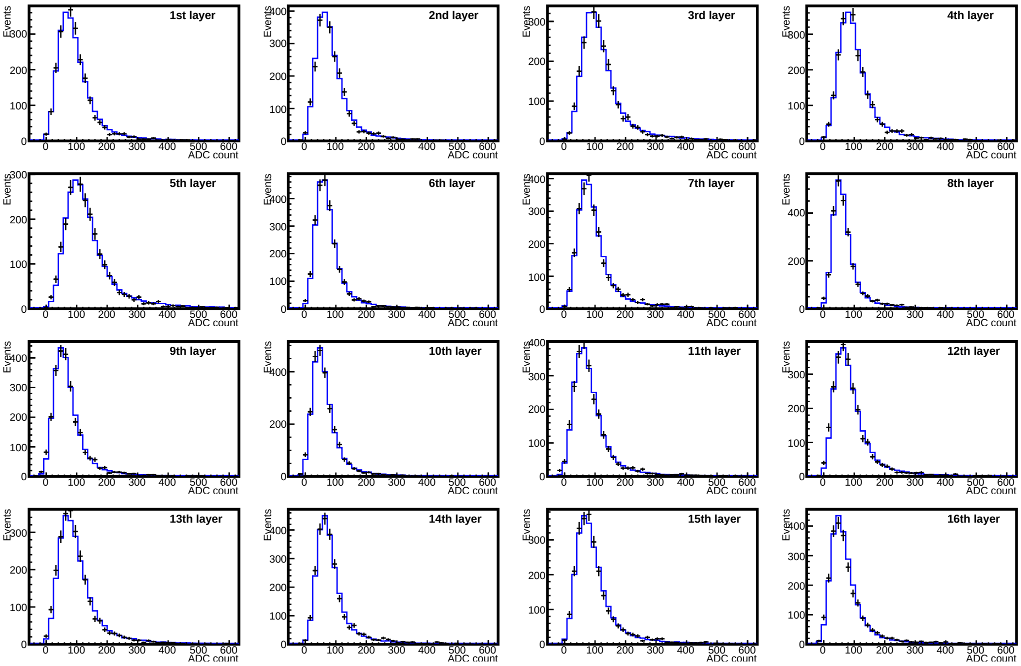

(b) Muon, Arm1 40 mm calorimeter

Figure 3.4: The energy deposit distributions of data (black points) and simulation (blue line) of the Arm1 a) 20 mm and b) 40 mm calorimeters which have minimum-chi-square parameters set for all layers. Injected particles are 250 GeV muons. The horizontal axis represents the ADC counts. The area of each MC distribution was normalized to the area of the corresponding data distribution.

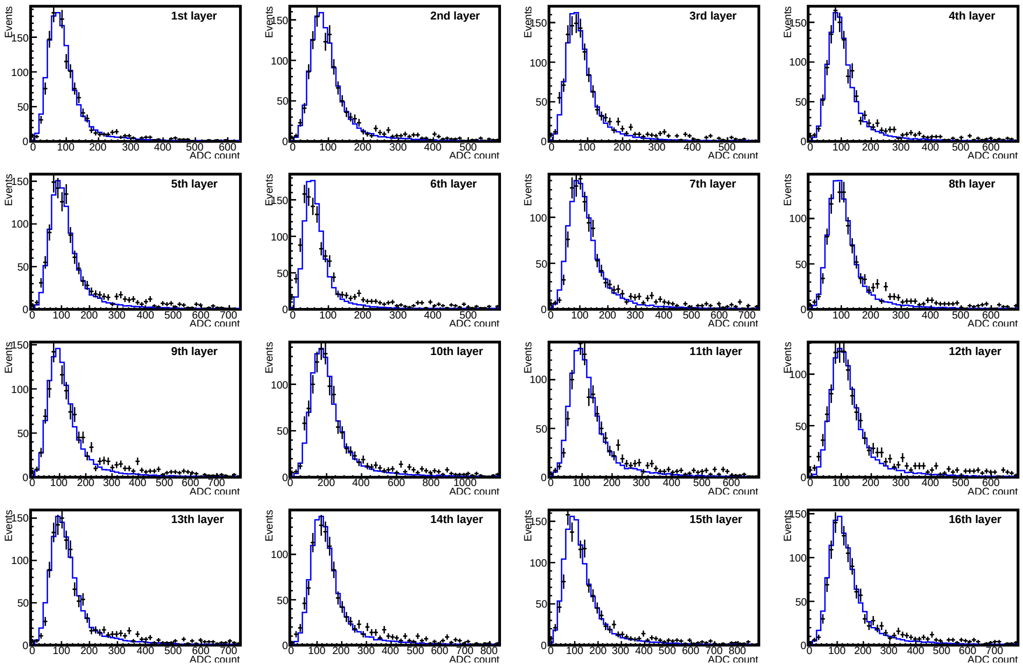

(a) Muon, Arm2 25mm calorimeter

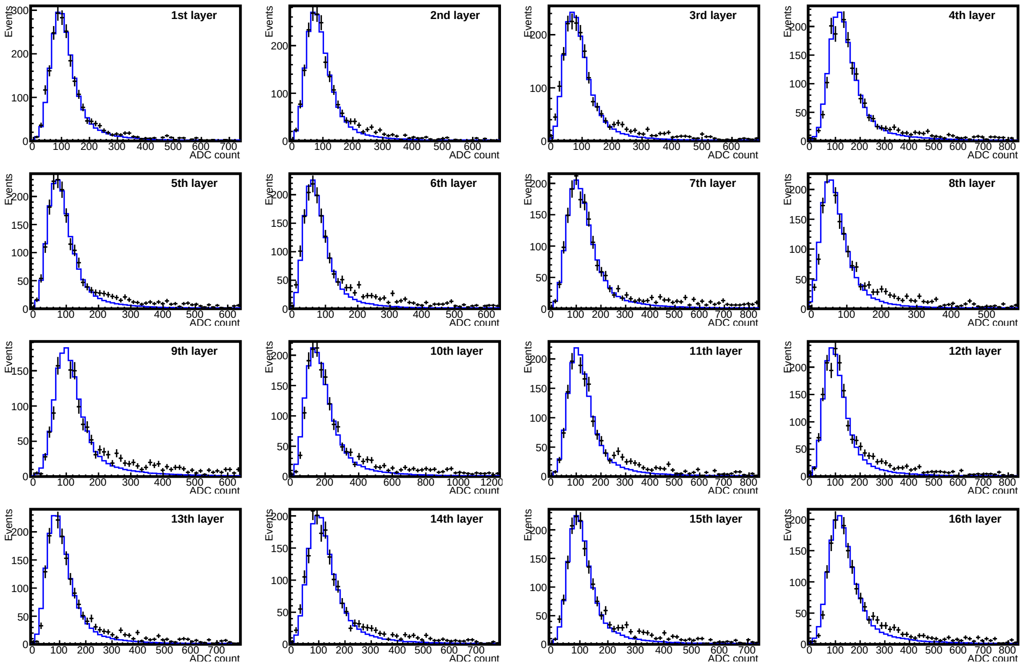

(b) Muon, Arm2 32mm calorimeter

Figure 3.5: The energy deposit distributions of data (black points) and simulation (blue line) of the Arm2 a) 25 mm and b) 32 mm calorimeters which have minimum-chi-square parameters set for all layers. Injected particles are 250 GeV muons. The horizontal axis represents the ADC counts. The area of each MC distribution was normalized to the area of the corresponding data distribution.

Table 3.2: Minimum χ^2 and DOF of the best fit parameter set for 150 GeV muons.

(a) Arm1 20 mm calorimeter

layer	χ^2	DOF	Prob.
1	-	-	-
2	34.971	23	0.052
3	40.290	29	0.079
4	29.190	24	0.213
5	36.717	34	0.344
6	12.794	14	0.543
7	22.931	37	0.966
8	18.079	23	0.753
9	23.583	23	0.427
10	39.096	32	0.181
11	43.939	26	0.015
12	12.164	18	0.839
13	18.579	23	0.725
14	38.490	19	0.005
15	20.436	16	0.201
16	28.269	24	0.249

(b) Arm1 40 mm calorimeter

layer	χ^2	DOF	Prob.
1	29.427	26	0.292
2	26.673	23	0.270
3	35.322	30	0.231
4	33.294	27	0.188
5	31.586	31	0.437
6	18.665	21	0.607
7	21.523	24	0.608
8	20.909	19	0.342
9	28.582	22	0.157
10	17.586	19	0.550
11	34.341	27	0.156
12	30.578	27	0.289
13	46.078	28	0.017
14	22.326	20	0.323
15	18.593	25	0.816
16	34.706	22	0.042

1000 V for the electron and muon operations, respectively, the muon-based conversion factors are re-scaled by the ratio of the PMT gain between the two configurations (ranging between 14 and 21). The temperature dependence of the PMT gain is corrected for the muon-based factors so as to adjust to the situation of the electron runs. The level of the correction is less than 10 %. Figure 3.6 shows the conversion factors of each layer of the Arm1 20 mm and 40 mm calorimeters. All points are normalized to the factors measured with the 200 GeV electron beam.

The data comparisons are used to estimate the systematic uncertainty of the calibration factors. The systematic errors associated with the conversion factors are estimated from the deviations of the electron factors obtained by various energies of electrons. The systematic error of the electron-based gain calibration is estimated as 2.2 % and 0.8 % for Arm1 and Arm2, respectively. The systematic error associated with muon-based gain calibration, which is estimated by calculating the ratios of the muon-based factor to electron-based factor for each layer, is considerably larger than that of the electrons: 7 % and 5–10 % for Arm1 and Arm2, respectively. The effect of uncertainty in muon-based factors is small for the photon energy reconstruction because they are used in the deeper layers (11th-13th), where the contribution to the total energy deposit S is 1.4(6) % in average for 200 GeV(6 TeV) incident photons.

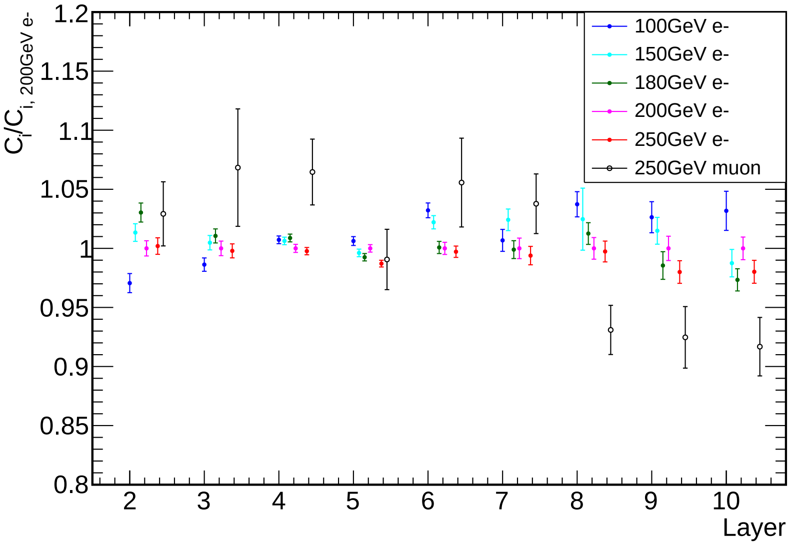

(a) Arm1 20 mm calorimeter

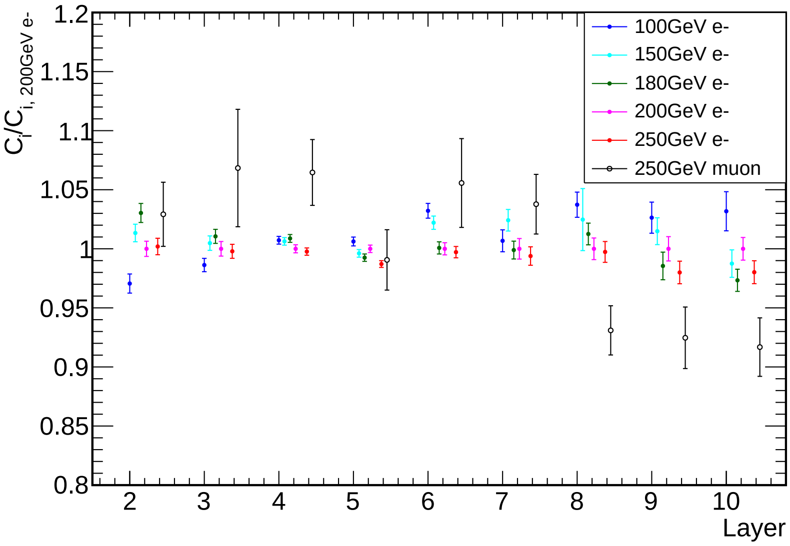

(b) Arm1 40 mm calorimeter

Figure 3.6: The dependence of the conversion factors derived from different energies and particles. Results of the Arm1 a) 20 mm and b) 40 mm calorimeters from the 2nd to the 10th layer are presented. The black points correspond to the muon-based factors while colored points represent the factors at various energies of the electron beam. All points are normalized to the factors obtained with the 200 GeV electron beam.

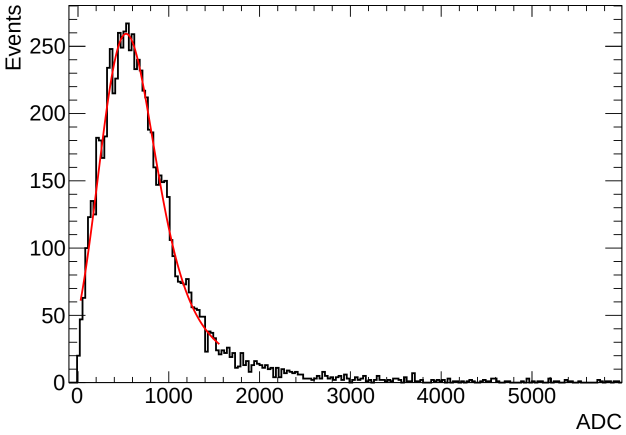

Figure 3.7: An example of the charge distribution of muon events. The distribution of the Arm1 20 mm calorimeter 1st layer X ch20 is shown here.

3.2.2 Gain calibration of GSO-bars of the Arm1 calorimeter

The gain calibration of all 480 channels of the GSO-bar hodoscope, $C_j^{\text{GSO-bar}}$ in Eq.2.4, is performed by using 250 GeV muon beams. Approximately 0.76 MeV of the deposited energy is expected when an MIP particle passes through 1 mm of a GSO-bar [46]. Because of such small energy deposit expected in muon evevnts, 950 V as the high voltage of MAPMT is applied to each channel of the GSO-bar hodoscope. A reference particle tracker, ADAMO, is located in front of the detector to locate a beam incident position at each GSO-bar layer. To extract deep penetrating events where uniform deposited energies are expected, the total energy deposited in the calorimeter is used to exclude backgrounds events such as pion contamination or muons that stop at the middle of the calorimeter.

A function convoluting Landau and Gaussian distributions is used to fit the energy deposition distributions. A most-probable value is defined according to a fit as a muon peak of a GSO-bar channel, of which ADC value is converted to 0.76 MeV. Figure 3.7 shows an example of a distribution of muon events observed by the GSO-bar hodoscope and the fitting result. Owing to the low photoelectron yields of the muon signal, the muon peaks are not able to be determined accurately, especially for relatively low-gain channels unlike the channel seen in Fig. 3.7. An alternative approach for the gain calibration is used for such channels. Using 150 GeV electrons, the average deposited energy on a GSO-bar is estimated from an expected lateral distribution of shower, when that channel is regarded as a shower peak. Eventually, dispersion of $C_j^{\text{GSO-bar}}$, which are translated to conversion factors, is 34 % as shown in Fig. 3.8.

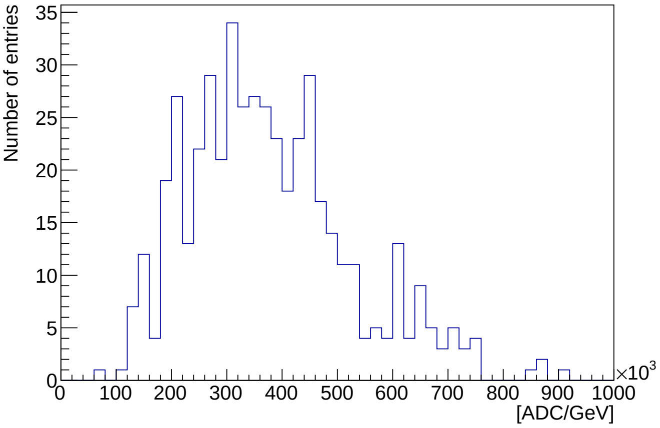

Figure 3.8: Distribution of the conversion factor [ADC/GeV] of all GSO-bar hodoscope channels.

3.2.3 Attenuation factor of the 200 m signal cables

In the LHC configuration, the PMT signals are sent from the detector to the electronics through 200 m long cables, thus the signal must be corrected to compensate losses along the cable. The signals of all channels experienced 300 ns of delyay in the SPS configuration. Since the waveform of a GSO scintillator signal is different from that of a plastic scintillator, the attenuation correction factor for each channel, λ in Eq.2.2, of the new detectors have to be measured again. The attenuation factor is measured by comparing the energy depositions for 150 GeV electron beam with different analog cable length: a) a replica of the 200 m long cable in the LHC between the detector and the electronics or b) with 300 ns cables as the nominal configuration in the beam test. Cable attenuation factors are estimated as 0.902 ± 0.005 for all the layers of Arm1, while in Arm2 they are 0.887 ± 0.005 for the 16th layer of the 25 mm calorimeter, 0.908 ± 0.005 for layers 2–10 of the 32 mm calorimeter, and 0.902 ±0.005 for the other layers after scaling for the different length of the cables, ranging 180–194 m owing to the experimental constraint, used at LHC.

3.3 Performance for EM shower measurements

Performance of the photon measurement can be evaluted with that of electron because their interaction in a calorimeter and cascade shower derived from them are essentially same. Thus, in the following sections, the performance of the photon measurement of the LHCf detectors using the electron data is examined. The energy and position resolutions, the position dependence of the energy and position reconstructions and the linearity of the detector responses are tested with various energies of electron beams.

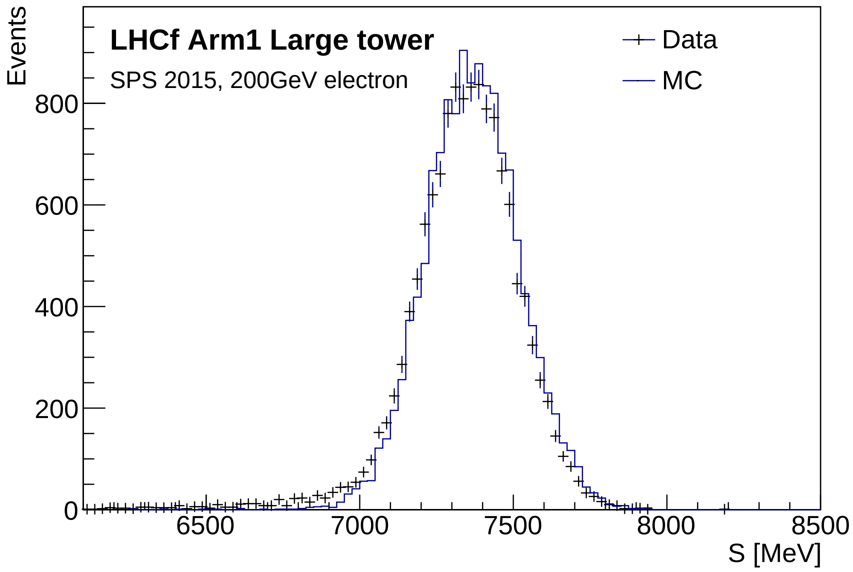

Figure 3.9: The distribution of the total energy deposit of the data (black points) compared with the simulation (blue line) of the Arm1 40 mm calorimeter. Electron beam with the momentum of 200 GeV is used here. Gaussian fit returns the mean and the standard deviation of 7.35 GeV and 0.16 GeV, respectively.

3.3.1 Energy resolution of the calorimeters

The energy resolution of the calorimeters are evaluated with the S distributions measured at each mono-energy beam. The events in a 4(8) mm × 4(8) mm square around the center of the 20(40) mm calorimeter of Arm1 are selected and the events in a 5(10) mm × 5(10) mm square around the center of the 25(32) mm calorimeter of Arm2 are selected. Figure 3.9 shows an example of the S distribution observed in the Arm1 40 mm calorimeter. For a primary electron energy of 200 GeV, an average sampled energy of 7.35 GeV is measured with a standard deviation of 0.16 GeV. The MC distribution reproduces the data distributions well.

The energy resolution is defined as 1-σ of the Gaussian fitting to the S distribution. The energy dependence of the energy resolution, compared with the MC prediction, is shown in Fig. 3.10 and 3.11 for Arm1 and Arm2, respectively. The results are fit by a function quadratically adding the stochastic and the constant terms

$$\frac{a}{\sqrt{E}} \oplus b, \tag{3.2}$$

where E denotes the energy in the unit of GeV. The obtained results are $a = 28.55 \pm 0.59$ %, $b = 0.74 \pm 0.12$ % and $a = 29.22 \pm 0.18$ %, $b = 1.10 \pm 0.03$ % for the Arm1 20 mm and 40 mm calorimeters, respectively, while $a = 22.10 \pm 0.33$ %, $b = 0.96 \pm 0.04$ % and $a = 23.72 \pm 0.16$ %, $b = 0.83 \pm 0.02$ % for the Arm2 25 mm and 32 mm calorimeters,

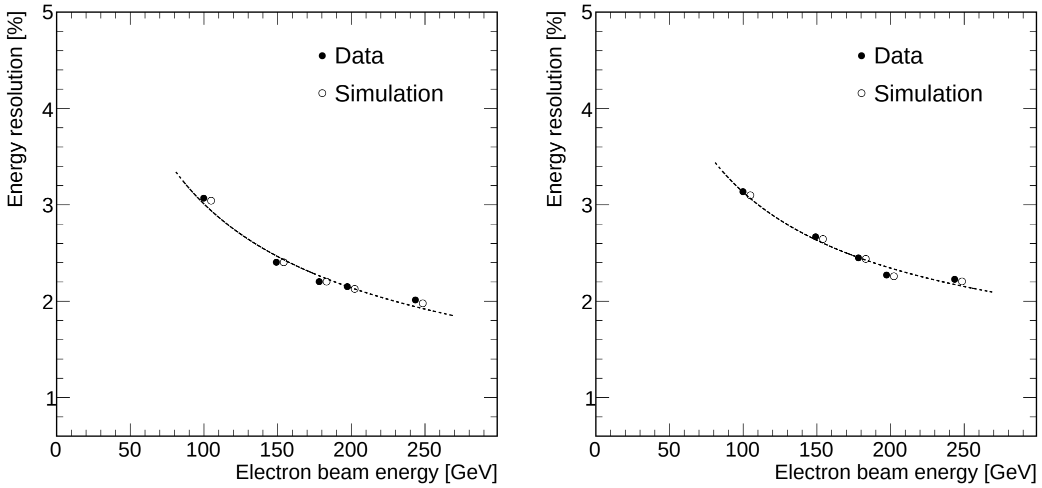

(a) Arm1 20 mm calorimeter

(b) Arm1 40 mm calorimeter

Figure 3.10: Energy dependence of the energy resolution of the Arm1 a) 20 mm and b) 40 mm calorimeters for the data (filled circles) and the MC (open circles, shifted horizontally by 5 GeV). The events in a 4(8) mm × 4(8) mm square around the center of the 20(40) mm calorimeter are selected.

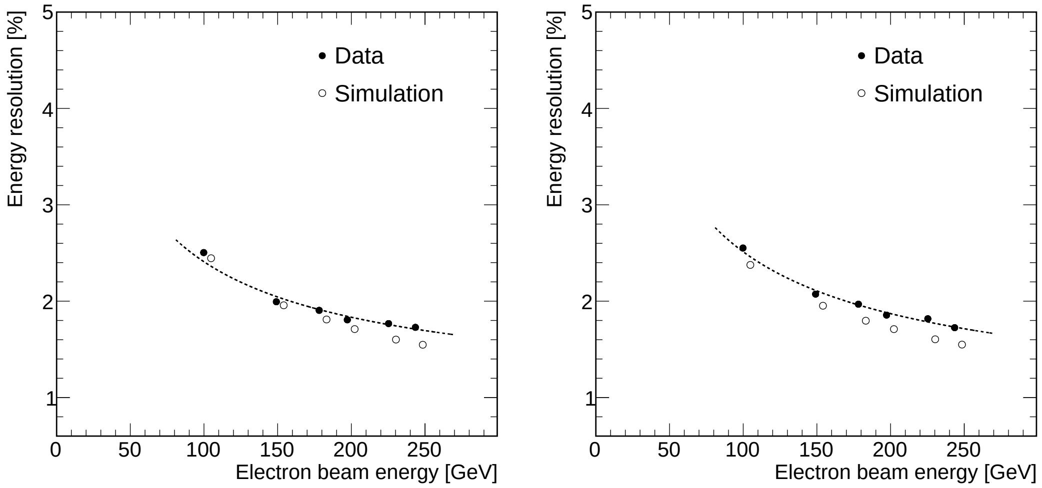

(a) Arm2 25 mm calorimeter

(b) Arm2 32 mm calorimeter

Figure 3.11: Energy dependence of the energy resolution of the Arm2 a) 25 mm and b) 32 mm calorimeters for the data (filled circles) and the MC (open circles, shifted horizontally by 5 GeV). The events in a 5(10) mm × 5(10) mm square around the center of the 25(32) mm calorimeter are selected.

respectively.

Although the energy resolutions are evaluated with use of the center region, the scan with 150 GeV electron beams is to test the resolutions of all the calorimeter surfaces. Figure 3.12 shows the position dependence of the energy resolution of the Arm1 calorimeters. Energy resolutions are evaluated every 1 mm and 2 mm steps for the 20 mm and 40 mm calorimeters, respectively, except for the 2 mm edge region of each calorimeter. The results are shown in Fig. 3.12(a) and 3.12(c). Distribution of S at three different points along the diagonal direction as indicated by small squares are shown in Fig. 3.12(b) and 3.12(d). Figures 3.12(a) and 3.12(c) indicate that the energy resolution becomes worse as it goes to the edge of the calorimeter. The incident position of the particles here are reconstructed by using the information of the position sensitive layer in the detector. For instance, in Fig. 3.12(c), the energy resolution is better than 3 % at the very center of the Arm1 40 mm calorimeter, while it is nearly level of 5 % at the edge of the calorimeter. 4–5 % of energy resolution at 150 GeV EM shower is not the matter as it still meets the requirement for the photon analysis in the p–p 13 TeV collisions. However, we have to carefully understand the systematic shift of the peak of S, especially those seen in the 40 mm calorimeter as shown in Fig. 3.12(d). Such systematic shift of the peaks, namely the position dependence of the energy reconstruction, is discussed in Sec. 3.3.2.

3.3.2 Position dependence of energy reconstruction

As mentioned in Chap. 2, the position dependence of light collection efficiency in GSO scintillators and shower leakage could cause the position dependence of the energy reconstruction. Nonuniformity of light collection and shower leakage effects are simultaneously corrected using a two-dimensional correction map, $F(x, y)$ of each layer as discussed in Eq. 2.3 and Fig. 2.12(b). These position dependent effects are known to be energy independent within our requirement.

The correction is tested by checking the position dependence of the S for each calorimeter. Data with 150 GeV and 200 GeV electron beams are used for this study of Arm1 and Arm2, respectively. The uniformity of the calorimeter response before and after the correction is demonstrated in Fig. 3.13. The distribution of averaged S in each position of the Arm1 40 mm calorimeter is shown in Fig. 3.14. In Arm1, the deviations of the S distributions relative to the value in the center of the calorimeter are 1.0(0.9) % for the 20(40) mm calorimeters, while in Arm2 they are 1.1(1.0) % for the 25(32) mm calorimeters. Therefore, the systematic uncertainty associated to the position dependence of the energy determination is estimated to be about 1 % for both Arm1 and Arm2. Particles incident within 2 mm from the edge of the calorimeters are not considered in the analysis, because the gradient of the position dependence of the energy deposition is too large and it cannot be properly corrected with this method. The same cut is applied to the LHC analysis.

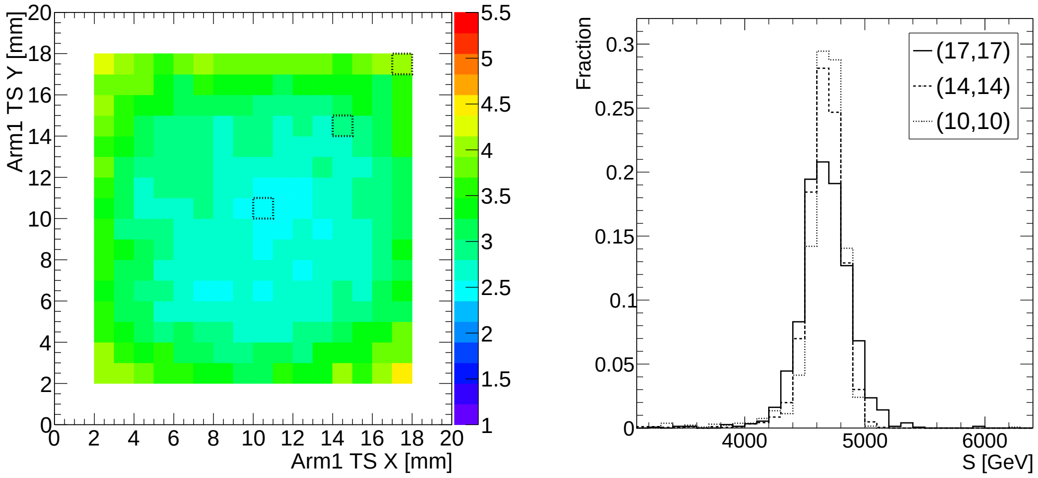

(a) Energy resolutions of 20 mm calorimeter (b) Sample S distributions

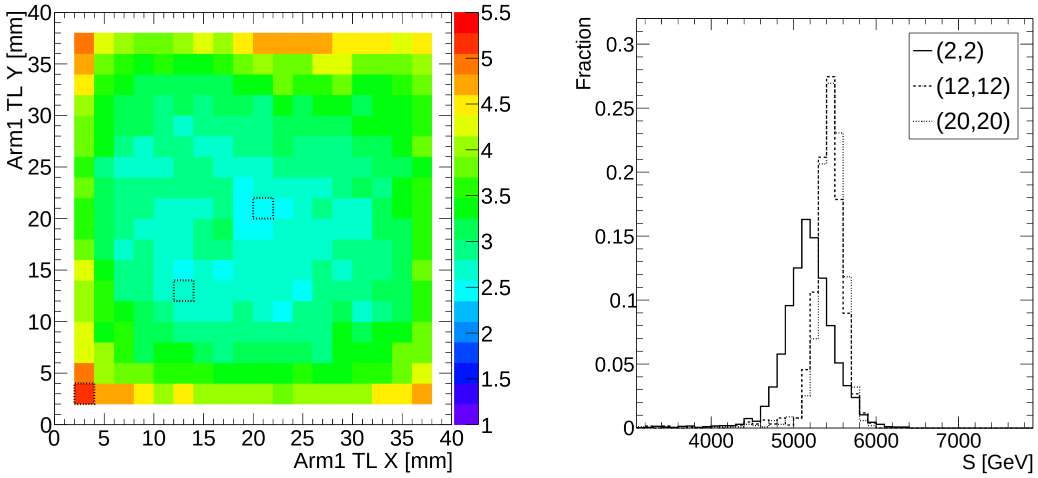

(c) Energy resolutions of 40 mm calorimeter (d) Sample S distributions

Figure 3.12: Energy resolution [%] of the Arm1 a) 20 mm and c) 40 mm calorimeters for 150 GeV electron as a function of the incident position. Samples of the S distributions at several positions indicated by squares for the Arm1 b) 20 mm and d) 40 mm calorimeters.

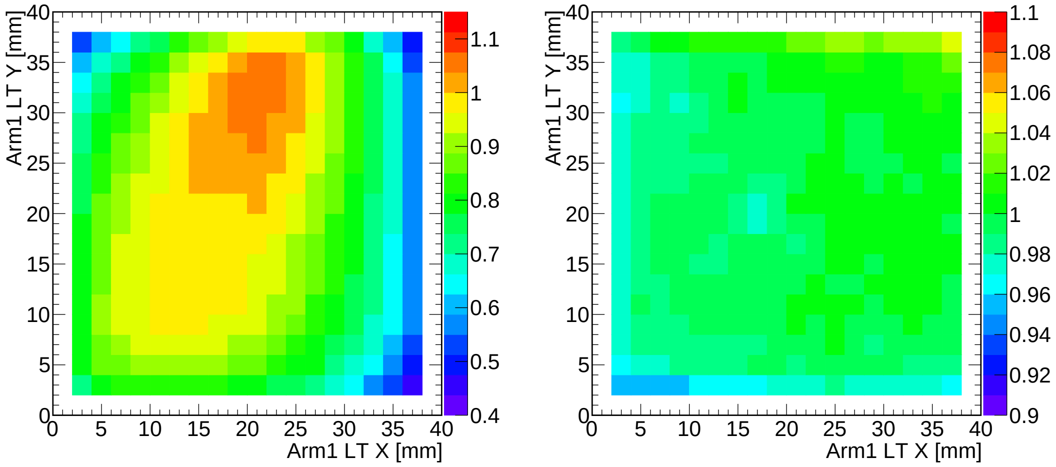

(a) Arm1 40 mm, before the correction (b) Arm1 40 mm, after the correction

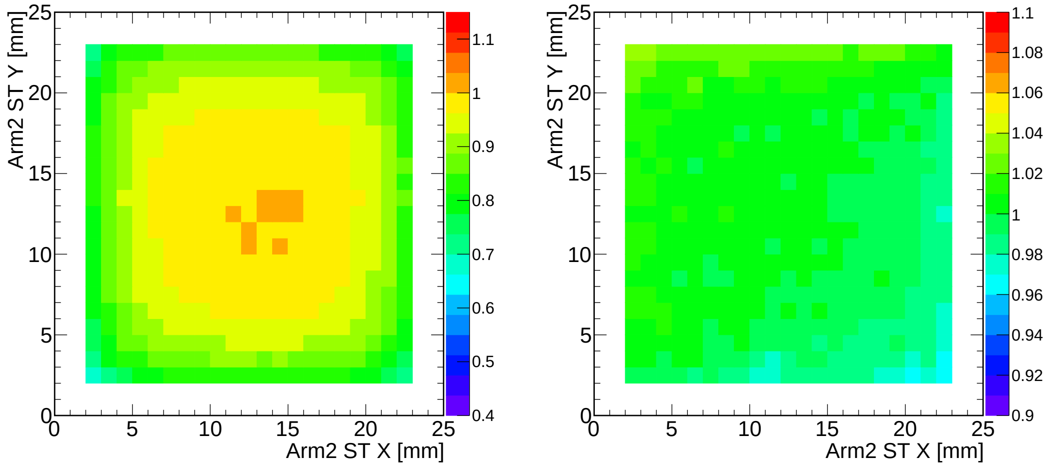

(c) Arm2 25 mm, before the correction (d) Arm2 25 mm, after the correction

Figure 3.13: The position dependence of S. X and Y represent the transverse coordinates of the Arm1 40 mm calorimeter a) before and b) after the correction, and the Arm2 25 mm calorimeter c) before and d) after the correction. The region within 2 mm from the edge of the calorimeters was not considered in the analysis.

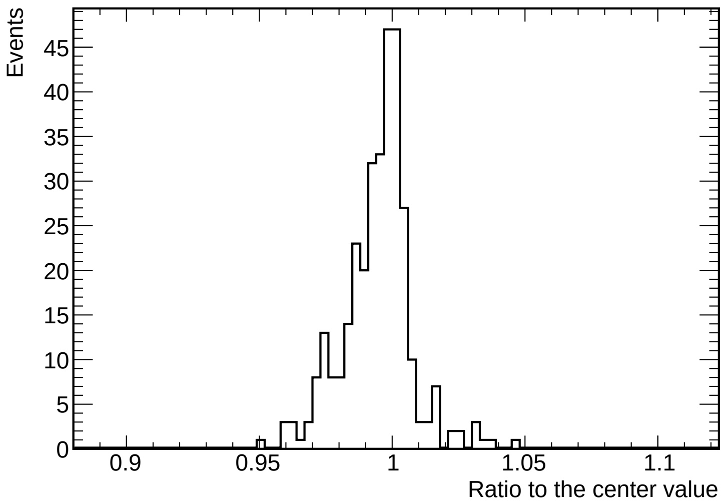

Figure 3.14: The one dimensional ratio distribution of Fig. 3.13(b).

3.3.3 Position resolution of the shower imaging layers

Particles entering the detector develop the cascade showers in the calorimeters. GSO-bar hodoscope layers measure the lateral distribution of the cascade showers at each depth. The lateral distributions in the orthogonal directions, X and Y, in each layer are then used to determine the hit position of the incident particles. In each event, measured charge information of the GSO-bar hodoscope are converted to the energy deposition as discussed in Sec. 2.5. Figure. 3.15 shows a lateral distribution measured in the second X layer of the GSO-bar hodoscope for the 250 GeV electron beam. The event shown in Fig. 3.15 demonstrates that the measured lateral shower distribution before the crosstalk corretion is smeared compared to that of after the correction. The profile of the lateral distribution, such as the width, after the correction is compatible with what is expected from the detector simulation without the crosstalk effect.

After the shower event selection, lateral shower distributions measured by each layer of the GSO-bar hodoscope are fit with the empirical function based on [55],

$$f = A\left[r\frac{\frac{1}{2}\sigma_a}{\{(x-x_0)^2+\sigma_a\}^{\frac{3}{2}}} + (1-r)\frac{\frac{1}{2}\sigma_b}{\{(x-x_0)^2+\sigma_b\}^{\frac{3}{2}}}\right], \tag{3.3}$$

where x_0 is the shower peak position, r is the fraction of the peak height of the fisrt to the second term, $\sigma_{a(b)}$ determine the width of the distribution, and A is normalization factor. The alignment of each GSO-bar position is measured with use of the muon beams not to develop the cascade showers. The obtained positions of GSO-bars are compatible and reasonable considering the holder of the GSO-bar bundles as the mechanical limits, which are $20.1^{+0.1}_{-0.0}$ mm and $40.35^{+0.1}_{-0.0}$ mm for the 20 mm and

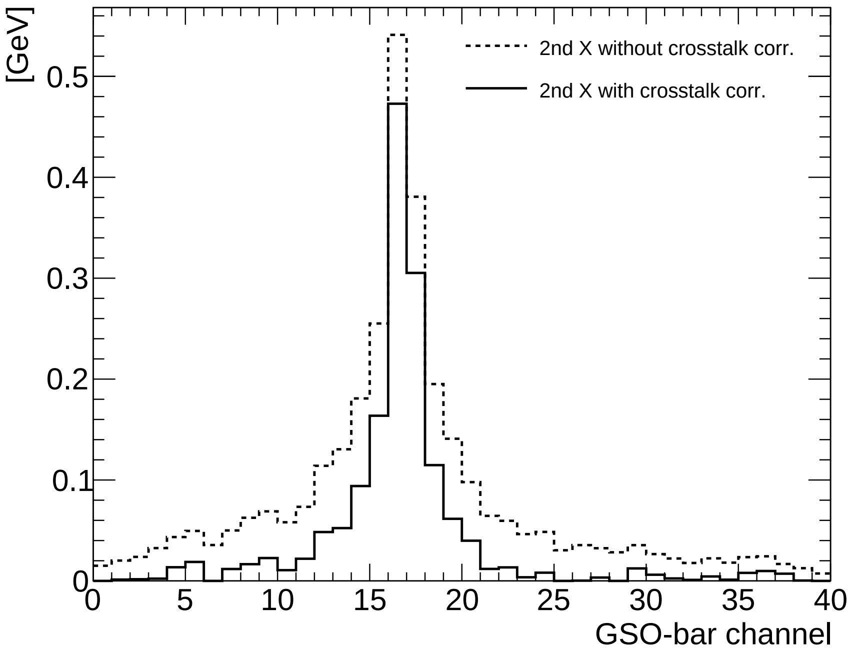

Figure 3.15: An example of the measured lateral shower distribution in the second X layer of the GSO-bar hodoscope. Electron beam with the momentum of 250 GeV is injected to the detector. Solid and dotted lines are the laterals before and after the crosstalk correction, respectively.

40 mm calorimeters, respectively. Each position of the GSO-bar determined by the alignment test is included in the analysis. The position resolution of the GSO-bar hodoscope is evaluated by comparing with the calculated incident positions with use of the ADAMO tracker. The calibration and performance of the ADAMO tracker is carefully studied. The ADAMO tracker is guaranteed to be used as the reference of the position, such as the position resolution of 30 μm.

Then residual between the reconstructed positions of the GSO-bar hodoscope and the ADAMO tracker is calculated in each event. Figures 3.16 and 3.17 are the residual distributions of the first and the second layers of the 20 mm and the 40 mm calorimeters, respectively. In Fig. 3.16 and 3.17, the distributions are calculated with the events hitting within 4 mm from the center of the calorimeters. Standard deviations of the residual distributions are defined as a position resolution in each beam energy, thus 100 μm for 20 mm 1st X for instance.

Figure 3.18 represents the position resolution of the first and the second layers of the GSO-bar hodoscope as a function of the electron beam energy. Corresponding the MC simulation results are compared with the observed results. The position resolution of the ADAMO tracker 30 μm is quadratically added to the calculated resolutions for the simulation data. Above the electron energy of 200 GeV, which is supposed to be the threshold for LHC 13 TeV collision data, we confirm better position resolution 130 μm than the previous LHCf Arm1 detector, while it was 170 μm using SciFi [35]. The improvement of the position resolution seems owing to the use of the holder structure of the GSO-bar hodoscope. SciFi used in the previous detector do not have any supporting structures such as holders, but each scintillating fibers are glued with each other [35]. Note that the obtained position resolution is slightly worse than that intrinsic resolution expected from detector MC simulation, however, these accuracy are precise enough for position reconstruction. The cause of the discrepancy would be related to the accuracies of the corrections for crosstalk between the GSO-bars and of the GSO-bar alignment.

Up to this point, the GSO-bar hodoscope has the position resolution, at the center of the calorimeters, which meets the requirement of the LHCf experiment. Position dependence of the position reconstruction is the another issue to be understood correctly. All the calorimeter surface is scanned with the 150 GeV electron beams in the test.

Residual distributions at three different positions are shown in Fig. 3.19. The peak position and width of the residual distributions are similar among the three positions on the first X layer of the 20 mm calorimeter, whereas a clear position dependence of the position reconstruction is observed in the first X layer of the 40 mm calorimeter. The residual distribution broadens as the incident position get closer to the edge of the calorimeter and its peak shifts by approximately +200 μm at 2 mm$< x <$3 mm, thus it indicates the reconstructed positions by the GSO-bar hodoscope are biased to the center of the calorimeter.

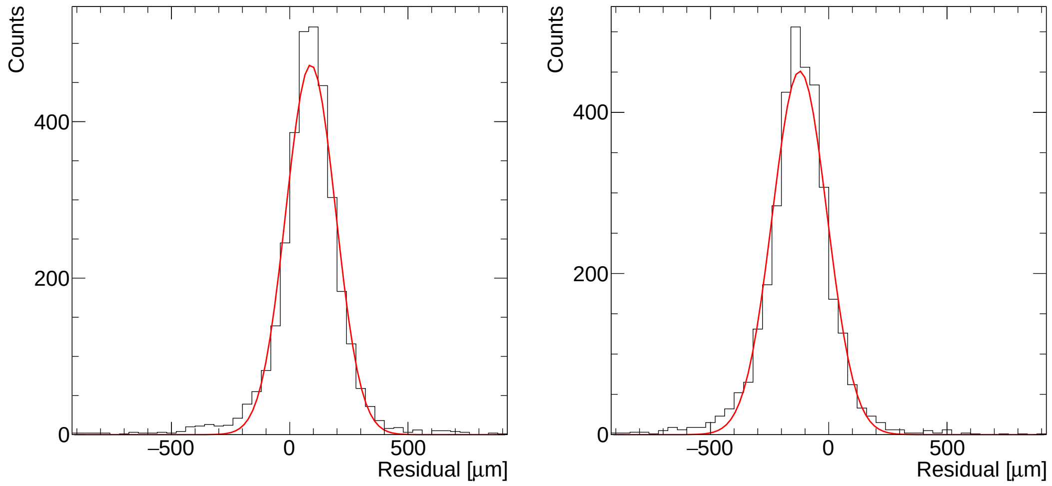

(a) 20 mm 1st layer X (b) 20 mm 1st layer Y

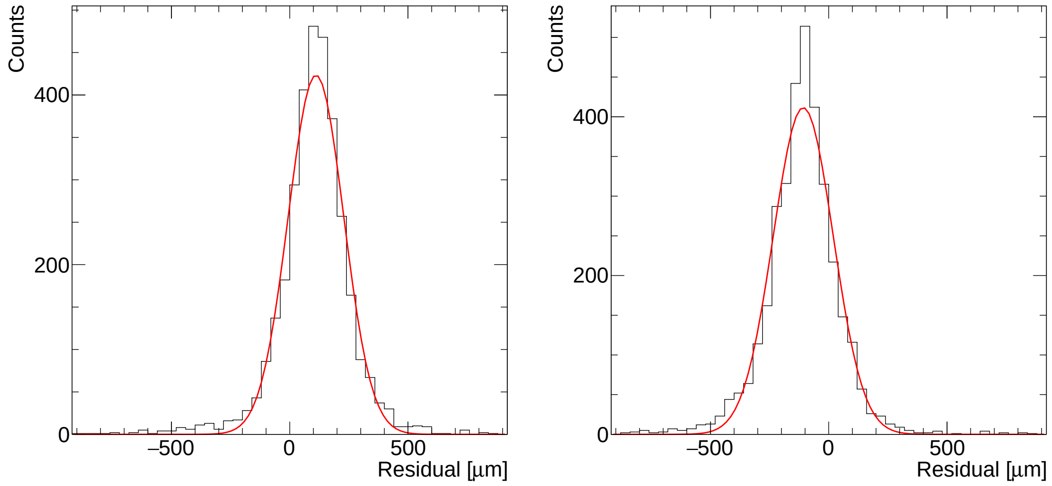

(c) 20 mm 2nd layer X (d) 20 mm 2nd layer Y

Figure 3.16: Distributions of the residuals between calculated positions by the GSO-bar hodoscope and the reference tracker ADAMO. Each plot represents the 20 mm a) 1st X b) 1st Y c) 2nd X, and d) 2nd Y. In this case, injected beam was 200 GeV electron and events inside a 4 mm × 4 mm square around the calorimeter center are selected.

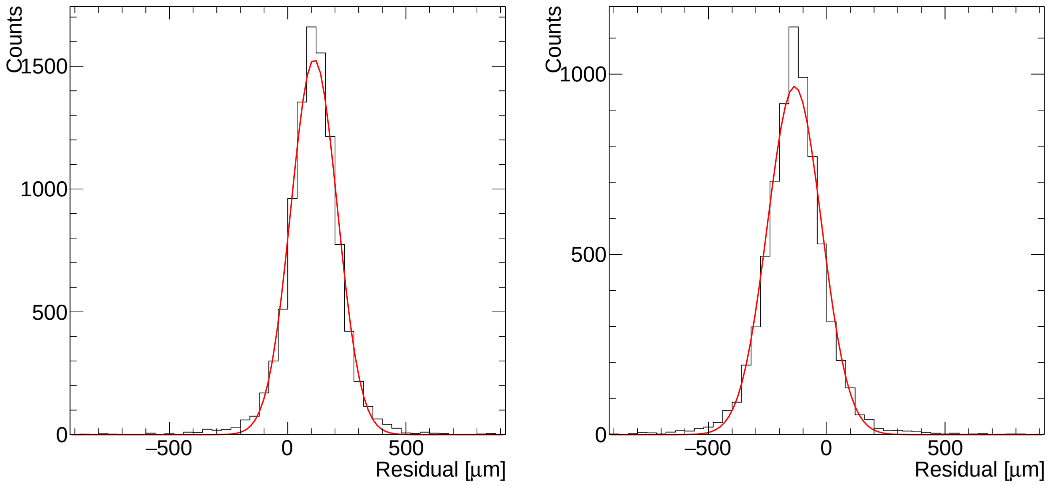

(a) 40 mm 1st layer X (b) 40 mm 1st layer Y

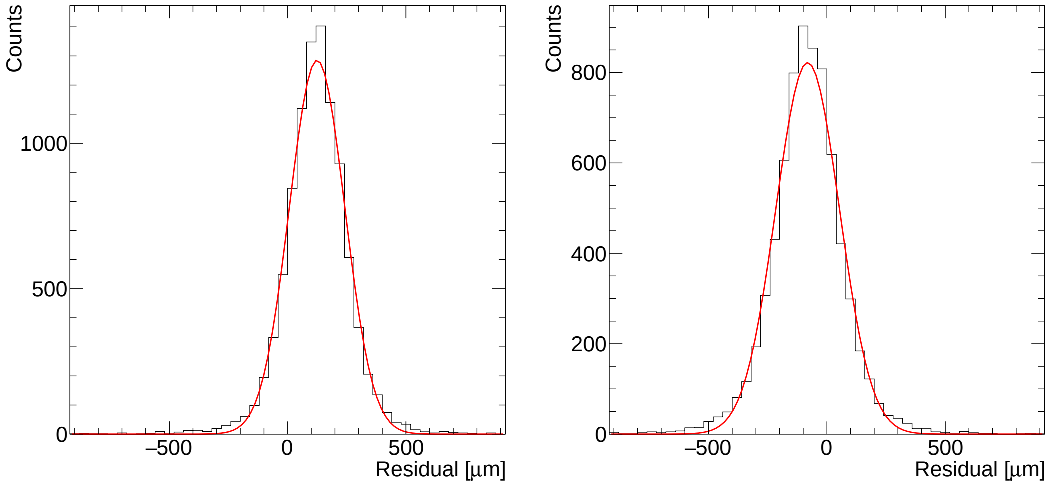

(c) 40 mm 2nd layer X (d) 40 mm 2nd layer Y

Figure 3.17: Distributions of the residuals between calculated positions by the GSO-bar hodoscope and the reference tracker ADAMO. Each plot represents the 40 mm a) 1st X b) 1st Y c) 2nd X, and d) 2nd Y. In this case, injected beam was 200 GeV electron and events inside a 4 mm × 4 mm square around the calorimeter center are selected.

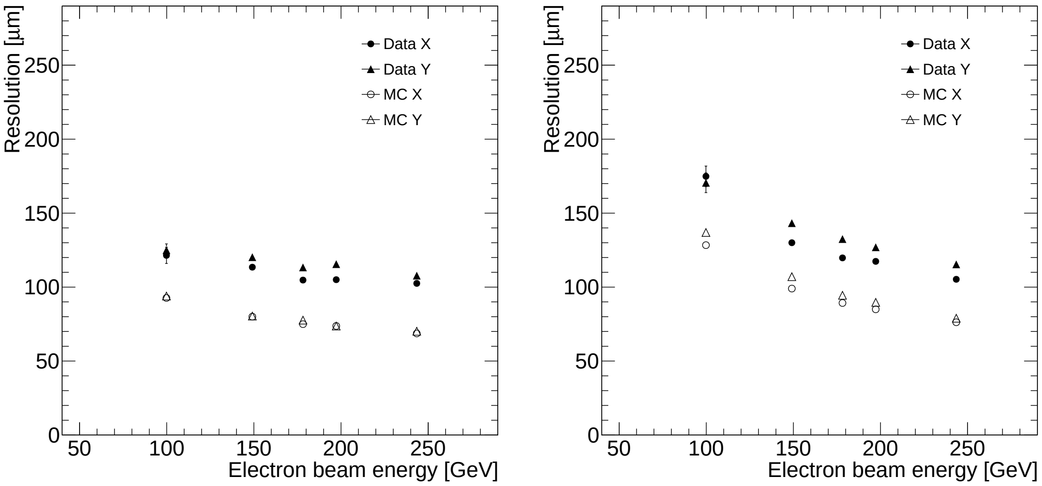

(a) 20 mm 1st layer

(b) 20 mm 2nd layer

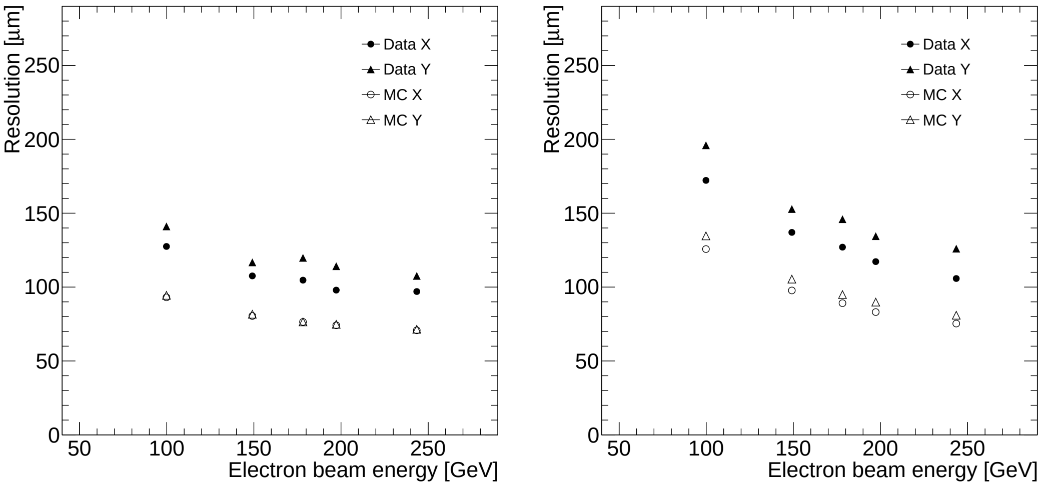

(c) 40 mm 1st layer

(d) 40 mm 2nd layer

Figure 3.18: Position resolution of the GSO-bar hodoscope a) 20 mm 1st, b) 20 mm 2nd, c) 40 mm 1st, and d) 40 mm 2nd layers depending on the injected beam energies. In each figure, black and white points represent the result of data and simulation, respectively. Circles and triangles represent X or Y side of the GSO-bar bundle. Error-bars are plotted, but within the markers in most cases. Note that, in these plots, MC points include, the position resolution of the reference tracker, 30 μm to compare with the data results.

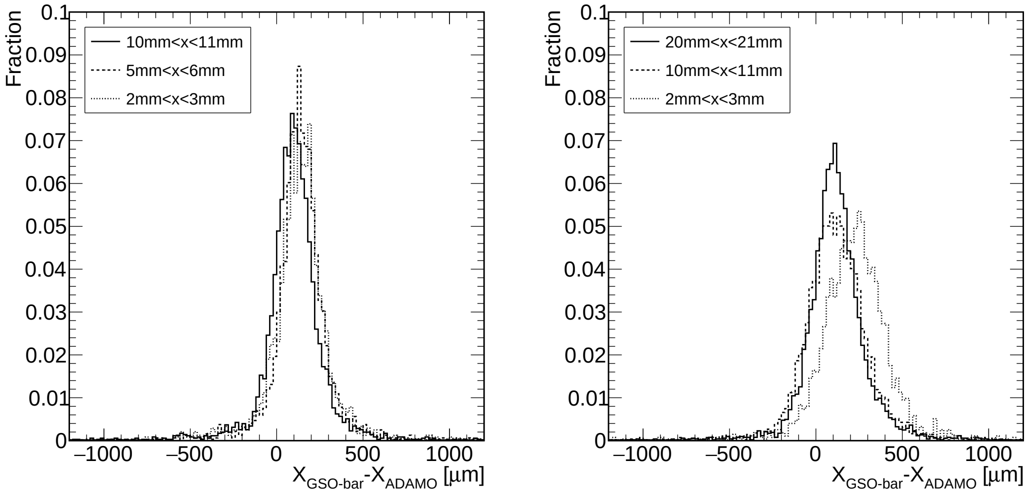

(a) 20 mm calorimeter (b) 40 mm calorimeter

Figure 3.19: Examples of distributions for the residual of the positions between GSO-bar and the ADAMO tracker at three different positions of the first layer of the Arm1 a) 20 mm and b) 40 mm calorimeters. For the 20 mm calorimeter, 2 mm< x <3 mm, 5 mm< x <6 mm, and 10 mm< x <11 mm are selected, while 2 mm< x <3 mm, 10 mm< x <11 mm, and 20 mm< x <21 mm are selected for the 40 mm calorimeter.

The position resolutions as a function of incident position given by the ADAMO tracker are summarized in Fig. 3.20. For the 20 mm calorimeter, obtained position resolutions are independent from the position except at the both side of the 2 mm edge regions for all layers. On the other hand, the resolution becomes slightly worse as the incident position locates closer to the edge for the 40 mm calorimeter.

Figure 3.21 shows the peak shift of the residual distributions depending on the positions. Also in this case, incident position of the particles calculated by the ADAMO tracker are used. As well as the observed results in Fig. 3.19(b), means of the residuals shift larger as the reconstructed positions by the ADAMO tacker are closer to $x(y) = 0$, while the opposite trend can be seen in the other side of the horizontal axis. The position dependence particularly seen in the edge of the calorimeters is not caused by the ADAMO tracker, because the particle tracking is performed before entering the LHCf calorimeters and the detection area of the ADAMO tracker is larger than that of the calorimeters. The results indicate that the position reconstruction near the edge is biased by the uncertainty of the gain calibration of edge channels of the GSO-bar hodoscope. The conversion factors of the GSO-bar hodoscope is determined by using muon data as discussed in Sec. 3.2.2, and the conversion factors are determined properly for most of channles. Due to the difficulty of the muon event selection where a penetrating track is expected, there is a relatively large uncertainty on the calculation of the conversion factors for the edge channels. Constant component of the offset from zero level is due to the precision of the alignment of the ADAMO

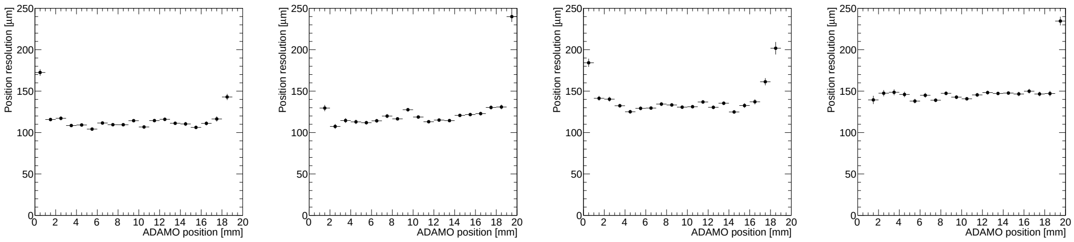

(a) 20 mm 1st layer X (b) 20 mm 1st layer Y (c) 20 mm 2nd layer X (d) 20 mm 2nd layer Y

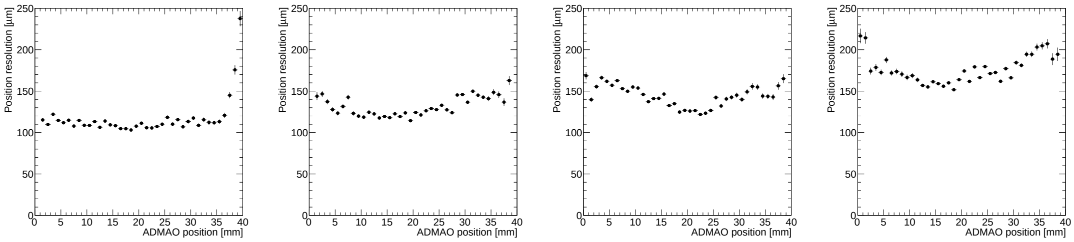

(e) 40 mm 1st layer X (f) 40 mm 1st layer Y (g) 40 mm 2nd layer X (h) 40 mm 2nd layer Y

Figure 3.20: Position dependence of the position resolutions. The horizontal and the vertical axes denote the incident position of the particle reconstructed by the ADAMO tracker and the position resolutions, respectively.

tracker relative to the LHCf calorimeters considering the fact that levels of the offest is similar among the layers. Thus the offset from the zero level is not associated with the LHCf detector itself.

3.3.4 Linearity of the detector responses

The linearity of the energy determination is checked by fitting the relation between S and the energy of the incident particle for all the electron beam energies with a linear function. Figure 3.22 shows the measured S as a function of the incident energy of electron beams. Although the LHCf detectors are designed to measure the particles with the energy up to 6500 GeV, 250 GeV is the highest energy at the beam test. Therefore, only the points with the energies bellow 200 GeV are used for the fitting in order to examine the linearity at the high energy region. Eventually non linearity of the calorimeters, defined as the deviations from the linear fitting at the lower energy, is less than 0.5 % at 200 GeV, 230 GeV (only Arm2), and 250 GeV for all calorimeters of both Arm1 and Arm2 (Fig. 3.23).

Deviations from linearity are smaller than 0.5 % in the whole energy range between 100 GeV and 250 GeV for both Arm1 and Arm2.

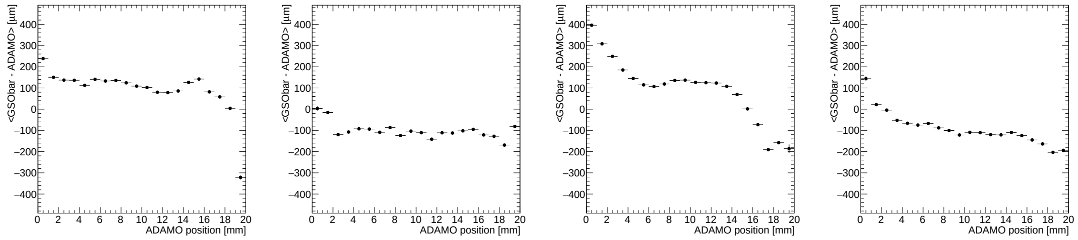

(a) 20 mm 1st layer X (b) 20 mm 1st layer Y (c) 20 mm 2nd layer X (d) 20 mm 2nd layer Y

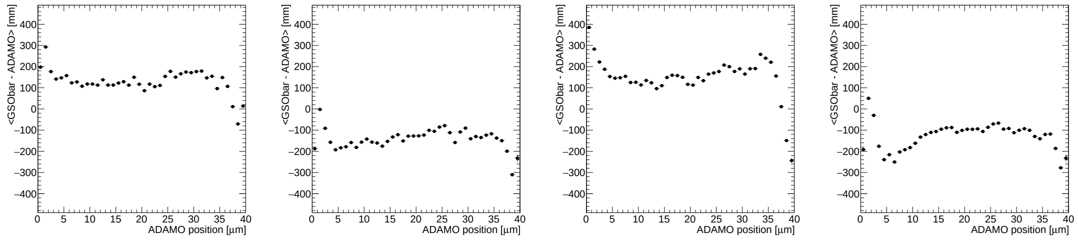

(e) 40 mm 1st layer X (f) 40 mm 1st layer Y (g) 40 mm 2nd layer X (h) 40 mm 2nd layer Y

Figure 3.21: Systematic offsets of the position reconstruction depending on the beam hit positions. Black points shows gaussian-fitted centers of the residual distributions at each beam-hit positions according to the reference tracker, ADAMO. Offsets of baselines from zero seen along y-axis are caused by the alignment between the detector and ADAMO, thus, which are not particular about the detector itself. Steep slopes are seen in the edges in each plots.

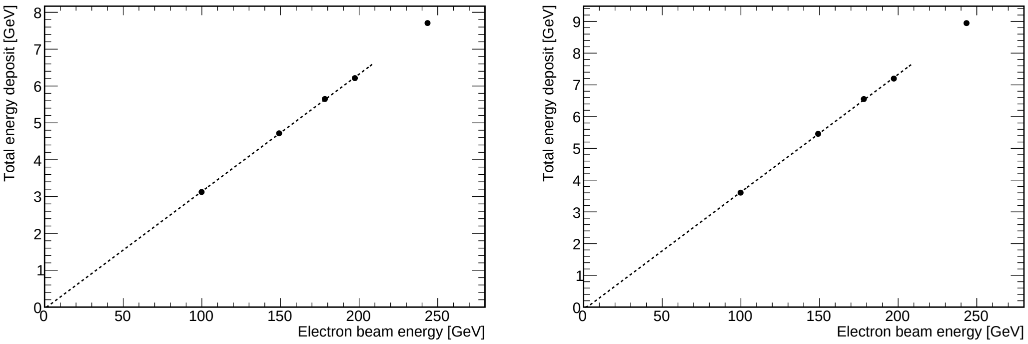

(a) Arm1, 20 mm calorimeter (b) Arm1, 40 mm calorimeter

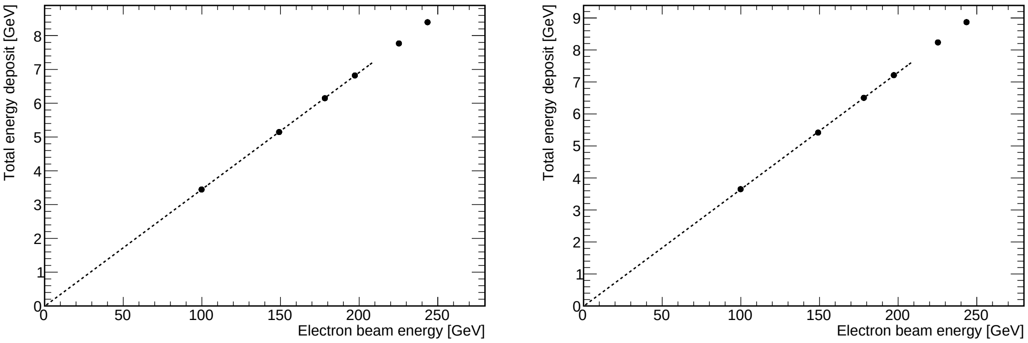

(c) Arm2, 25 mm calorimeter (d) Arm2, 32 mm calorimeter

Figure 3.22: The relation between the energy of the incident particle and S for both the Arm1 and the Arm2 detectors. The black points represent measured data while the fit function is drawn as a dashed line.

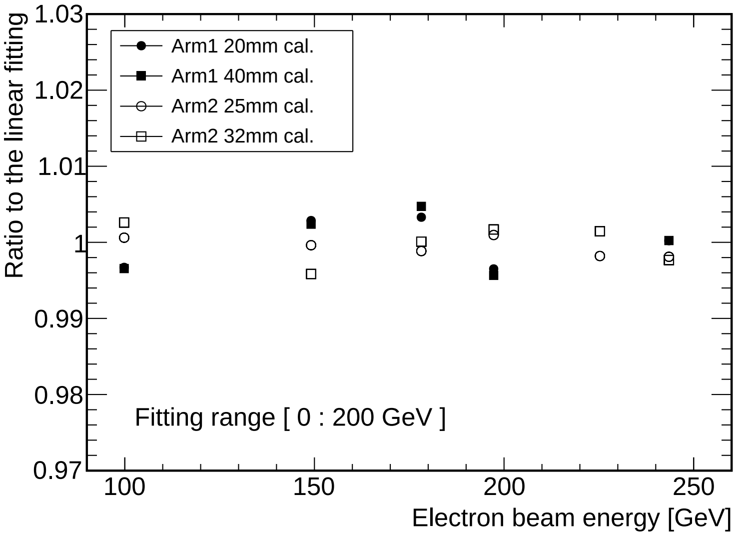

Figure 3.23: Deviation from the fitting results of Fig. 3.22. Black circles, black squares, white circles, and white squares represent the results of the 20 mm and the 40 mm calorimeters of Arm1 and the 25 mm and the 32 mm calorimeters of Arm2, respectively. The points with the energy of 230 GeV and 250 GeV did not join the fittings.

Chapter 4

Data analysis of forward-photon energy spectra in p–p $\sqrt{s}$ =13 TeV collisions

4.1 13 TeV proton-proton collisions at the LHC

4.1.1 The LHCf dedicated run

In 8-13 June 2015, LHCf has successfully completed all programs for 13 TeV proton proton collisions. Fill 3855, on 12–13th June 2015, is used for the photon analysis in this study. Initially the delivered filling scheme was "Multi_39b_37_15_15_4bpi11inj", where 37 bunches and the rest two bunches were filled for colliding at the point1 and the background study associated with residual gas in the beam pipe, respectively. After a RF problem of LINAC, the scheme changed as 29 colliding bunches, and 6 and 2 non-colliding bunches for Beam1 and Beam2, respectively. The beams have the crossing angle of 145 μrad, which is the limit of crossing angle at IP1. This results in the shift of the beam position by 20.45 mm downward at the location of the LHCf experiment as discussed with Fig. 2.10 in Sec. 2.4.4. Owing to the beam crossing, the η acceptance of the LHCf detectors is maximized to $\eta > 8.4$. A beam parameter for the transverse emittance, β^*, is adjusted to 19.11 m so as to achieve a low luminosity condition for LHCf. The beam condition of Fill 3855 is summarized in Tab. 4.1.

Figure 4.1 shows time variation of trigger rate, DAQ efficiency, and counting rate of the Front Counter [35] of the LHCf experiment together with the beam condition during Fill 3855. They are compared with the luminosity measured by the ATLAS experiment [54]. Meeting the requirement of the LHCf experiment, a remarkably low luminosity, an order of 10^{29} cm^{-2}s^{-1} which is five orders of magnitude lower than a nominal condition is achieved by unsqueezing the beam bunches instead of squeezing. The counting rate of the LHCf Front Counter, proportional to the luminosity in this

Table 4.1: Beam condition of Fill 3855

Fill no.	3855
Filling scheme	Multi_39b_37_15_15_4bpi11inj
Duration	14h:05m:26s
Beam energy [GeV]	6500
Crossing angle [μrad]	145 (V)
β^* [m]	19.11

counting range, exhibits the behavior compatible with the luminosity measured by the ATLAS experiment. The trigger rate of LHCf is roughly 400 Hz, where the efficiency of DAQ is a level of 50 %. During the fill, we adjust the beam parameters, such as beam separtation, to satisfy the L3T rate slightly above the maximum DAQ rate with satisfying low pile-up probability. A pile-up event is defined as the event where multiple collisions happen in a single bunch crossing. These pile-up events are crucial for the LHCf experiment because the LHCf detectors are not capable of distinguishing the pile-up events from multiple particles associated with a single collision. Although the fill lasted for 14 hours, the beam condition optimized for the photon analysis is intentionally changed in the middle of the fill for the other physics program, the π^0 analysis, after a confirmation of the statistics of the first program. The pile-up parameter, μ, average numbers of inelastic collisions per one beam crossing, is kept approximately 0.01 during the photon program, while it is 0.03 for the rest of the fill to increase the statistics of π^0 events with a dedicated trigger mode and compromising a slightly high pileup probability. The expected rates of the pile-up event during the operation are approximately 0.3 and 0.6 % for μ=0.01 and 0.03, respectively.

Only the data with $\mu = 0.01$, photon dataset hereafter, is used for the study here. The photon dataset contains 170 LHCf DAQ runs, in which one LHCf DAQ run is equal to 25,000 triggered events, corresponding to live time of 9945.38 seconds. Slow control data (temperatures of electronics and PMTs, applied HV and LV values, manipulator positions, and etc.) are recorded and confirmed to be stable for runs of the photon dataset.

The integrated luminosities of every LHCf DAQ runs are then calculated by the luminosity provided by ATLAS and the DAQ efficiency. The averaged luminosity and DAQ efficiency during each LHCf run are used for the calculation. Eventually the integrated luminosity for all the photon dataset is 0.1905 nb^{-1} for both Arm1 and Arm2, corresponding to 1.5×10^7 inelastic collisions assuming the inelastic cross-section of 78.53 mb at $\sqrt{s}$ =13 TeV, which is extrapolated by previous measurement up to $\sqrt{s}$ =8 TeV of total and elastic cross-sections [1, 53]. The uncertainty of the luminosity measurement by the ATLAS experiment here is 1.9 % [54].

In the following sections, the inclusive photon analysis is discussed with the Arm1 detector. The analysis procedure of the Arm2 detector is essentially same as Arm1,

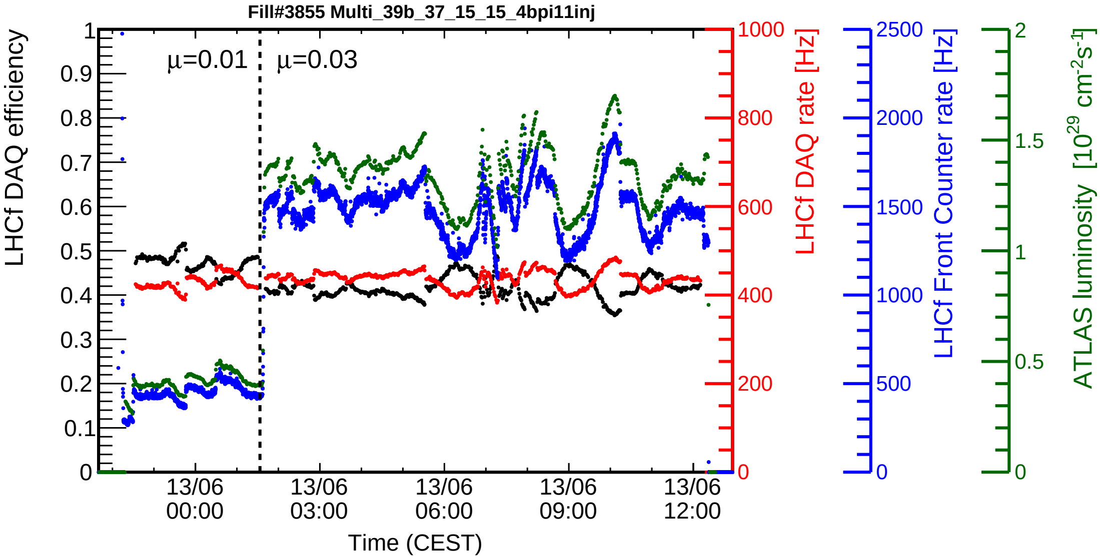

Figure 4.1: DAQ during Fill 3855. The DAQ rate, DAQ efficiency, and count rate of Front Counter of the LHCf experiment are shown in black, red, and blue, respectively. Luminosities measured by the ATLAS experiment is shown in green points. The vertical dotted line shown in the plot represents the boundary of the two different beam condition, μ=0.01 and μ=0.03. Only the data with μ=0.01 is used for the photon analysis.

and the results of the both detectors are combined eventually in Sec. 4.6.1.

4.1.2 Trigger efficiency

In order to evaluate the trigger efficiency of the photon event in the dataset, firstly the detection efficiencies of sampling layers are calculated. The detection efficiency of each sampling layer is defined as the fraction of the events in which the sampling layer issues the hit flag out of the all events. Here all events include the ones in which the Arm2 detector issues the trigger independent from the Arm1 detector, thus these are no bais trigger for Arm1. The obtained efficiency as a function of measured energy of the Arm1 20 mm calorimeter are shown in Fig. 4.2 as examples. The positions of the cutoff energy, around 600 MeV, vary depending on the sampling layers due to the difference of the signal baselines of each layer.

By using the obtained efficiency curves we compute the efficiency of issuing a shower-trigger by the calorimeter compared with the energies deposited in each layer according to MC simulations. The shower-trigger requires three successive layers having hit flags as discussed in Sec. 2.4.3.

Figure 4.3 shows the photon trigger efficiencies of the Arm1 calorimeters as a function of incident energy. The efficiency becomes nearly 100 % above 200 GeV of photon energy for both calorimeters. The difference of the cutoff positions between

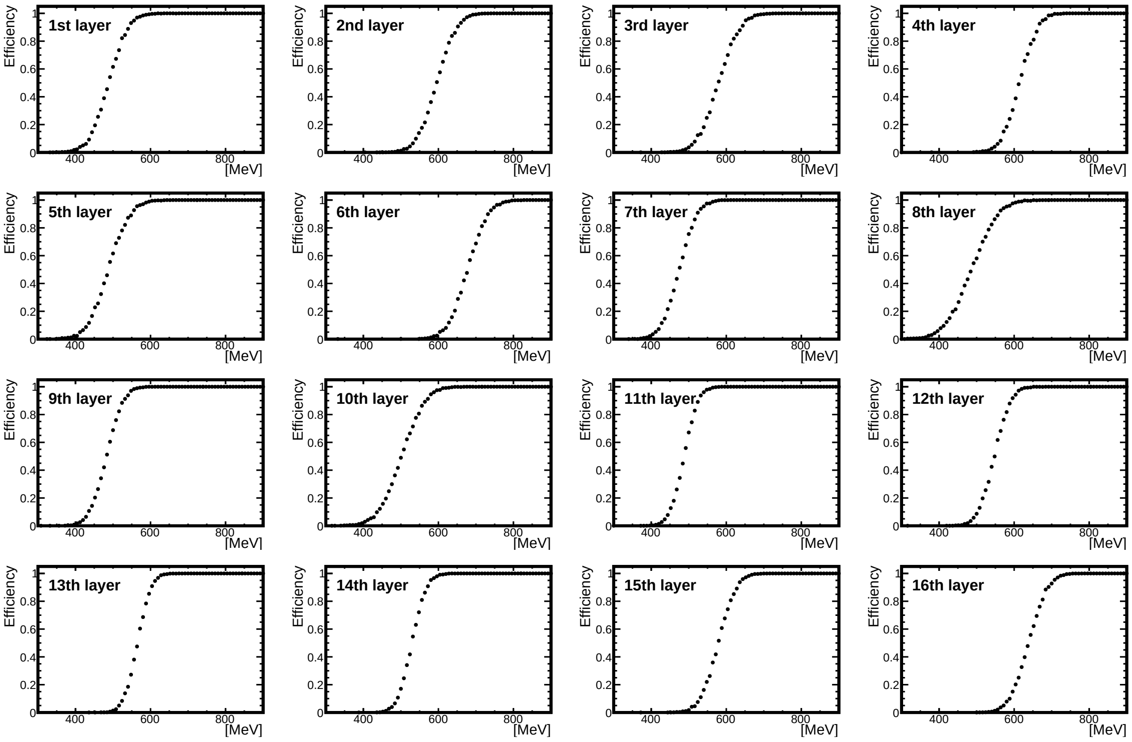

Figure 4.2: The detection efficiencies of the 16 sampling layers of the Arm1 20 mm calorimeter. The horizontal and the vertical axes denote the measured energy deposition in MeV, and the fraction of the events in which the sampling layer issues a hit flag.

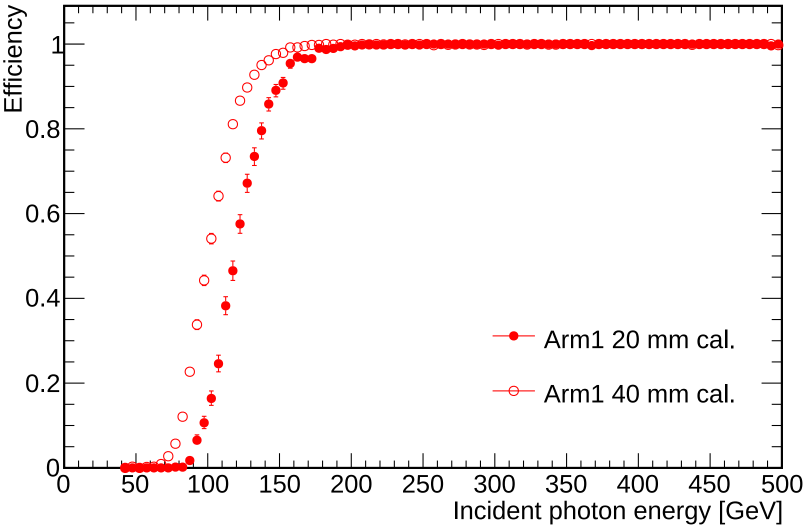

Figure 4.3: The trigger efficiencies for photons as a function of the energy. Red open and filled circles represent the efficiencies of the Arm1 40 mm and 20 mm calorimeters, respectively.

the 20 mm and the 40 mm calorimeters is originated from the baseline of the signal and applied high voltage of each sampling layer.

4.2 Detector simulation

The full detector simulations with use of Cosmos 7.645 / EPICS 9.165 package begins from the particle generation at the interaction point. QGSJETII-04 [25] is chosen for the reference model with statistics of 10^8 inelastic collisions, while approximately 3×10^7 inelastic collisions with EPOS-LHC [24] are also prepared for the studies of systematic uncertainty due to the model dependence. Particles generated at the interaction point are transported to the detector position, in which the simulation includes the influence of the materials of the triplets of quadrupole focusing magnets, the beam seperation magnets, and the beam pipe structures as well as megnetic fields. The detector response to the incident particles is simulated as described in Chap. 3 with taking into account of the experimental situations, e.g. measured noise fluctuations, during Fill 3855.

Apart from the full detector simulation, to compare with the unbiased photon spectrum obtained by the photon analysis, 10^8 inelastic collision events are generated with each of hadronic interaction model via the Cosmic Ray Monte Carlo (CRMC) package [62]. The models chosen in this study are, DPMJET 3.06 [27], QGSJETII-04, EPOS-LHC, SIBYLL2.1 [26], SIBYLL2.3 [32], PYTHIA 8.212 [28].

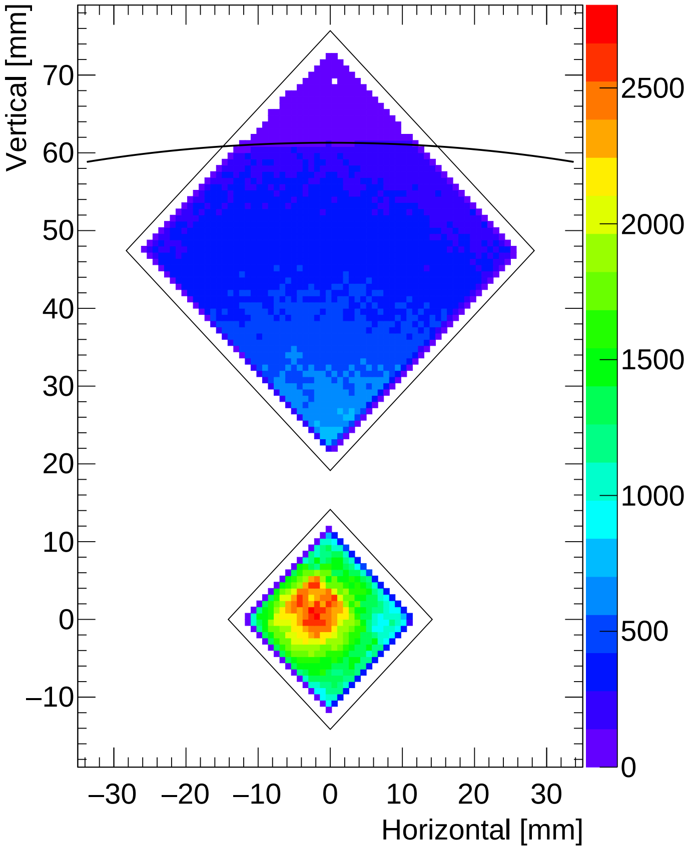

Figure 4.4: The distirbution of the reconstructed positions of the single-hit events with the energy above 100 GeV (EM-equivalent) after the 2 mm edge cut.

4.3 Event reconstruction and selection

In this section, the steps of the event selection to obtain the single photon events at $\eta > 10.94$ and $8.99 > \eta > 8.81$ are introduced. The event selection follows the steps, namely *energy cut*, *multi-hit cut*, *acceptance cut*, and *hadron cut*. Figure 4.4 shows the hit distribution of the measured events in the photon dataset. The distribution of the reconstructed incident position of the particles shown in Fig. 4.4 contains all the single-hit events above 100 GeV except the 2 mm edges of the calorimeters.

After the single photon selection, 44,756 and 41,742 events for $\eta > 10.94$ and $8.99 > \eta > 8.81$ are remained in the photon spectrum.

4.3.1 Energy reconstruction

The energy of the incident particles is reconstructed using the energy estimator S. Figure 4.5 shows the conversion functions, $J(S)$ in Eq.2.1, which provides the incident photon energy. The conversion functions are estimated by the simulations,

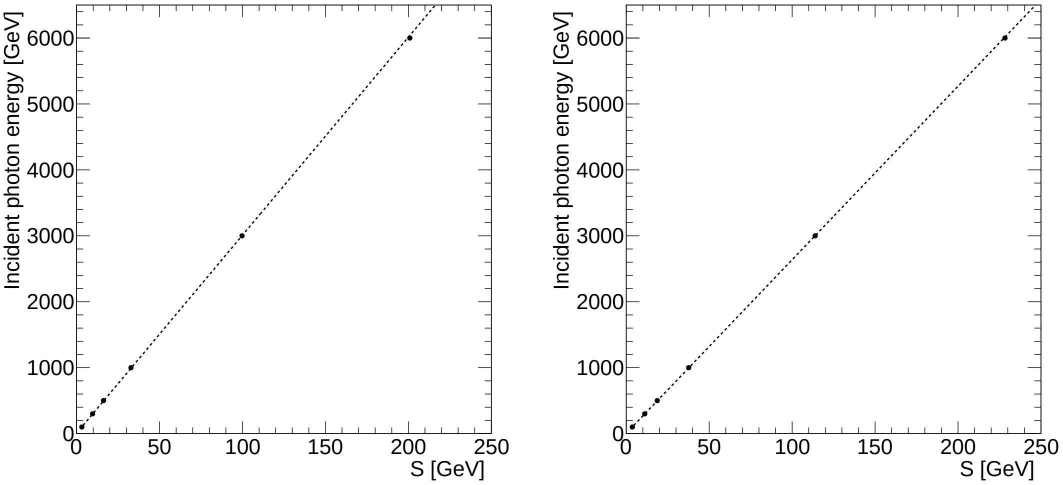

(a) Arm1 20mm calorimeter

(b) Arm1 40mm calorimeter

Figure 4.5: Incident photon energies as a function of sampled energy, S of a) the 20 mm and b) the 40 mm calorimeters. Dashed curves represent the second-order polynomial fitting results.

where electrons with six mono-energies of 100 GeV, 200 GeV, 500 GeV, 1000 GeV, 3000 GeV, and 6000 GeV injected in a 1 mm × 1 mm square at the center of the calorimeters. Obtained S distributions are then fit with Gaussian functions to determine the expected S corresponding incident photon energies. The functions $J(S)$ shown by the curves in Fig. 4.5 are obtained from the results of second-order polynomial fitting for each calorimeter. Eventually the deviations from the fitting results are less than 0.5 %, while those from the linear fittings are 1 %, which is slightly worse in the lower energy. The difference of the configurations from those at the calibration test in Chap. 3, such as the applied high voltages to PMTs, are taken into account for the configuration at the LHC. Associated uncertainties about the energy scale is discussed in Sec.4.5.5.

Although the energy reconstruction is fully based on the calibration result at the SPS, a re-scaling factor is applied for the LHC 13 TeV analysis. The pair of calorimeters in the LHCf detectors allows us to detect π^0 which decays into two photons almost at the collision point. π^0 events are able to identified by a corresponding mass peak in the the reconstructed invariant mass distribution of two gamma rays. Thus the reconstructed mass peak is able to be used for the calibration of the energy scale during the operation. Figure 4.6 is the reconstructed invariant mass distributions of measured data and MC with QGSJETII-04, in which each calorimeter detected a photon-like particle. The peak in the measured invariant mass distributions is fit with a Gaussian function with a Chebyshev polynomials term as the combinatorial background, in which independent two photons were accidentally detected by the de-

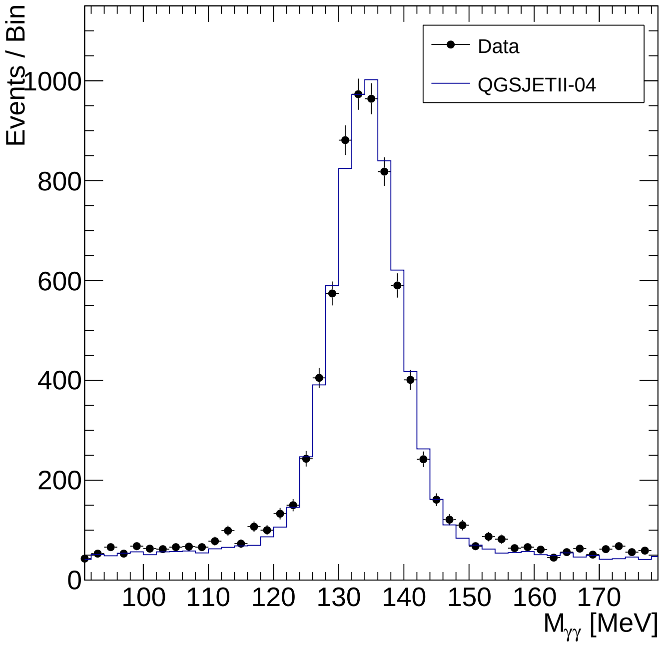

Figure 4.6: Invariant mass distributions of photon pairs of the experimental data after applying the rescaling factor and MC.

tector at the same time. The measured π^0 mass peak of Arm1 is 129.58 MeV, while that of MC is 134.16 MeV. Therefore, the difference 3.5 % is used as the re-scaling factor in the energy reconstruction to correct the data. The shift of the reconstructed mass peak from 135 MeV observed in the data is consistent with the uncertainty of the energy scale, 3.4 %, estimated in Chap. 3.

4.3.2 Position reconstruction and the multi-hit rejection

The position information of the particles is determined by the 16 shower-lateral distributions (i.e. four layers of x and y directions in two calorimeters) measured by the GSO-bar hodoscopes.

The hit position and the number of hit particles are calculated by the position reconstruction algorithm. Although the performance of the single shower detection, such as the position resolution, is already discussed in Chap. 3, a detailed study about the single/multi-hit identification is required for the 13 TeV analysis. A multi-hit event is defined as the event where multiple particles hit a calorimeter. In this study, we cut multi-hit events because energy reconstruction of each particle is difficult. Therefore, we cut the multi-hit events and correct their contribution after calculating the single photon spectra.

Figure 4.7 demonstrates a multi-hit event where two photon-like particles hit the 40 mm calorimeter. The top and the bottom plots represent x and y sides of the GSO-bar hodoscope layers, respectively. Two shower distributions are clearly observed in

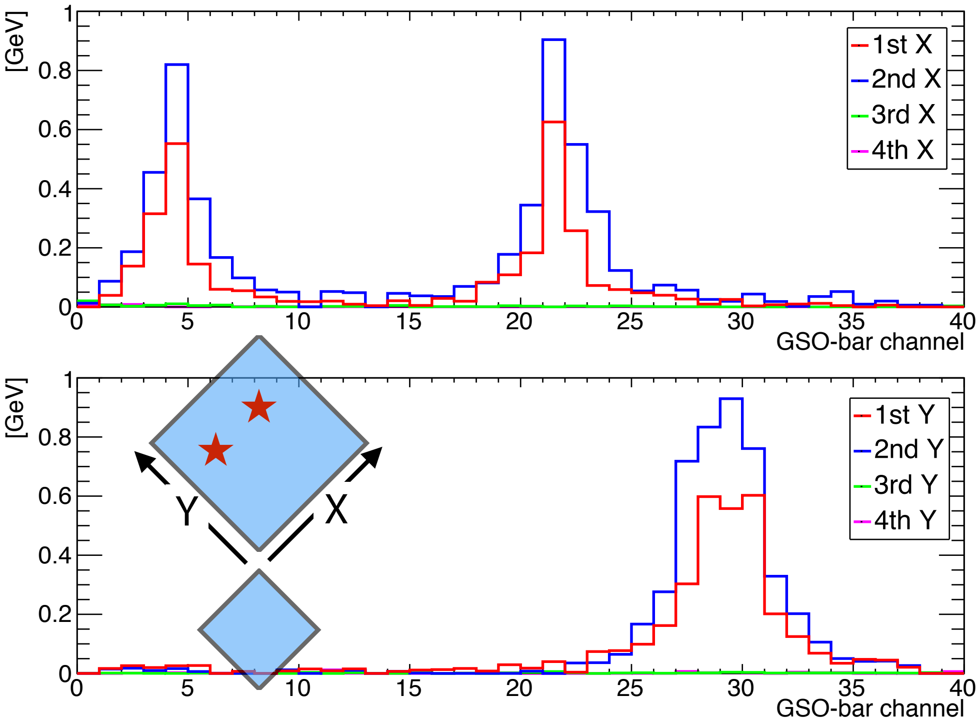

Figure 4.7: A multi-hit event sample measured in the photon dataset. Photon-like particles hit the 40 mm calorimeter and developed the cascade shower in the first and second layers of the GSO-bar hodoscope. Top and bottom plots corresponded to x and y-sides, respectively. Left-bottom illustration of the calorimeters indicates the possible impact points of two photons marked by stars.

the x side of the GSO-bar hodoscope, while it is not clear in the y side. A possible impact points of two photons seen in this event is illustrated in left-bottom of Fig. 4.7.

Figure 4.8 shows the fraction of the multi-hit events in the photon spectra calculated by QGSJETII-04. Only photon-like events with the reconstructed energies above 200 GeV are selected in Fig. 4.8. Contribution of the multi-hit events increases as the energy increases and it becomes dominant above few TeVs. If a multi-hit event is recognized as a single-hit event, it leads a substantial overestimation of a reconstructed energy. Since a photon energy spectrum is expected to be exponential-like shape, miss identification of multi-hit events makes the energy spectrum much harder. Multi-hit identification has been thought to be a challenging issue for the GSO-bar hodoscope of Arm1 due to the sampling pitch of 1 mm. Typically, a half-width at the half-maximum of EM cascade showers measured by the GSO-bar hodoscope layers is less than 1 mm independent from the energy in the medium of the tungsten absorber.

Firstly the position reconstruction algorithm begins the first-level peak search to all the shower lateral distributions measured by the GSO-bar hodoscope layers based on TSpectrum [56] implemented in the ROOT library [57]. A peak search method of

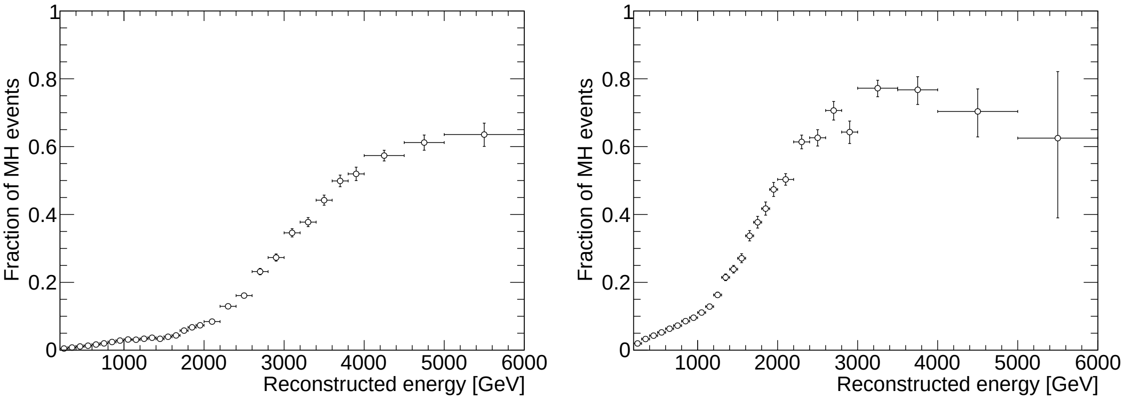

(a) 20 mm calorimeter

(b) 40 mm calorimeter

Figure 4.8: Fractions of the multi-hit events expected in the photon spectra of the 20 and 40 mm calorimeters. QGSJETII-04 is used for the estimation.

TSpectrum provides the positions of peaks satisfying given conditions of a width and peak heights lying on the background distribution. We did not set strict constraints on these conditions at this level. Information of peaks found by the first-level peak search, such as peak positions and their heights, are used as the initial parameters for the fitting of the shower lateral distributions. The fitting function is exactly same as Eq. 3.3. For the multi-hit fitting, a linear sum of Eq. 3.3 is used.

Following the output of the initial peak-search method, single and multi-hit fittings are performed simultaneously in any case. A peak height of fitted shower lateral distribution is required to be more than 50 MeV in order to reject noise peaks. Also, if the distance between reconstructed two peaks is less than 3 mm, the multi-hit fitting is rejected because the multi-hit fitting is not reliable in such case considering the 1 mm pitch of the hodoscope. Finally, the algorithm calculates chi-squares in order to evaluate goodness of fit for both single and multi-hit fittings. If the multi-hit fitting satisfies the criterion, such as the energy threshold, the distance of two peaks and the goodness of fit, we recognize it as a multi-hit event.

Using information of the number of hits in the x and y-sides of the 1st and the 2nd layers, the algorithm distinguishes multi-hit events from the single-hit events. For the photon analysis, the 3rd and the 4th layers locating at 30 X_0 and 42 X_0, respectively, are not used for multi-hit identification, since EM showers do not reach such layers. The events satisfying two hits in 'x and y-sides of either layer' or 'the 1st and the 2nd layer of either side' are classified as multi-hit events. Although multi-hit events are cut in the spectrum calculations, the contribution of such photons in each energy bin of the inclusive photon spectrum is compensated in the spectrum unfolding process. The details are discussed in Sec.4.4.1.

The performance of the single and multi-hit indentification algorithm is examined experimentally. In the following, we focus on the study of the single and the multi-hit

Table 4.2: Single-hit detection efficiency of the 20 mm calorimeter for 200 GeV electron beams. Single-hit detection efficiency is defined as the fraction of the events properly tagged as single-hit out of the all single-hit samples.

Threshold [MeV]	Total events	Single-hit tagged	Multi-hit tagged	Detection eff.
5.0	2355	2110	245	0.896
30.0	2355	2283	72	0.969
50.0	2355	2311	44	0.981

Table 4.3: Single-hit detection efficiency of the 40 mm calorimeter for 200 GeV electron beams. Single-hit detection efficiency is defined as the fraction of the events properly tagged as single-hit out of the all single-hit samples.

Threshold [MeV]	Total events	Single-hit tagged	Multi-hit tagged	Detection eff.
5.0	5983	5245	738	0.877
30.0	5983	5789	194	0.968
50.0	5983	5865	117	0.980

detection efficiencies of the algorithm.

In order to estimate the single-hit detection efficiency of the algorithm experimentally, the data taken at the SPS is again used. Detection efficiency for single hit is examined by applying the position reconstruction algorithm to the data where 200 GeV electron beams are exposed to each calorimeter at SPS. The track information of the ADAMO tracker with the position resolution of 30 μm is used to avoid multi-hit events. With a threshold value for peak height of 50 MeV, 2,311 out of 2,355 single-hit events and 5,865 out of 5,983 single-hit events are properly tagged as single-hit events in the 20 mm and the 40 mm calorimeters, respectively, as summarized in Tab. 4.2 and 4.3. The algorithm has the capability of single-hit detection efficiency greater than 98 % for 200 GeV photons. The efficiency is expected to improve as the energy increases. The algorithm applied to the MC simlation shows the single-hit detection efficiency greater than 99 % above 200 GeV photons with a dataset of pure single-hit samples. The single-hit detection efficiecies of the actual data and MC show good agreement considering the possible contamination of the multi-hit events.

The selection efficiency of the multi-hit events in p–p $\sqrt{s}$ =13 TeV at the LHC is evaluated by using the artificial multi-hit samples. Lateral distributions of single EM shower events in various energy ranges are extracted from the measured data at the LHC as shower templates.

In order to make artificial multi-hit samples, a pair of primary and sub showers are superposed according to the two-dimensional probability function depending on the energy of the primary shower. The function reproduces the ratio of sub to primary energies of particles and the distance of incident positions between sub and

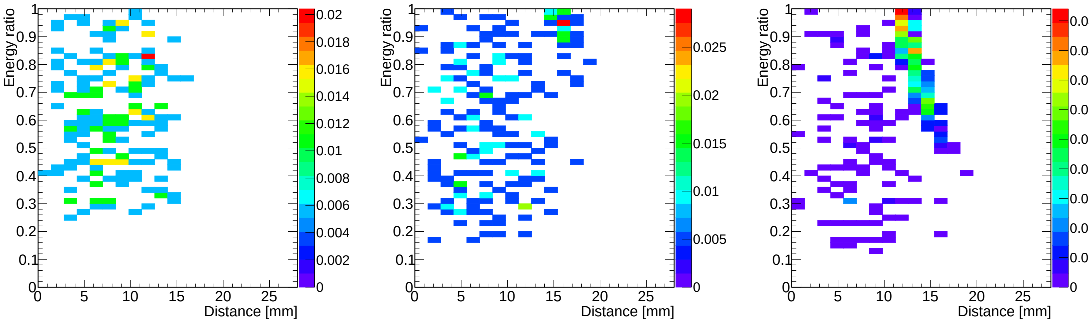

(a) 800-900 GeV (b) 1200-1300 GeV (c) 1600-1700 GeV

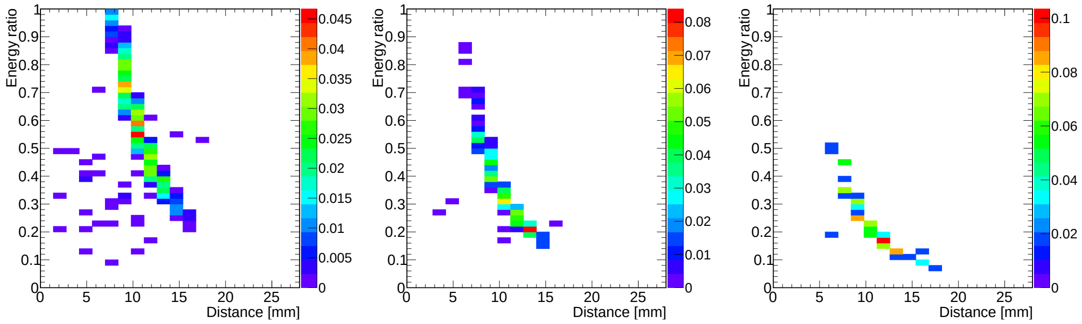

(d) 2400-2500 GeV (e) 3200-3300 GeV (f) 4000-4100 GeV

Figure 4.9: The two-demensional probability functions of multi-hit events for the Arm1 20 mm calorimeter obtained from the MC simulation with QGSJETII-04. Six of energy ranges are shown as samples. The horizontal and vertical axises represent distance between two shower-peaks and energy ratio to primary showers, respectively. Arc-like structures seen in the high energy regions are made by neutral pion decays.

primary particles. Here primary and sub particles correspond to the particles which have higher and lower energies, respectively. The probability functions are determined using QGSJETII-04. Figures 4.9 and 4.10 show the two-dimensional probability functions in several energy ranges of the higher energy photons for the 20 mm and 40 mm calorimeters, respectively. In the lower energy region, Fig. 4.9(a) for instance, the energy ratio and the distance between two peaks are uniformly distributed, while clear arc-like structures are seen in the higher energy region. These arc-like structures are the events in which two photons decayed from neutral pions. As the energies of photons increase, contribution of neutral pion events becomes more dominant. Such neutral pion events having larger distance between two peaks, more than 5 mm in most case, leads high detection efficiency of multi-hit events. Using the artificial multi-hit event samples, the algorithm of multi-hit identification is examined whether each event is properly identified as multi-hit or not event by event. Simulation data is also tested as well as the procedure of the data analysis.

Figure 4.11 shows the multi-hit detection efficiency as a function of the measured energy both for the data and the simulation. The efficiency is defined as a fraction

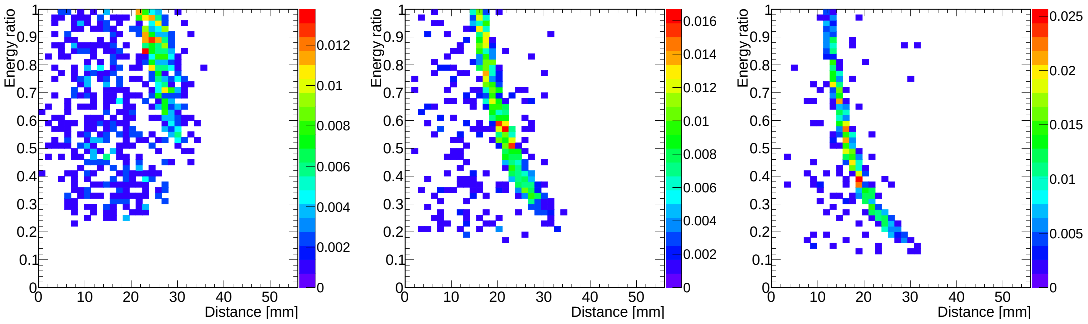

(a) 800-900 GeV (b) 1200-1300 GeV (c) 1600-1700 GeV

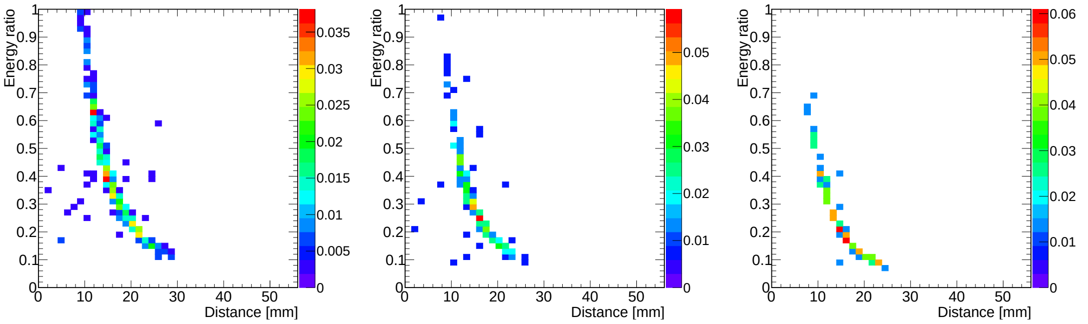

(d) 2000-2100 GeV (e) 2400-2500 GeV (f) 2800-2900 GeV

Figure 4.10: The two-demensional probability functions of multi-hit events for the Arm1 40 mm calorimeter obtained from the MC simulation with QGSJETII-04. Six of energy range are shown as samples. The horizontal and vertical axises represent distance between 2 shower peaks and energy ratio to primary showers, respectively. Arc-like structures seen in the high energy regions are made by neutral pion decays.

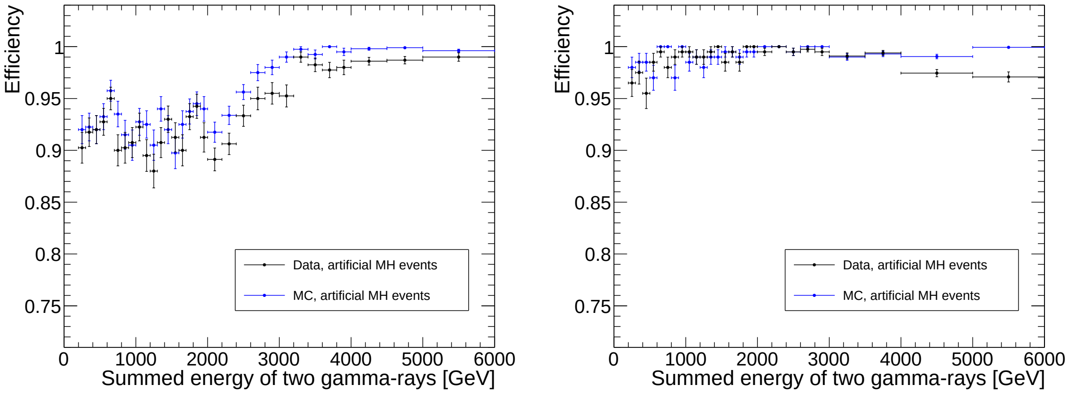

(a) 20 mm calorimeter

(b) 40 mm calorimeter

Figure 4.11: Multi-hit detection efficiency as a function of total measured energies of the 20 mm calorimeter (left) and the 40 mm calorimeter (right). Here the efficiency is defined as the ratio of events tagged as multi-hit over all multi-hit events in each energy range. A probability function of energy ratio and distance between peaks based on MC simulation (QGSJETII-04) are used in this analysis.

of the events identified as multi-hit properly out of all the artificial multi-hit events. Efficiency shows its minimum, approximately 0.9, around 1000 GeV before increasing up to nearly 1 for the 20 mm calorimeter. In contrast to the 20 mm calorimeter, efficiency keeps above 0.95 for the 40 mm calorimeter. The observed difference between the 20 mm and 40 mm calorimeters is not originated from the detector performances, but the difference in the distribution of secondary particles as shown in Fig. 4.9 and 4.10. Basically a large fraction of the multi-hit events seen in the 40 mm calorimeter is the neutral pion events because of its large aperture, whereas there is a large number of accidental multi-hit photons at the low energy of the 20 mm calorimeter.

Figure 4.12 shows the ratio of multi-hit detection efficiencies of MC to experimental data wchich are shown in Fig. 4.11. The inconsistency of the responses becomes 4 % at the maximum below a few TeVs. The observed inconsistency of the multi-hit detection efficiecncy could be a systematic uncertainty of a photon spectrum, because the multi-hit correction that is discussed in Sec. 4.4.1 is performed assuming the detector responses of the actual data and MC are same. The systematic uncertainty arising from these difference of the multi-hit selection efficiencies is discussed in Sec. 4.5.3.

4.3.3 Beam center and the acceptance cut

A scattered angle of a particle is measured from the distance between the incident position and the "beam center" at the GSO-bar hodoscope. The beam center is calculated by the two-dimensional hit map of neutrons as their emission is concentrating

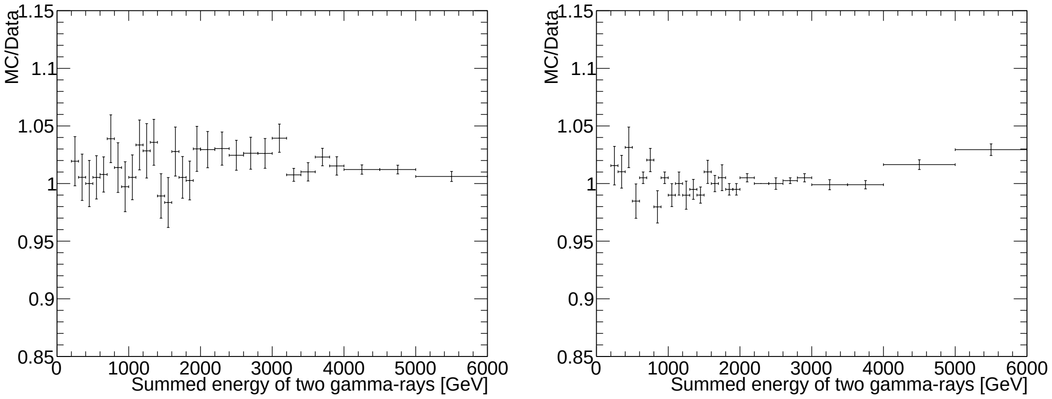

(a) 20 mm calorimeter (b) 40 mm calorimeter

Figure 4.12: The ratio of efficiencies for MC to data (original curves are shown in Fig. 4.11) of (left) the 20 mm and (right) the 40 mm calorimeters.

in the very forward angle, especially for higher energy neutrons. Therefore, we select high energy neutrons above 1.5 TeV from the reconstructed events. Figure 4.13 is the distribution of the reconstructed hit positions of neutron-like events plotted in the coordinate of the 20 mm calorimeter after a hadron-enhance selection. The obtained distribution is fit with the following two-dimensional exponential function to define the beam center,

$$f = Ae^{-B\sqrt{(x-x_0)^2+(y-y_0)^2}}, \tag{4.1}$$

where x_0 and y_0 are the beam center in the coordination of the Arm1 20 mm calorimeter. The distribution in Fig. 4.13 is fit resulting in $x_0 = 9.57\pm0.03$ mm and $y_0 = 12.46\pm0.03$ mm, respectively. Projections of the neutron incident positions with the beam center fitting are shown in Fig. 4.14. The calculated beam center locates in 2.5 mm away from the center of the 20 mm calorimeter. Small spikes are found around the peaks of the distributions owing to the uncertainty of the gain calibration at the third and the fourth layers of the GSO-bar hodoscope.

Stability of the calculated beam center is also evaluated because it could be changed depending on the beam condition provided by the LHC. Figure 4.15 shows beam center positions calculated for every 20 DAQ runs, equivalent to approximately 20 minutes, of the dataset for the photon analysis. Observed variation is mostly consistent with the errors of each point and is ±0.3 mm by taking min-max of the variation. Even though the level of the variation is almost compatible with the position resolution better than 0.2 mm, the systematic uncertainty of the beam center position on the spectra discussed in Sec. 4.5.1 is assigned to ±0.3 mm.

For the photon analysis, the η regions of $8.99 > \eta > 8.81$ and $\eta > 10.94$ as same as the previous 7 TeV photon analysis [38] are selected for the fiducial area to calculate the photon spectra. Reconstructed position distribution of the selected

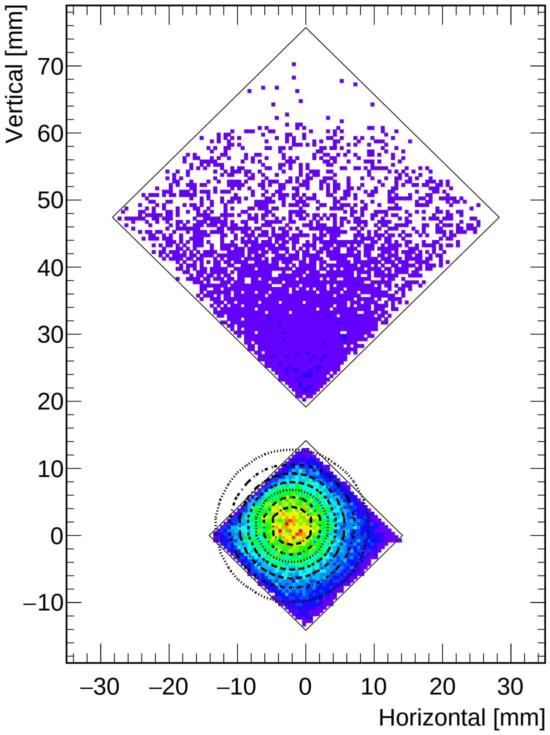

Figure 4.13: The distribution of the reconstructed hit positions of neutron-like events having the energy above 1.5 TeV. Black circles on the 20 mm calorimeter is the result of two-dimensional exponential fitting.

single photon events after the acceptance cut is shown in Fig. 4.16. No significant spike-like structures are found in those regions. In order to reduce the systematics associated with the edge of the calorimeters, the fiducial area is limited to rotation angles of $\Delta\phi = 180°$ and $\Delta\phi = 20°$ for $8.99 > \eta > 8.81$ and $\eta > 10.94$, respectively.

4.3.4 Particle identification (PID)

Particles detected by the LHCf detectors are classified as photon-like or hadron-like events. Here hadron-like events are mostly neutrons, since charged particles are swept away by the dipole magnets between the interaction point and the detectors. Photon events are extracted and hence other hadronic particles are rejected via the particle identification (PID) process by using information of longitudinal development of the cascade shower in the calorimeters. To evaluate the longitudinal development of the induced cascade shower quantitatively, we introduce a cut parameter $L_{90\%}$. $L_{90\%}$ represents the longitudinal depth in the unit of radiation length, where the measured energy deposit reaches 90 % of the total measured energy-deposit in the calorimeter. The difference of the cross sections leads a $L_{90\%}$ distribution of photons having the sharp peak at low $L_{90\%}$ due to the rapid energy loss of EM cascades, while that

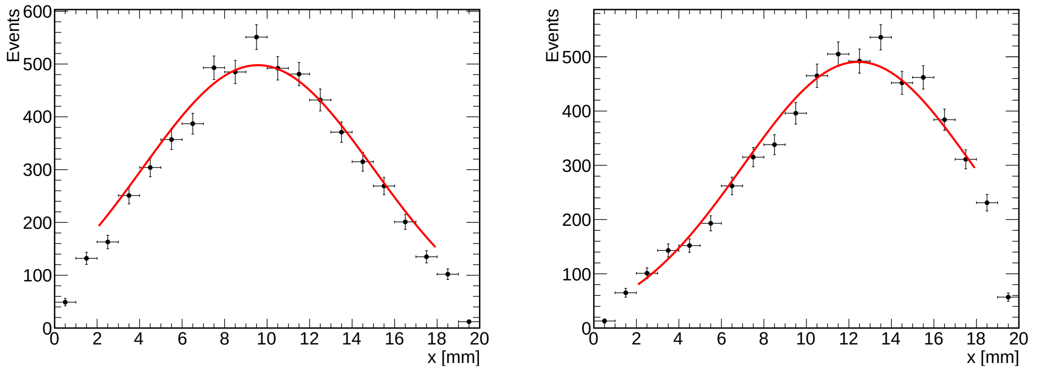

(a) 20 mm cal. X=10–11 mm

(b) 20 mm cal. Y=12–13 mm

Figure 4.14: The a) x and b) y-projections, of Fig. 4.13, of the neutron distributions and those fit results. 10–11 and 12–13 mm for x and y, respectively, where calculated beam center locates, are extracted. Black points and red lines represent data and fit results, respectively.

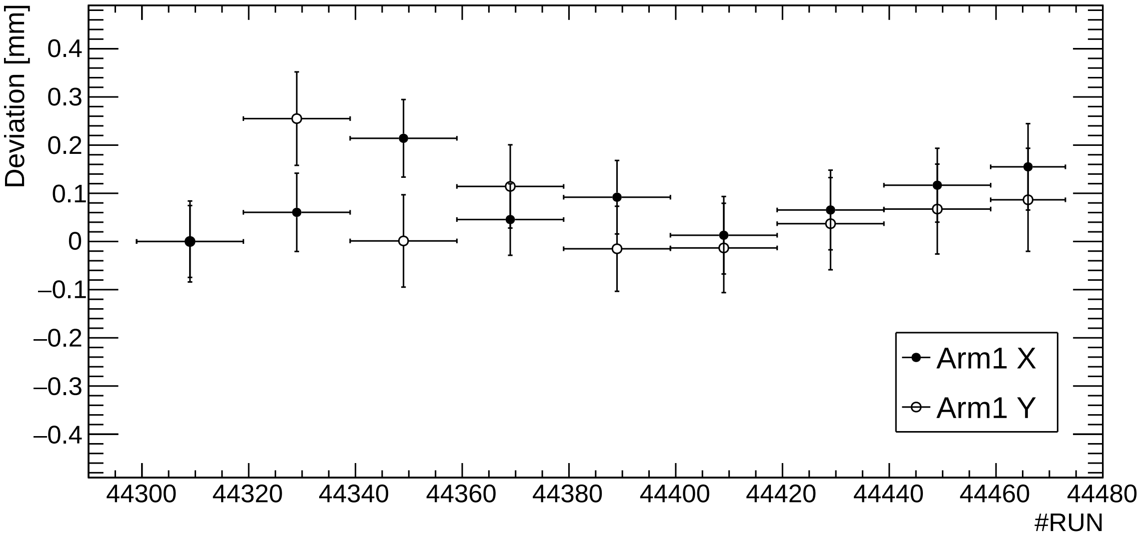

Figure 4.15: X and Y positions of the calculated beam centers as a function of LHCf DAQ runs during the photon dataset. Black and white markers are x and y, respectively. All points are normalized to the first points. Bars on the points represent the fitting errors at each beam position.

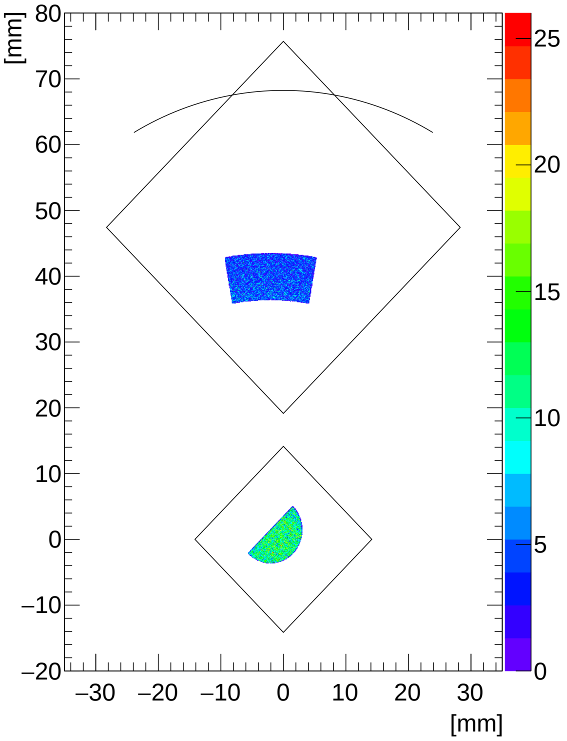

Figure 4.16: The distribution of the reconstructed positions of single photons entering the two of η regions, $8.99 > \eta > 8.81$ and $\eta > 10.94$.

of neutrons would be a broad $L_{90\%}$ distribution with a peak expected to be larger $L_{90\%}$. Figure 4.17 shows an example of $L_{90\%}$ distribution by the detector simulation with QGSJETII-04. Photons and neutrons having photon energies from 700 GeV to 800 GeV entering $\eta > 10.94$ are selected in Fig. 4.17. Photons and hadrons are clearly separated at $L_{90\%} \sim 20$. However, the separation of two components becomes worse for the high energy region. Therefore, the selection efficiency and purity of photons have to be determined for each energy bin. The true number of photons is able to be calculated by multiplying a factor, p/ϵ where p and ϵ represent purity and efficiency, respectively, to the measured number of photons in each energy bin. Although the selection efficiency can be determined by MC simulations, the purity depends on the photon-hadron ratio of the data.

Pure $L_{90\%}$ distributions of photons and hadrons are obtained by the detector simulation with QGSJETII-04, and they are called the photon and the neutron templates, respectively. Measured $L_{90\%}$ distributions at the each energy range are fit with the photon and the neutron templates. Two parameters to scale photon and neutron templates vertically are set as free parameters for the template fitting. Figures 4.18 and 4.19 demonstrate the result of the template fitting in several energy ranges. As shown in Fig. 4.18 and 4.19, template fitting is able to reproduce the measured $L_{90\%}$ distribution nicely in the wide energy range with these two parameters.

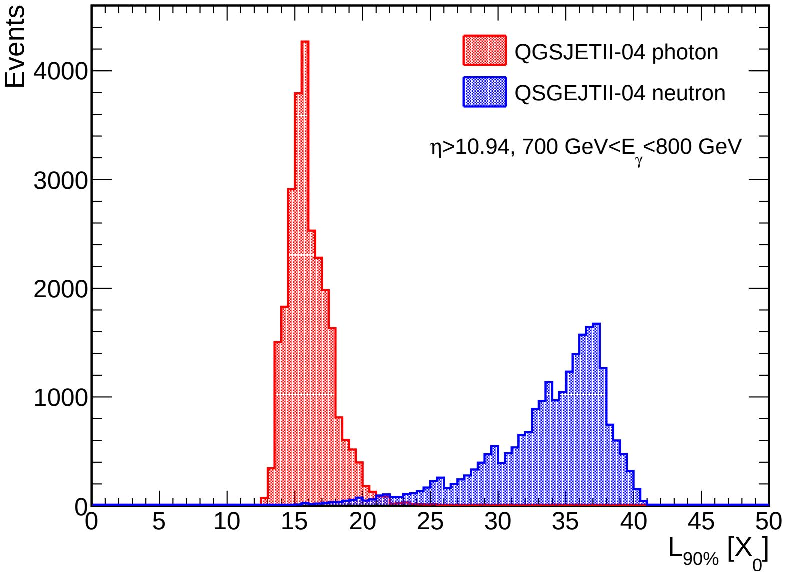

Figure 4.17: $L_{90\%}$ distributions of the pure photon (red) and neutron (blue) simulated with QGSJETII-04. Events having photon energies from 700 GeV to 800 GeV within $\eta > 10.94$ are selected.

After the fitting, purity and efficiency of the photon selection can be defined with a given cut for $L_{90\%}$. For the 13 TeV photon analysis, the $L_{90\%}$ values satisfying efficiency of 90 % are calculated for each energy region and are then fit with a logarithmic function. The calculated cut parameters and fitting results in both of the fiducial areas as a function of the energy are shown in Fig. 4.20. Contamination from the hadron component and missed photon events are corrected by applying p/ϵ. The PID correction has been performed by using p/ϵ as a function of shower energy, and the curves of the cut parameter can be found in Fig. 4.20. The factors are ranging within ±30% depending on the energy as shown in Fig. 4.21.

4.4 Spectrum correction

4.4.1 Multi-hit correction and spectrum unfolding

In order to obtain an unbiased photon spectrum free from distortion or smearing by the detector response, the unfolding technique is performed to the measured photon spectrum. Spectrum unfolding is a probabilistic approach, not deterministic, to obtain true spectrum from the observed spectrum. The technique is widely used in high energy physics to correct the instrumental distortion. Unfolding is particularly useful for the case where a reasonable hypothesized spectrum and backgrounds with free parameters to fit the observed data do not exist. In this study, the iterative Bayesian unfolding [58, 60] is performed to the measured spectrum via RooUnfold package [59].

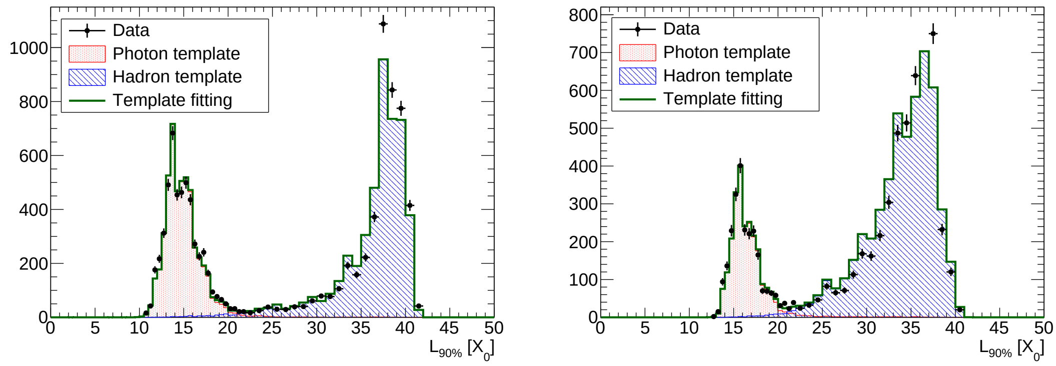

(a) 200–300 GeV (b) 900–1000GeV

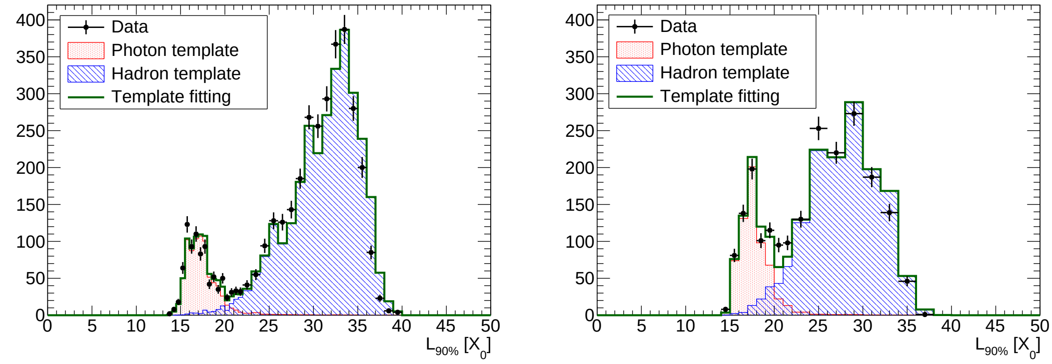

(c) 1900–2000 GeV (d) 2800–3000GeV

Figure 4.18: Measured $L_{90\%}$ distributions and template-fitting results in four energy ranges of the Arm1 20 mm calorimeter. Black points represent the measured data, while the green histograms are the results of the template fitting. Each of photon and hadron contribution is shown as filled the red and the blue areas, respectively.

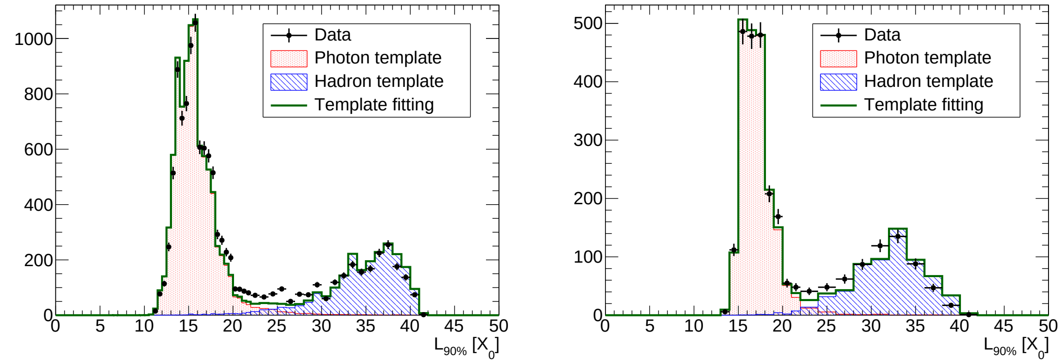

(a) 200–300 GeV (b) 900–1000GeV

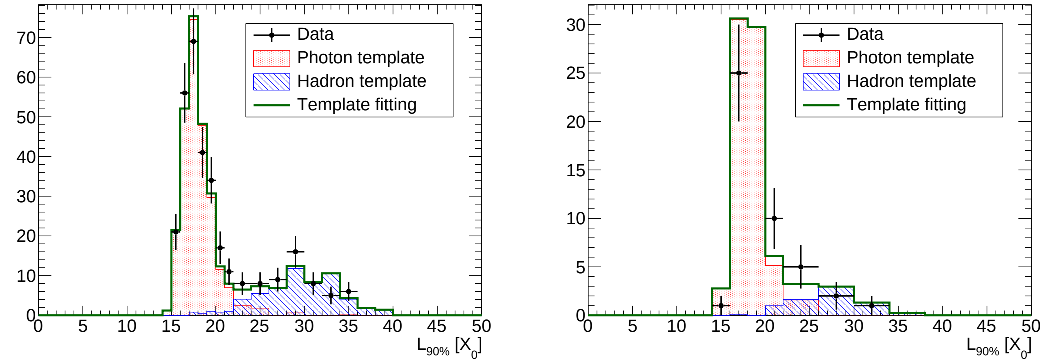

(c) 1900–2000 GeV (d) 2800–3000GeV

Figure 4.19: Measured $L_{90\%}$ distributions and template-fitting results in four energy ranges of the Arm1 40 mm calorimeter. Black points represent the measured data, while the green histograms are the results of the template fitting. Each of photon and hadron contribution is shown as filled the red and the blue areas, respectively.

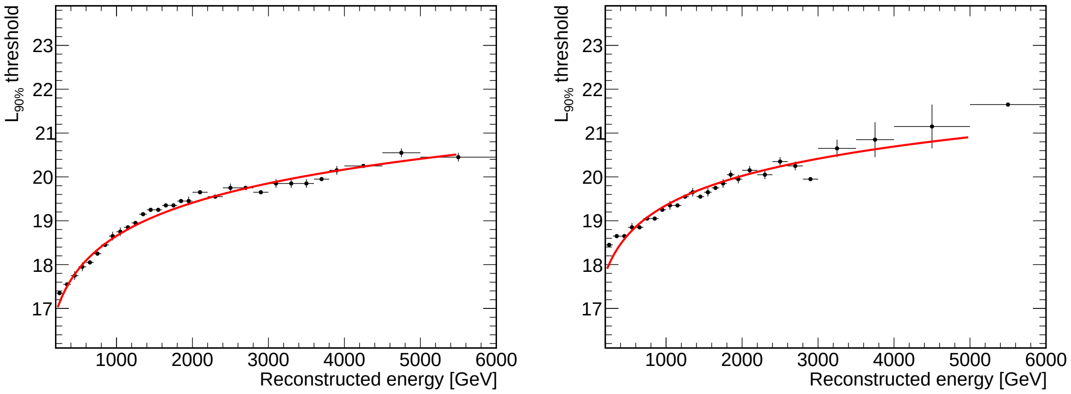

(a) Arm1 20 mm calorimeter (b) Arm1 40 mm calorimeter

Figure 4.20: $L_{90\%}$ cut parameters as a function of photon energy. The red curves show the results of fitting with a logarithmic function.

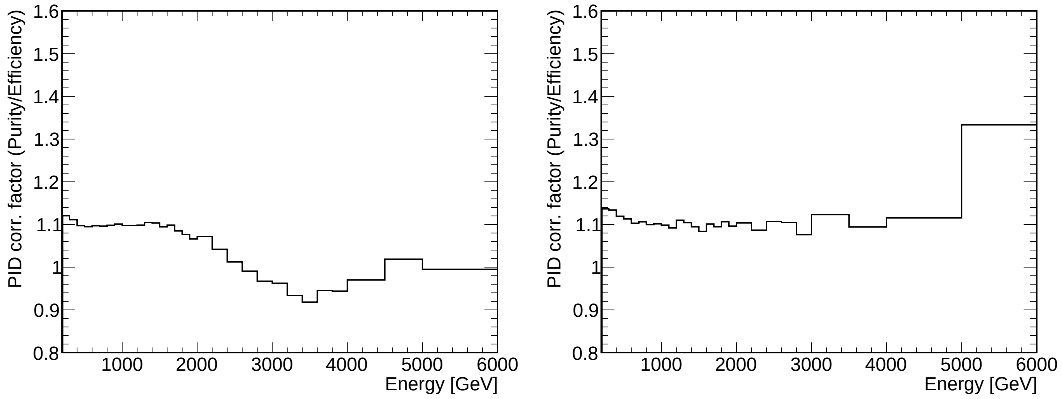

(a) 20 mm calorimeter

(b) 40 mm calorimeter

Figure 4.21: PID correction factors p/ϵ depending on the shower energies for the 20 mm and 40 mm calorimeters.

The spectrum unfolding is expressed using the Beyse theorem as

$$P(C|E,\Lambda) \propto P(E|C,\Lambda)P(C) \tag{4.2}$$

where C and E represent the true and measured spectra, respectively, and Λ denotes the response of the detector. Thus $P(C|E,\Lambda)$ denotes a conditional probability of C given E under Λ. However, there is a difficulty to express $P(C|E,\Lambda)$ mathematically [60]. In the iterative Bayesian unfolding, Eq.4.2 is altered as

$$P(C_i|E_j,\Lambda) \propto P(E_j|C_i,\Lambda)P(C_i) \tag{4.3}$$

where $P(E_j|C_i)$ is so-called 'response matrix'. C_i and E_j represent i-th and j-th bins of the true and measured spectra, respectively.

In order to obtain the *true* spectrum, the spectrum unfolding is performed by applying the unfolding matrix to the measured spectrum

$$N(C_i) = \sum_j \lambda_{ij} N(E_j) \tag{4.4}$$

where the unfolding matrix, λ_{ij} is given by

$$\lambda_{ij} = \frac{P(E_j|C_i)N_0(C_i)}{\epsilon_i f_j} \tag{4.5}$$

where $\epsilon_i \equiv \sum_j P(E_j|C_i)$ is considered as efficiencies and $N_0(C_i)$ is prior (or input) training spectrum, while f denotes the folded spectrum of a training sample. After the first iteration of the unfolding, $N_0(C_i)$ is replaced with $N(C_i)$ of the previous iteration. In principle, the input $flat$ spectrum is even possible, such as $P(C_i) = constant$. This may be rephrased that the result of the unfolding should not be influenced by the prior spectrum. However, such a $flat$ spectrum could lead a too much strong bias, even iteration smears the prior information. Thus a photon spectrum of an interaction model is used for the training for a practical reason.

As the training sample of the unfolding to calculate $\lambda_{i,j}$, inelastic collision events of 10^8 are generated with use of QGSJETII-04 including the transportation of particles in the beam pipe and the detector simulation. Looping all the training events, each event is classified into three types of the event (*True*, *Missed*, and *Fake*) using the true and reconstructed information. If the event is single photon according to the true information and is detected by the detector consistent with true information such as the number of hits and the incident position, the reconstructed and true energies of the incident particle are used for the calculation of the response matrix, $P(E_j|C_i)$. These events are classified as *True*. Otherwise, if the event is multi-hit according to the true information or the reconstruction fails, those events are considered as as *Missed* due to inefficiency. The point here is that contribution of the multi-hit events, which are cut in the reconstruction process, are taken into account as inefficiency of the corresponding bins of photons in C_i. Therefore, the correction of the multi-hit events depends on the interaction model selected for the training. Finally, in the cases where the photon-like particle is reconstructed with no true information, these events are treated as *Fake* in the unfolding matrix.

The contribution of each type of the event is shown in Fig. 4.22 with the reconstructed single photon spectra of the training sample. The fraction of *Missed* increase in the high energy region due to the multi-hit events.

Beside QGSJETII-04, the simulation of EPOS-LHC with 3×10^7 inelastic collisions is performed to evaluate the systematic uncertainty concerning the choice of the model. The uncertainty of the unfolding matrix is determined by the statistics of the training samples and the number of iteration. Basically the uncertainty of the unfolding increase as the number of iteration increases. RooUnfold is able to treat the propagation of the errors during the iteration, even though it is not considered and hence underestimated in the original paper [58]. The number of iteration for the photon analysis stops at three, because, not only the large errors, further iteration causes unphysical behavior of the unfolded spectra such as bin-by-bin spikes instead of smooth spectral shapes.

Figure 4.23 shows the ratio of the photon spectra before and after the unfolding. The obtained photon spectra are unfolded by the unfolding matrix trained by QGSJETII-04. Note that the unfolding includes the multi-hit correction, while it is essentially independent of bin-to-bin migration of the unfolding, owing to the diagonal correction factors in the correction matrix. After the unfolding, the contents of each bin changes roughly -20% and -30% for the large part of the spectra of $\eta > 10.94$ and $8.99 > \eta > 8.81$, respectively, while large differences are seen between the measured and the unfolded spectra at the highest energy bins.

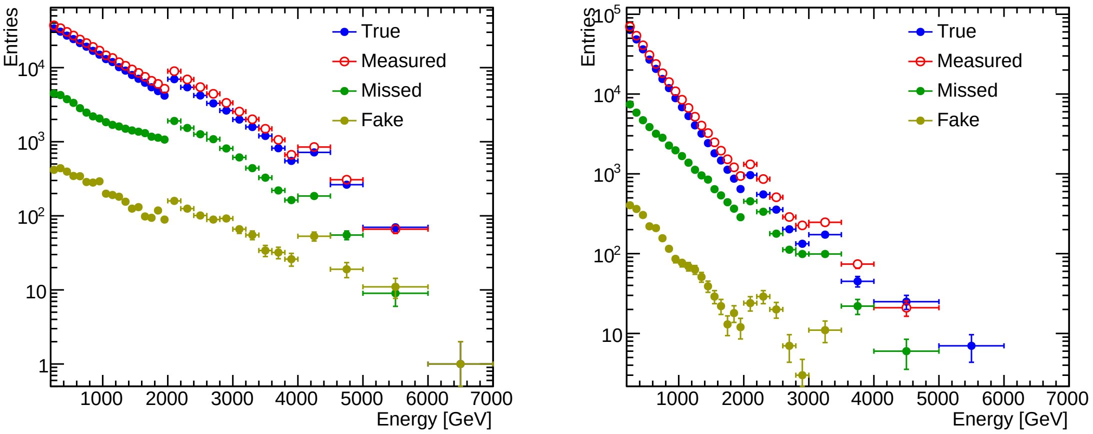

Figure 4.22: Contribution of three types (*True*, *Missed*, and *Fake*) of the events and the measured spectra (indicated in *Measured*) at $\eta > 10.94$ (left) and $8.99 > \eta > 8.81$ (right) of the training sample. Horizontal axis represents the true energy for *True* and *Missed*, and the reconstructed energy for *Fake* and *Measured*.

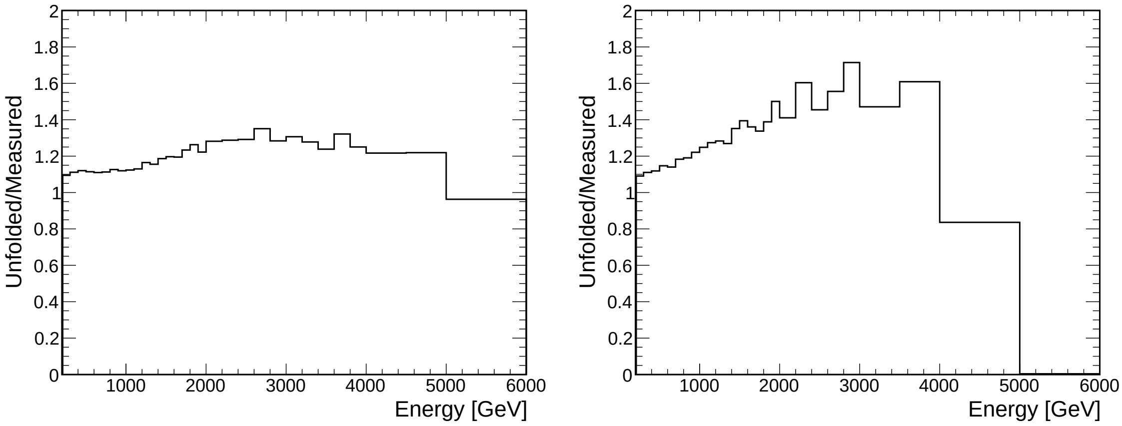

(a) $\eta > 10.94$

(b) $8.99 > \eta > 8.81$

Figure 4.23: Comparison of the photon spectra before and after the unfolding at a) $\eta > 10.94$ and b) $8.99 > \eta > 8.81$.

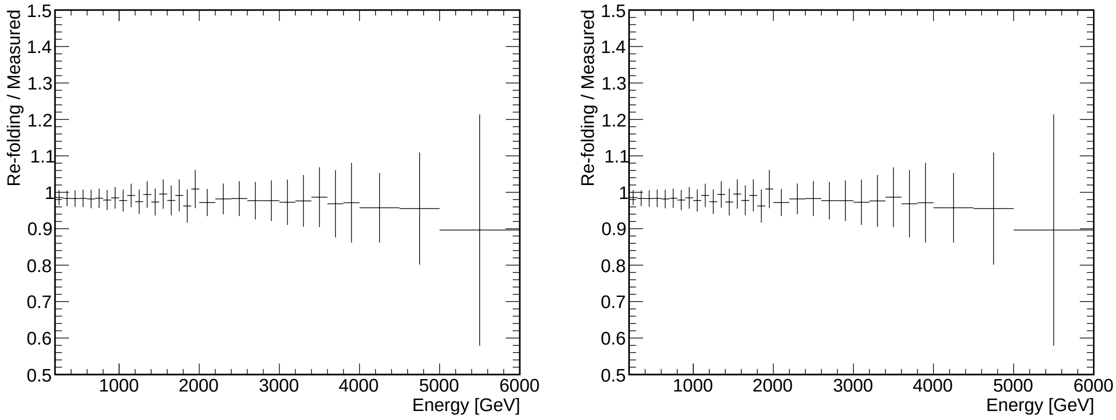

(a) $\eta > 10.94$

(b) $8.99 > \eta > 8.81$

Figure 4.24: Ratio of the re-folding spectra to the measured spectra at a) $\eta > 10.94$ and b) $8.99 > \eta > 8.81$.

In order to validate the unfolding process, the unfolded spectra are re-foleded again with use of the calculated response functions for each η regions. Figure 4.24 shows the ratio of the re-folded spectra to the measured spectra for both η regions. The re-folding process succeed to reproduce the original measured spectra within the errors, thus we conclude that there is no significant systematic bias in the unfolding process.

4.4.2 Beam-pipe and beam-gas backgrounds

The measured photon spectra could be contaminated with the secondaries originated from beam related backgrounds. Main contribution are considered as the beam gas and the beam pipe backgrounds.

The background contribution of beam gas events is estimated by using a special bunch structure, named “Non-colliding bunches”, in the bunches circulating the LHC, in which only one side of beam bunch exists, thus no collisions are expected. Therefore, the triggered events synchronized with non-colliding bunches are caused by the interactions of beam particles with the residual gas in the pipe or with the beam pipe material. The spectral shape of beam gas events is quite similar to that of collision events, and the yield is proportional to the intensity of the beams. The contribution of beam gas events to the photon spectra is less than 1 % and corrected in the spectrum calculation.

Secondary particles can interact with the beam pipe and generate particles which are not associated with the p–p collisions. Even a thickness of the beam pipe itself is negligible, particles scattered with the small angle have to experience long beam-pipe materials while their propagation. Accordingly, particles generated in the beam pipe

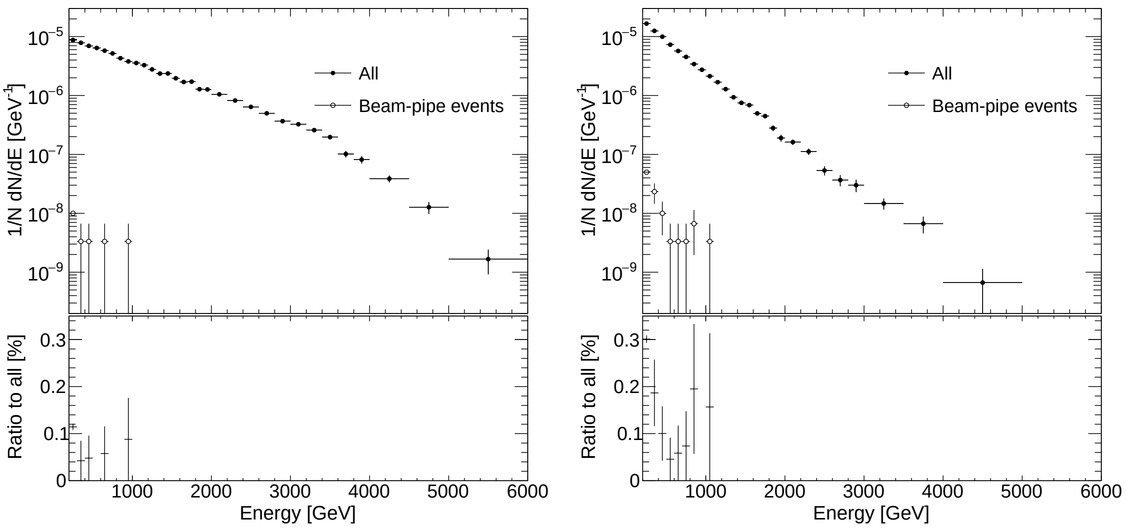

(a) $\eta > 10.94$

(b) $8.99 > \eta > 8.81$

Figure 4.25: The photon spectra with QGSJETII-04 and the contribution from the beam pipe events. Black and white markers are spectra of all and beam-pipe-event origin, respectively. The fraction of beam pipe events to all events are shown in the bottom for each.

could enter the LHCf detectors. These beam pipe background events are thought to be low energy considering their larger production angle. Beam pipe backgrounds is studied by the MC simulation which calculates the transportation of the particles from the interaction point to the detector position. Contribution of the beam pipe background is then estimated by using the tag of each particles, such as the nominal beam-beam collision or the secondary interaction with the beam pipe meterial. QGSJETII-04 is used for this study. Figure 4.25 shows the photon spectra together with the photon spectra of which photons are originated from the beam pipe events. As expected, the energies of photons originated from the beam pipe events are concentrated on the low energy regions below 1000 GeV, and their yield is much smaller than that of beam-beam collision events. The fractions of beam pipe events are less than 0.3% for both of $\eta > 10.94$ and $8.99 > \eta > 8.81$. We do not subtract these events because its fraction is enough small compared to the other systematic uncertainties.

4.5 Systematic uncertainties

4.5.1 Beam center

Pseudorapidty of the paticles are calculated based on the beam center determined in Sec. 4.3.3. Since there are the η dependence of the sectral shape and the yield, the uncertainty on the beam center could change the spectrum calculated for each

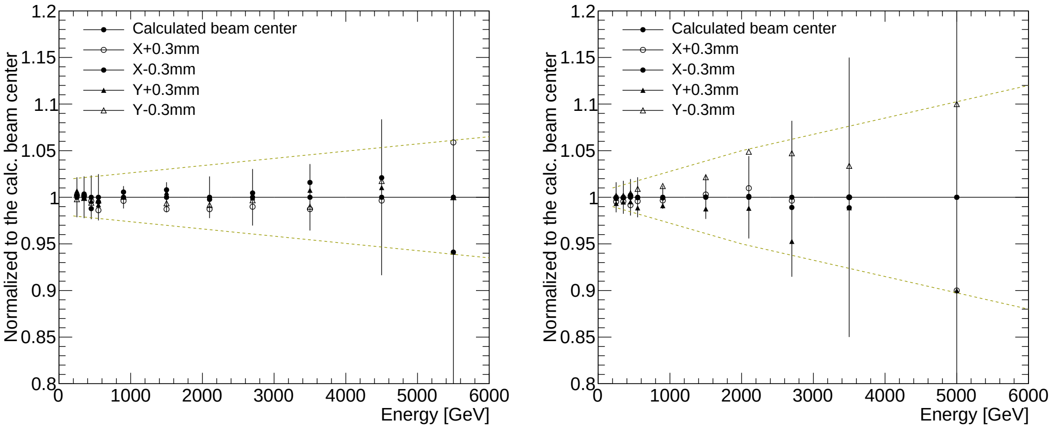

(a) $\eta > 10.94$ (b) $8.99 > \eta > 8.81$

Figure 4.26: The ratio of the four additional energy spectra for shifted beam center positions to the original spectrum in the η regions of a) $\eta > 10.94$ and b) $8.99 > \eta > 8.81$. Error bars are common for the ratios of all the four spectra, and are shown for one spectrum.

η region. The uncertainty concerning beam center is estimated from comparison of the spectra calculated with the fiducial areas shifted by ±0.3 mm in the x and y directinos. In Fig. 4.26, four of the spectra are shown for the four shifted fiducial areas normalized to the original spectrum. Here the uncertainty of beam center calculation is assigned to be 0.3 mm discussed in Sec. 4.3.3. The upper and lower band of the systematic uncertainties are defined to cover all the center values of the minimum and the maximum for all energy bins. Eventually, systematic errors for the spectra are estimated to be 2 % and 1 % for $\eta >$10.94 and $8.99 > \eta > 8.81$ at 200 GeV, respectively. They increase to 6.5 % and 12 % for the $\eta >$10.94 and $8.99 > \eta > 8.81$ at 6000 GeV, respectively.

4.5.2 PID correction

The uncertainty of the PID correction is estimated by checking the bias of the analysis criteria. In Sec. 4.3.4, the cut parameter which satisfies the photon selection efficiency of 90 % are applied to measured $L_{90\%}$ in each energy range. Photon spectra are again calculated with different criteria, 85 % and 95 % instead of 90 %, although the difference of cut criteria here is independent of the result if the correction for compensation of missed photon and the hadron contamination works correctly. The contribution of missed photons and contaminated neutrons in the photon spectra with cut parameters of 85 % and 95 % are corrected using the correction functions optimized for each as well as in the case of 90 %.

Cut parameter dependence of the calculated photon spectrum is shown in Fig. 4.27.

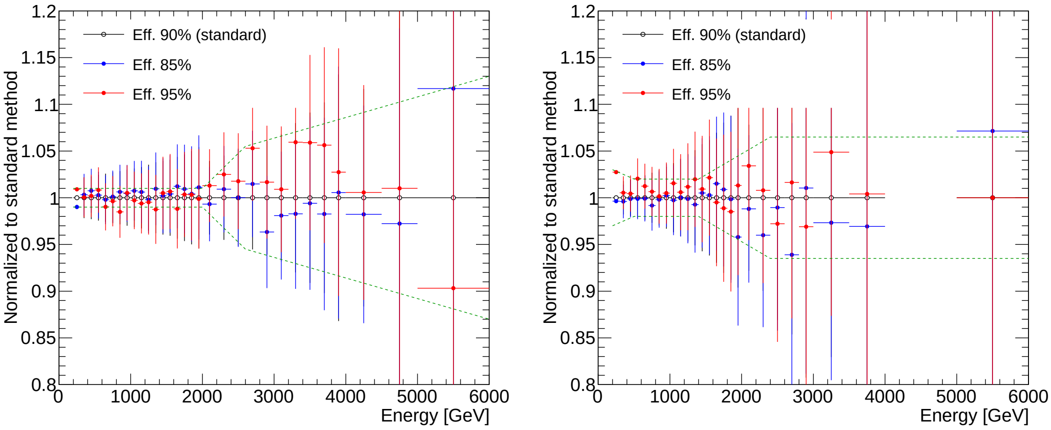

(a) $\eta > 10.94$ (b) $8.99 > \eta > 8.81$

Figure 4.27: The three photon spectra calculated with the different criteria for the PID correction having efficiencies of 85 %, 90 %, and 95 % in a) $10.94 > \eta$ and b) $8.99 > \eta > 8.81$. Here shown the ratios normalized to the one with 90 % efficiency which is the standard criteria.

Two spectra with the cut parameter of 85 % and 95 % are normalized to the original spectrum with the parameter of 90 %. The effect is a level of few percent in the lower energy region, while it increases to around 10%.

4.5.3 Multi-hit selection

The uncertainty from the multi-hit selection performance is estimated by the difference of the multi-hit detection performance of data and MC. The difference of the performance is already shown in Fig. 4.12. The ratio of the reconstructed events of the multi-hit to the single-hit is also taken into account. The ratios of two η regions calculated by the measured data are shown in Fig. 4.28. Although the fraction of the multi-hit events is small below 2000 GeV, it increases as the energy for each η region.

The systematic uncertainty of the multi-hit selection is estimated by the results in Fig. 4.12 multiplying the multi-hit event fraction based on the results in Fig. 4.28. The obtained results are shown in Fig. 4.29. The uncertainty is almost negligible in low energy because the fraction of the multi-hit event is small, while the uncertainty increases to a level of 4 % and 8 % for $\eta > 10.94$ and $8.99 > \eta > 8.81$, respectively, in the high energy region.

4.5.4 Unfolding and multi-hit correction

As is discussed in Sec. 4.4.1, spectrum unfolding includes uncertainties of unfolding process itself and the multi-hit correction. The uncertainty of unfolding is a level of few percent relying on the statistics of the training sample and the number of inter-

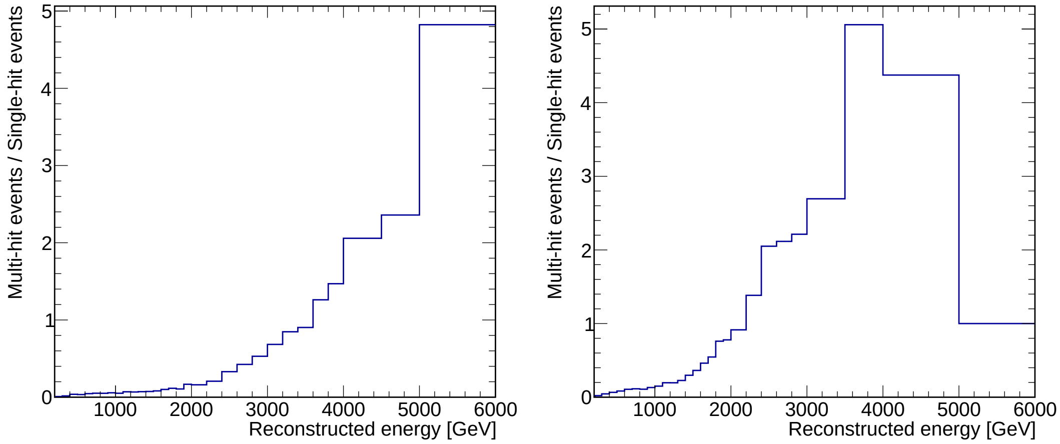

(a) $\eta > 10.94$ (b) $8.99 > \eta > 8.81$

Figure 4.28: The ratios of the reconstructed events of the multi-hits to the single-hit of for a) $\eta > 10.94$ and b) $8.99 > \eta > 8.81$. The ratios here are calculated from the measured data in the photon dataset. Horizontal axis denotes the energy reconstructed as a single photon.

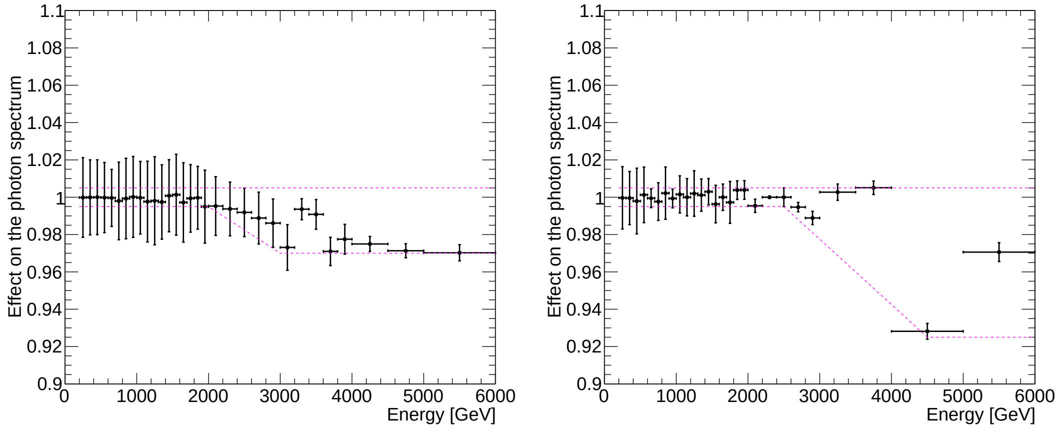

(a) (b)

Figure 4.29: The uncertainty on the multi-hit selection performace of two rapidity regions for the Arm1 a) 20 mm and b) 40 mm calorimeters.

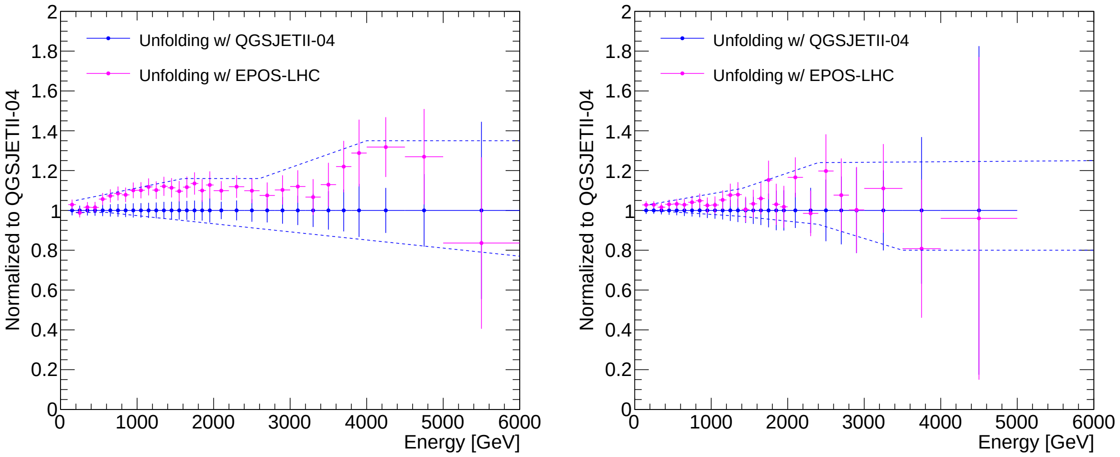

(a) $\eta > 10.94$

(b) $8.99 > \eta > 8.81$

Figure 4.30: The ratios of the unfolded measured spectra with the training samples of QSGJETII-04 (blue) and EPOS-LHC (magenta) normalized to that of QSGJETII-04 for a) $\eta > 10.94$ and b) $8.99 > \eta > 8.81$. The difference between two unfolded spectra indicates the model dependence of the distribution of secondary particles concerning the multi-hit events.

action. Total uncertainty is dominated by contribution of the multi-hit correction. Multi-hit correction performed in Sec. 4.4.1 completely depends on the secondary particle distribution of the selected interaction model. QGSJETII-04 is selected as the reference model in this study.

The uncertainty of the multi-hit correction is estimated from the two unfolded spectra with different training samples. EPOS-LHC is used as an alternative model and simulated for 3×10^7 collisions. Figure 4.30 shows the unfolded spectra with two models normalized to that for QGSJETII-04. According to Fig. 4.30, EPOS-LHC predicts that the observed photon spectra are much biased with the multi-hit events for both η regions than those predicted by QGSJETII-04. The uncertainty is estimated to include the center values of the minimum and the maximum of all bins asymmetrically, less than ±20% below 2000 GeV and ±20% at the higher energy regions.

4.5.5 The energy scale

Systematic effect of spectrum calculation arising from the energy scale is estimated by taking the ratio of the original spectrum to the spectra with shifted energy scale. The reasonable shift of the energy scale is estimated from the contribution of linearity of ADC (0.1%), pedestal fluctuation (0.025%), the gain calibration (2.2%), cable attenuations (0.5%), HV gain of PMTs (1.3%), gain table (1.4%), nonuniformity of the energy reconstruction (1.3%), temperature dependence of the PMTs (0.1%), and the

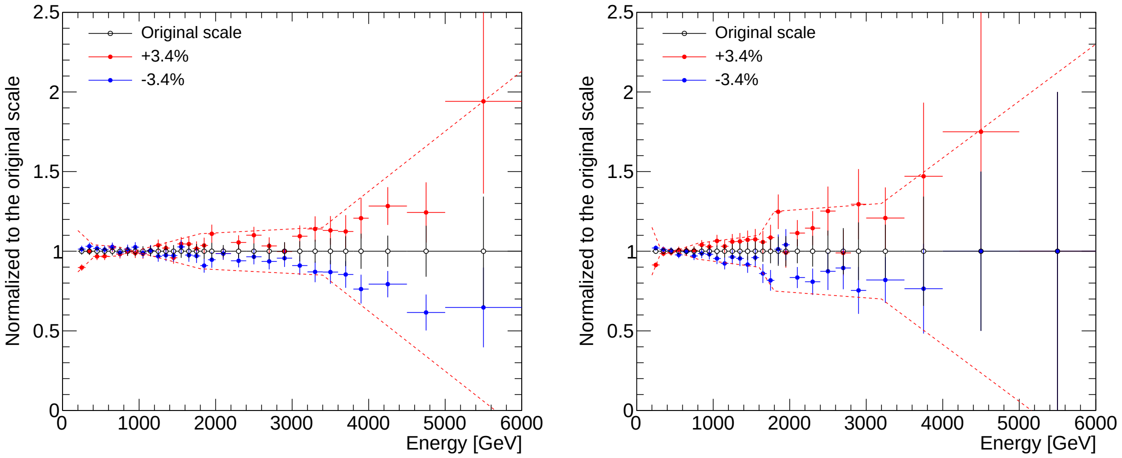

(a) $\eta > 10.94$

(b) $8.99 > \eta > 8.81$

Figure 4.31: Systematic effect arising from uncertainty of the energy scale in a) $\eta > 10.94$ and b) $8.99 > \eta > 8.81$. Three spectra shown in each plot are those of the original (white), energy scale shifts of -3.4%(blue) and +3.4% (red), respectively. Estimated systematics are shown in red broken lines.

LPM effect (0.7%). Total of 3.4% is obtained by adding each element quadratically. Figure 4.31 shows the ratio of the measured spectra to the spectra with the shifted energy scale. Approximately 10 % of the uncertainty is observed around 2000 GeV, and the effect is larger in the higher energy region.

Stability of the energy scale during the runs for the photon analysis is evaluated by using the time variation of the reconstructed π^0 mass peaks every in 5 LHCf runs as shown in Fig.4.32. Less than ±1 % of variation is seen and it is negligible comparing to the other contribution of the systematic uncertainties.

4.5.6 Overall

All contribution of the systematic uncertainties of the Arm1 detector is summarized in Fig. 4.33. The largest contribution is the energy scale, while it becomes compatible with the uncertainty arising from the multi-hit correction in upper side of the lower energy regions. The total systematic error is calculated by adding each component quadratically, and it becomes larger as energy increases. At the highest energy bin, the contribution from the energy scale dominates the others.

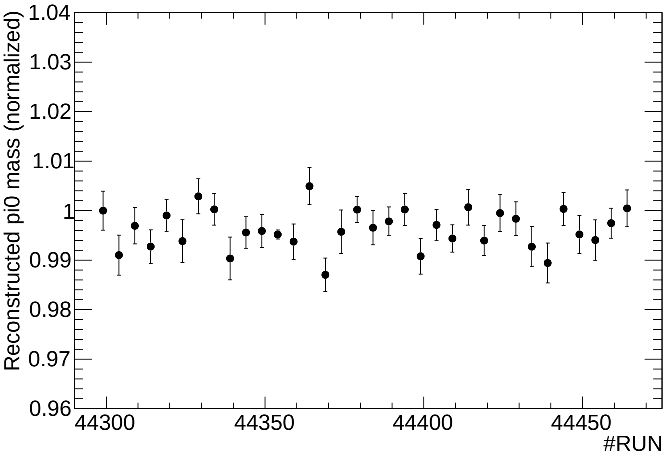

Figure 4.32: Time vatiation of the measured π^0 mass peaks reconstructed by photon pairs. The horizontal range shown in the plot correspond to the LHCf runs used in this photon analysis.

4.6 Forward photon spectra and comparison with MC predictions

4.6.1 Combining the photon spectra

Before comparing the unfolded photon spectra with the MC predictions, we combine the Arm1 spectra with those of Arm2 which are analyzed independently. By comparing both of the spectra, they show good agreement within the estimated systematic errors as shown in Fig. 4.34. The difference of the two spectra is 10% level at maximum except for very-high energy region. We combine those of spectra taking into account the associated systematic uncertainties and their correlations. We follow the spectrum-combine method studied in the previous works [39]. The Arm1 and Arm2 spectra have been combined following the "pull-method"[61] and the combined spectra have been accordingly obtained by minimizing the value of the chi-square function defined as

$$\chi^2 = \sum_{i=1}^{n} \sum_{a=1}^{2} \left(\frac{N_{a,i}^{measured}(1 + S_{a,i}) - N_i^{combine}}{\sigma_{a,i}} \right)^2 + \chi^2_{penalty} \tag{4.6}$$

where the index i represents the energy bin number running from 1 to the total number of bins, n, $N_{a,i}^{measured}$ and $N_i^{combined}$ are the number of events of measured and combined spectra, respectively, and $\sigma_{a,i}$ is the uncertainty of the Arm-a spectra calculated by quadratically adding the statistical uncertainties. The $S_{a,i}$ denotes the

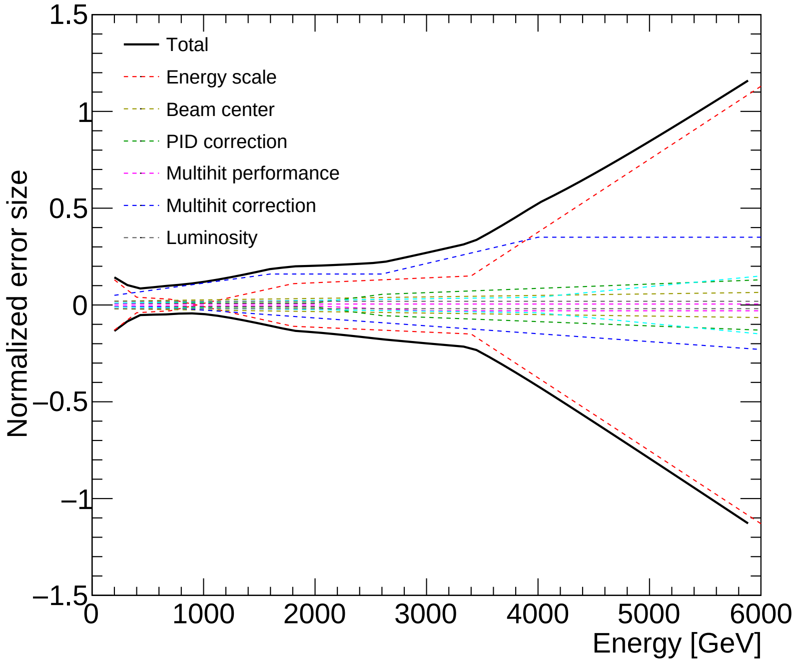

(a) $\eta > 10.94$

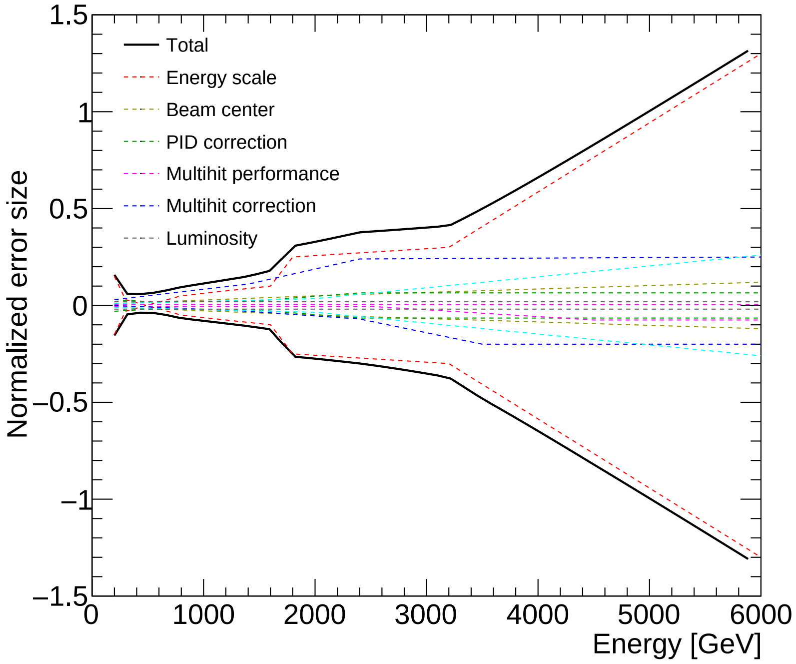

(b) $8.99 > \eta > 8.81$

Figure 4.33: All contribution of the systematic uncertainties and the sum of them for the Arm1 detector at a) $\eta > 10.94$ and b) $8.99 > \eta > 8.81$.

systematic correction to the number of events in the ith bin of Arm-a,

$$S_{a,i} = \sum_{j=1}^{4} f_{a,i}^{j} \epsilon_{a}^{j}. \tag{4.7}$$

The coefficient $f_{a,i}^{j}$ is the systematic shift of the i-th bin content due to the j-th systematic uncertainty term. The four systematic uncertainties for *energy scale*, *PID correction*, *beam center*, *multi-hit selection* are assumed fully uncorrelated between the Arm1 and Arm2 detectors. Arm1-Arm2 correlated uncertainties, multi-hit correction and luminosity are quadratically added to the combined spectra. Coefficients ϵ_{a}^{j}, which should follow a Gaussian distribution, can be varied to achieve the minimum χ^2 value in each chi-square test, while they are constrained by the penalty term

$$\chi^2_{penalty} = \sum_{j=1}^{4} \sum_{a=1}^{2} |\epsilon_{a}^{j}|^2 \tag{4.8}$$

The ratio of Arm1 and Arm2 to the combined spectra are shown in Fig. 4.35. The obtained minimum chi-squares over degree of freedom are 1.61 and 1.65, and corresponding probabilities are 0.03 and 0.04 for $\eta > 10.94$ and $8.99 > \eta > 8.81$, respectively. There is a systematic difference between Arm1 and Arm2 in $\eta > 10.94$ below 4000 GeV, but still, they are consistent within the estimated uncertainty. It is expected to be originated from the one or some of the systematic effect.

4.6.2 Comparison with the predictions of the hadronic interaction models

Figure 4.36 shows the obtained inclusive photon energy spectra at $\eta > 10.94$ and $8.99 > \eta > 8.81$ and the corresponding model predictions. Predictions of each model have been generated with use of Cosmic Ray Monte Carlo package (CRMC) [62]. In this study, QGSJETII-04 [25], EPOS-LHC [24], SIBYLL2.3 [32], DPMJET3.06 [27], and PYTHIA8.212 [28] are compared to the LHCf results. 10^8 inelastic collisions are generated for each interaction model. Statistic errors of MC predictions are enough smaller than the systematic uncertainty of the measured results.

In $\eta > 10.94$, the prediction of DPMJET3.06 and SIBYLL2.3 are overestimation and underestimation, respectively, and they are clearly inconsistent with the experimental result, Especially, the spectral shape predicted by DPMJET3.06 is too much hard above the mid-energy region. A similar spectral shape is seen also for PYTHIA8.212, while its photon yield shows good agreement, better than 20%, below 3000 GeV. A particular increase of photon yield of PYTHIA8.212 above 3000 GeV is associated with the diffractive events of which fraction exceeds the other contribution unlike the other models [63]. Although we do not separate the diffractive and the

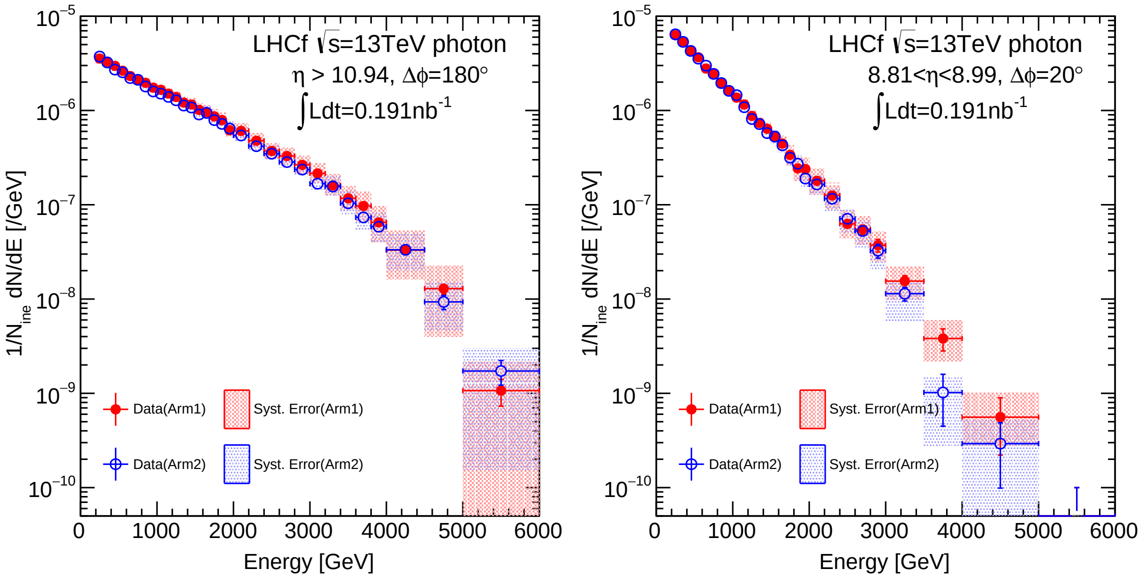

Figure 4.34: Comparison of the Arm1 and the Arm2 spectra in $\eta > 10.94$ with $\Delta\phi = 180°$ (left) and $8.99 > \eta > 8.81$ with $\Delta\phi = 20°$ (right). The red and the bule hatched boxes show systematic errors for Arm1 and Arm2, respectively.

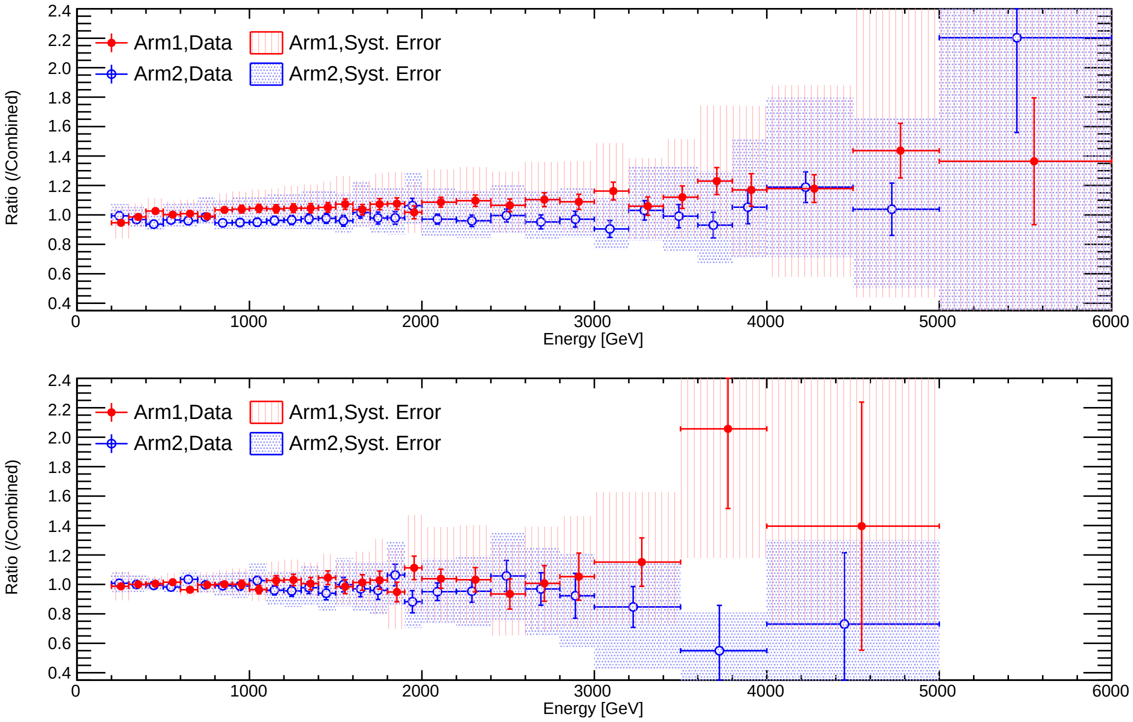

Figure 4.35: The Arm1 and the Arm2 spectra normalized to the combined results. Top and bottom plots are $\eta > 10.94$ and $8.99 > \eta > 8.81$, respectively. Red and blue denote Arm1 and Arm1, respectively. Systematic uncertainties of each detector are shown by the red and the blue hatched boxes.

non-diffractive events in this work, a future analysis with the ATLAS collaboration has a capability of extracting diffractive events. LHCf can use the ATLAS detector as a *veto* detector to tag diffractive events because LHCf had performed a common operation during Fill 3855 with ATLAS. More details can be found in the simulation study in [63]. QGSJETII-04 and EPOS-LHC show quite similar behavior, consistent with the measured result within 30%, up to 4000 GeV, whereas very high energy photons are expected by EPOS-LHC at the highest energy bin.

In $8.99 > \eta > 8.81$, The results indicate that all models except QGSJETII-04 predict photon spectrum at this region harder, especially those of DPMJET 3.06, SIBYLL2.3, and PYTHIA 8.212. Although the spectral shape of EPOS-LHC is harder than the measured result above roughly 3000 GeV, the agreement with the measured result is the best, better than 20%, below 3000 GeV. The prediction of QGSJETII-04 at this region is smaller than the data as well as $8.99 > \eta > 8.81$, or even worse, almost half of the data.

General features of the model predictions comparing to the LHCf results are similar to those of $\sqrt{s} = 7$ TeV previously shown in Fig. 1.10. According to the obtained results, we confirm that even the post-LHC models, QGSJETII-04, EPOS-LHC, and SIBYLL2.3, do not reproduce the LHCf spectra perfectly. Considering that the very-forward region, $\eta > 8.4$, is very relevant to in the air shower development as we discussed in Sec. 1.3.1, the study here indicates the importance of the further tuning of the post-LHC models with the LHCf results.

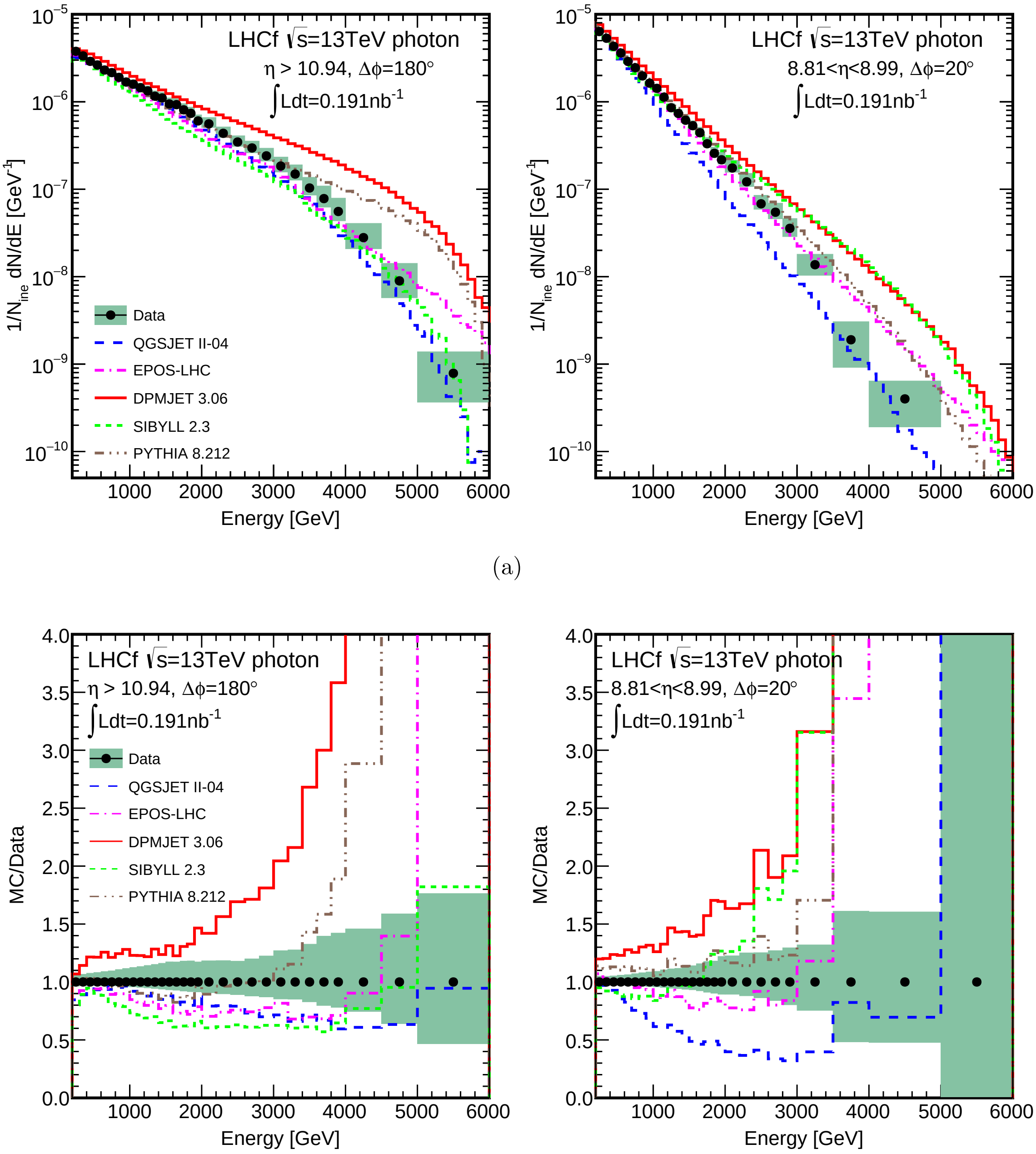

(a)

(b)

Figure 4.36: Forward photon spectra and comparison with the model predictions in $\eta > 10.94$ with $\Delta\phi = 180°$ and $8.99 > \eta > 8.81$ with $\Delta\phi = 20°$. Top and bottom plots represent a) energy spectra of the observed results and MC predictions and b) ratios of MC predictions to the observed results, respectively. Black points and colored lines represent the combined LHCf results and model predictions, respectively. Green area associated with the data points denotes the systematic uncertainty. Statistical errors of model predictions are considerably small against the systematic uncertainty of data results.

Chapter 5

Pseudorapidity dependence of the photon energy flow in $\sqrt{s}$ =13 TeV collisions

5.1 Energy flow measurement with the Arm1 detector

In Chap. 4, the inclusive photon spectra at $\eta > 10.94$ and $8.99 > \eta > 8.81$ are calculated with the Arm1 and the Arm2 detectors, and the model predictions are tested in terms of the spectral shape. In this chapter, we focus on the photon energy flow which is relevant to the EM component of the air shower. The photon energy flows are calculated by the photon energy spectra at each η region. In order to test the η-dependence of the photon energy flow with wide η, the η acceptance region is enlarged with the Arm1 detector.

5.1.1 Additional pseudorapidity regions of 13 TeV photon analysis

The additional η regions, 9.22> η >8.99, 8.81> η >8.66 and 8.66> η >8.52, are selected with keeping the distance of 2 mm from the edge of the 40 mm calorimeter of Arm1. Eventually, 8.66> η >8.52 as the lowest η region reaches almost the limit of the acceptance of LHCf in the p–p $\sqrt{s}$ = 13 TeV dataset. Figure 5.1 shows the distribution of the reconstructed positions for the photon events in the four η regions of the 40 mm calorimeter and the region of the 20 mm calorimeter used in this study. The polar angle cut $\Delta\phi$ =20° is applied for the additional regions in the 40 mm calorimeter as well as 8.99> η >8.81.

The difference among various model predictions of the photon production is shown in Fig.5.2. Each bin content represents the number of photon events normalized

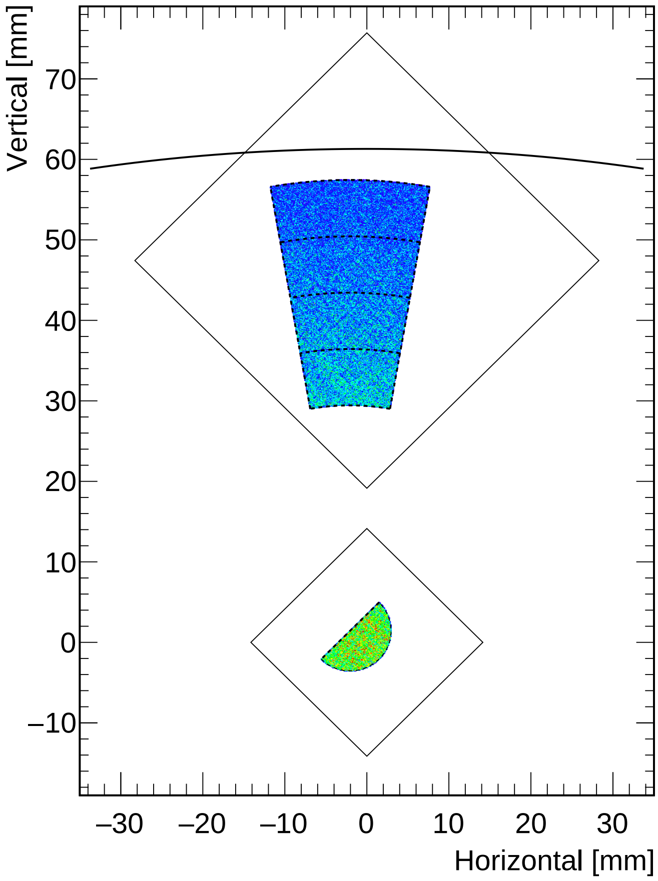

Figure 5.1: All the η regions for the energy flow analysis including additional regions. Four η regions in the 40 mm calorimeter have boundaries at the distance from the beam center of 28.0 mm, 35.0 mm, 42.0 mm, 49.0 mm, and 56.0 mm, respectively, with $\Delta\phi$ =20°. The arc of an ellipse shown on the upper side of the 40 mm calorimeter is the projection of the beam pipe, thus the limitation of the acceptance, at approximately η=8.4.

by the number of inelastic collisions in p–p $\sqrt{s}$ =13 TeV collisions in the x_F and p_T phase space, where x_F and p_T represent Feynman-x and transverse momentum, respectively. The post-LHC models, QGSJETII-04, EPOS-LHC, and SIBYLL2.3 are simulated with 10^8 inelastic collisions. Five pseudorapidity regions which are able to be tested in this study are indicated by the broken lines. EPOS-LHC and SIBYLL2.3 predict high energy photons in high η, and only EPOS-LHC has very high energy photons in the region of $x_F > 0.9$ under the given number of collisions. SIBYLL2.3 implies the existence of high energy photons even in high p_T up to approximately 3 GeV unlike the other two models. In contrast to EPOS-LHC and SIBYLL2.3, the photon production predicted by QGSJETII-04 is modest in high x_F. Owing to the additional η regions, the model predictions can be tested with measured data in the phase space where large differences can be observed among the models.

5.1.2 Spectrum calculations for the additional η regions

The inclusive photon energy spectra at each additional pseudorapidity region are calculated by the analysis procedure described in Chap. 4. Systematic uncertainties are again evaluated for those additional η regions. Eventually, no significant differences of the level of the uncertainties are observed between the region $8.99 > \eta > 8.81$ and the additional η regions. Thus same values of the systematic uncertainties as well as $8.99 > \eta > 8.81$, as shown in Fig. 4.33, are taken for the additional η regions. More detail discussions can be found in Appendix B.

Figure 5.3 shows the unfolded photon spectra and the model predictions at the four η regions in $9.22 > \eta > 8.52$. Corresponding ratio plots can be found in Fig. 5.4. QGSJETII-04 predicts the lowest photon yields, less than a half of that of the measured data in the high energy region for all η regions as shown in Fig. 5.3 and 5.4. SIBYLL2.3 shows good agreement with data below a few TeVs, but the predicted photon spectra are clearly harder than that of data in the TeV region. This trend is true for all four η regions in Fig. 5.4. Although the spectral shape of EPOS-LHC is softer than that of data in the mid-energy region, its photon yield is close to the data within a level of 30 % in the wide range except for the highest energy bins. More importantly, the agreement of EPOS-LHC with the observed result is remarkably good, and almost compatible within the systematic errors, below 1000 GeV. The trends of the differences between the model predictions and the observed results are similar to those observed in $8.99 > \eta > 8.81$ as discussed in Chap. 4 for the Arm1-Arm2 combined result. The agreement in the low energy region is essentially important from the point view of the energy flow because the contribution from the low energy is expected to be dominant considering the exponential-like spectral shape.

Regarding the differences between the pre/post-LHC models, the predictions of the photon yield of EPOS-LHC and QSGJETII-04 below 1000 GeV become smaller than those of EPOS1.99 and QGSJETII-03, respectively. Especially, the agreement of

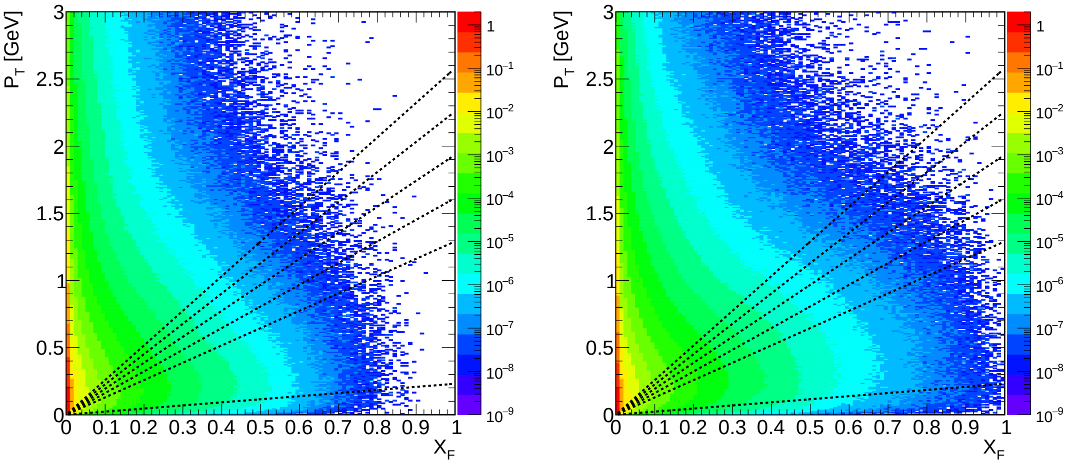

(a) QGSJETII-04 (b) EPOS-LHC

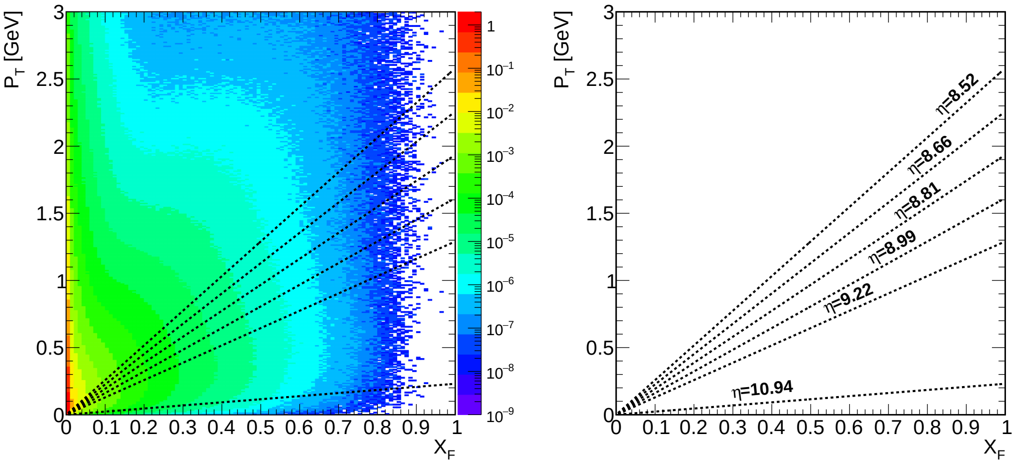

(c) SIBYLL2.3 (d) η correspondence

Figure 5.2: Production rate of photons of a) QGSJETII-04, b) EPOS-LHC, and c) SIBYLL2.3 in p–p 13 TeV collisions. Horizontal and vertical axises represent Feynman-x and the transverse momentum, respectively. The number of contents in each bin represents the number of produced photons normalized by the number of inelastic collisions. Each broken lines on the plots shows the acceptance regions of the study, which are η >10.94, 9.22> η >8.99, 8.99> η >8.81, 8.81> η >8.66, and 8.66> η >8.52 as illustrated in the panel (d).

EPOS with data improves for all four η regions shown in Fig. 5.4. This is not true for SIBYLL. SIBYLL2.3 increases photon yield at the low energy region in 9.22> η >8.99, while no significant difference can be observed in low energy for other three regions. SIBYLL2.1 exceeds the photon yields of SIBYLL2.3 in the mid-energy regions for all η regions.

Figure 5.5 shows the η dependence of the spectral shape at $9.22 > \eta > 8.52$. Each spectrum is normalized to the one at $9.22 > \eta > 8.99$. As is expected, softer spectra are observed as η decreases as shown in Fig. 5.5(a). The measured data has a large η dependence of the spectral shape than any other model predictions, even though similar η dependence can be observed in QGSJETII-04 (Fig. 5.5(b)) and EPOS-LHC (Fig. 5.5(c)). SIBYLL2.3 has a particular feature, which is the weakest η dependence above 2000 GeV, among three of the model predictions as shown in Fig. 5.5(d). The behavior of SIBYLL2.3 at high x_F and high transverse momentum already appears in Fig. 5.2, but the experimental data disfavors the trend clearly.

5.1.3 Energy flow calculation

Forward photon energy flow of the i-th bin, Y_i [GeV/$\Delta\eta$], is calculated by the integration of the photon spectrum measured in the certain η range, $\Delta\eta$. Y_i is given by

$$Y_i = \frac{1}{\Delta\eta} \sum_j E_j \, F(E_j) \, w_j, \tag{5.1}$$

where j denotes the bin number of the ϕ-acceptance-corrected energy spectrum $F(E_j)$, and E_j and w_j are the center energy and the width of the j-th bin. In the case of the region including zero-degree, the upper limit of pseudorapidity is set as 13 in order to avoid $\Delta\eta$ of infinity, thus $\Delta\eta$=13 - 10.94 is for this case.

The energy dependence of the contribution to the total energy flow is shown in Fig. 5.6 by multiplying the energy to the measured spectra. The geometrical acceptance of each photon spectrum is corrected in Fig. 5.6. Each distribution has their peak in low energy, around 400–600 GeV for 8.66> η >8.52, and the contribution from the energy greater than 2000 GeV is relatively negligible. There is a clear trend that the contribution of the high energy photon becomes smaller as the pseudorapidity η goes smaller. Since the peak of the energy flow is expected to be around η =7–8, the yield of $\eta > 10.94$ is smaller than the other η regions.

Y_i is calculated by simple integration of the spectra which have the energy thresholds due to the constraints of the experiment as discussed in Sec. 4.1.2. Therefore, the calculated energy flows miss the contribution below the energy thresholds, of which fraction depends on η. It is needed to extrapolate the spectra below the energy threshold of 200 GeV in order to directly compare the models. Extrapolation itself,

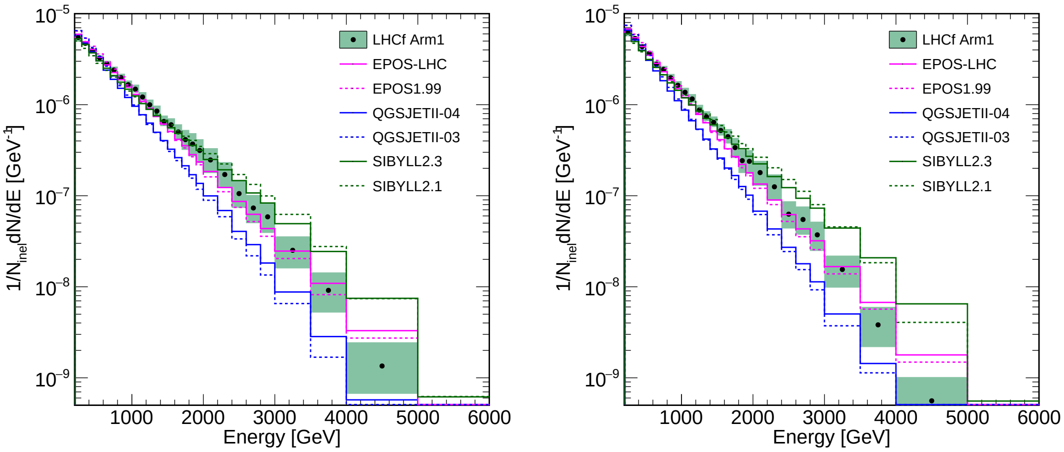

(a) 9.22> η >8.99 (b) 8.99> η >8.81

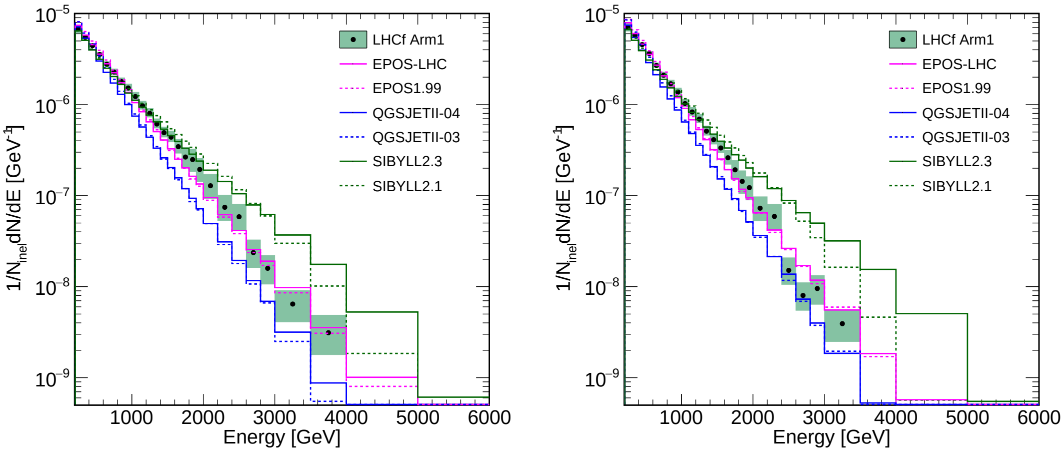

(c) 8.81> η >8.66 (d) 8.66> η >8.52

Figure 5.3: The Arm1 photon spectra at each η region, a) 9.22> η >8.99, b) 8.81> η >8.66, and c) 8.66> η >8.52, and comparison with the models. Green filled area of data points represents the estimated systematic errors, while statistical errors are not shown for model predictions as they are negligible.

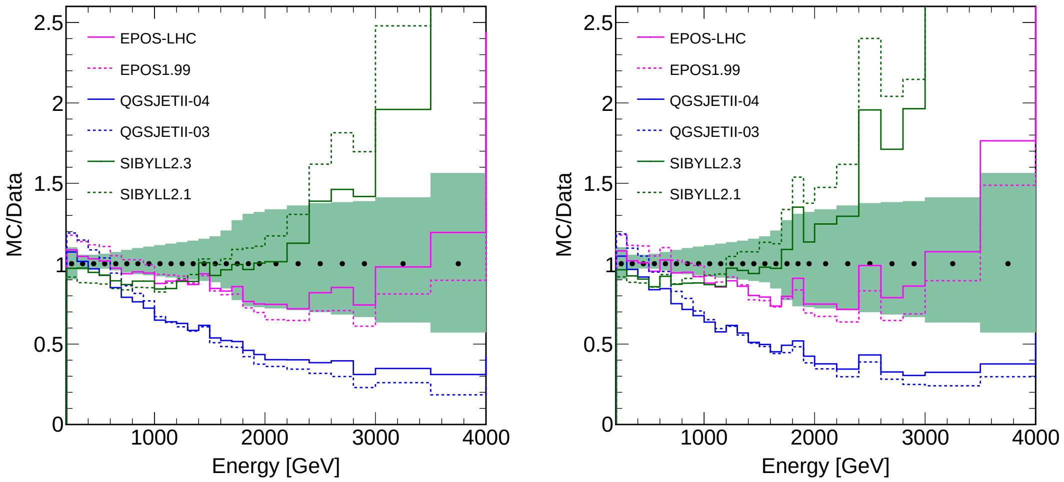

(a) 9.22> η >8.99 (b) 8.99> η >8.81

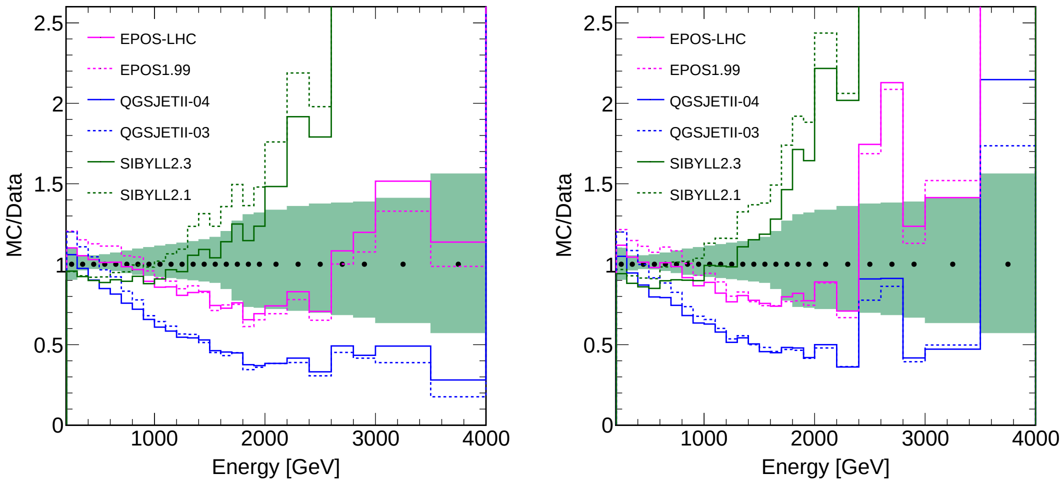

(c) 8.81> η >8.66 (d) 8.66> η >8.52

Figure 5.4: Model predictions of the photon spectra normalized to the LHCf-Arm1 spectrum. Each plot represents a) 9.22> η >8.99, b) 8.81> η >8.66, and c) 8.66> η >8.52. Green filled area with the data points represents the systematic errors. In order to understand the difference in the low energy region, the ratios above 4000 GeV are not displayed in the plots.

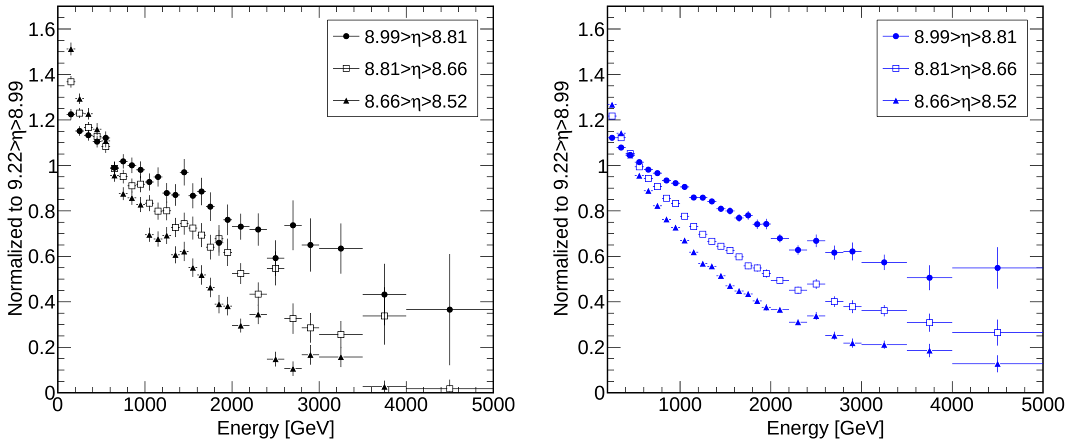

(a) LHCf Arm1 (b) QGSJETII-04

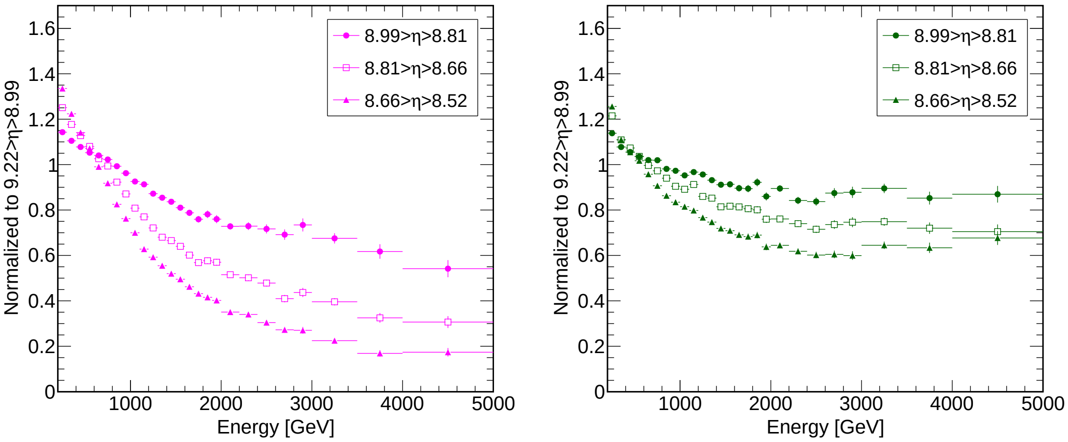

(c) EPOS-LHC (d) SIBYLL2.3

Figure 5.5: Comparison of the spectral shapes of a) LHCf Arm1, b) QGSJETII-04, c) EPOS-LHC, and d) SIBYLL2.3. Each spectra of 9.22> η >8.99, 8.81> η >8.66, and 8.66> η >8.52 are normalized to the one in 9.22> η >8.99. Only statistical errors are shown.

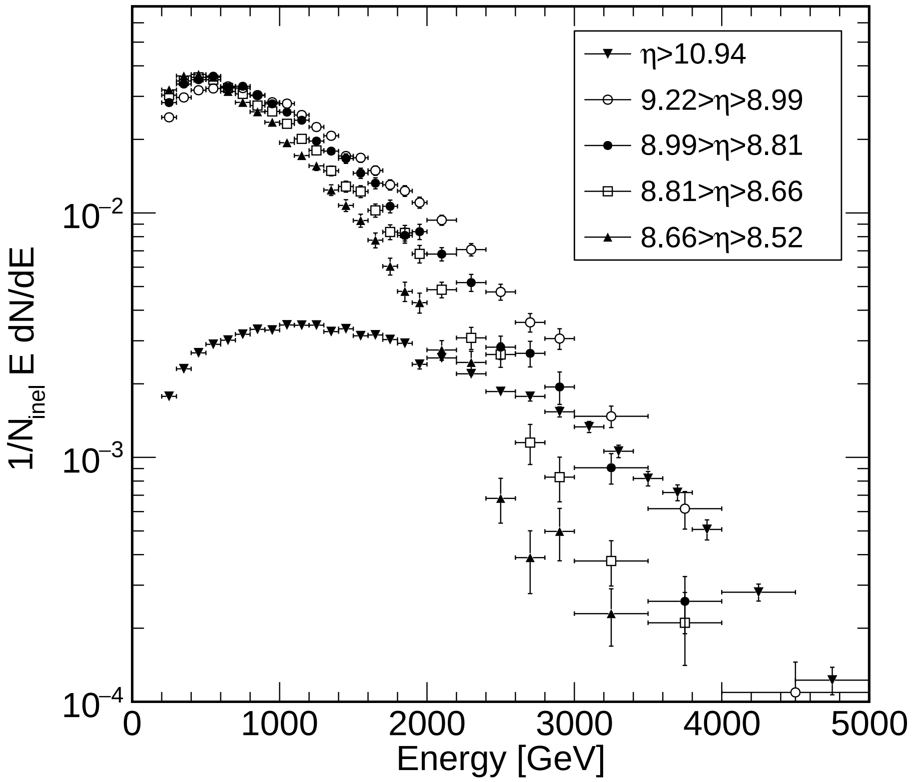

Figure 5.6: Contributions of each energy bin in the energy flow calculation. The measured photon spectra are multiplied with energy at each bin. Geometrical acceptances, $\Delta\phi = 180°$ and $\Delta\phi = 20°$ for the 20 mm and 40 mm calorimeters, respectively, are corrected.

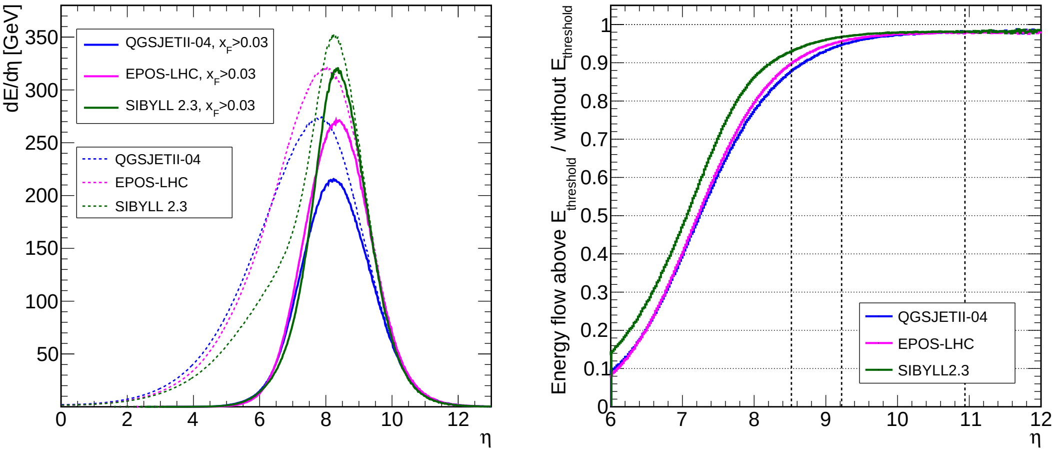

(a) With/without the threhold

(b) Efficiency

Figure 5.7: a) Energy flow distributions with or without the energy threshold at 13 TeV collisions. Broken and solid lines correspond to the distributions with or without the energy threshold. b) Efficiency defined as the fractional energy above thresholds with respect to the energy without the threshold.

Table 5.1: Efficiency of the energy flow measurement assuming the energy threshold of 200 GeV at $\sqrt{s}$ =13 TeV. The efficiency [%] is defined as fractional energy above the threshold with respect to the energy without the threshold at the certain region.

η range	QGSJETII-04	EPOS-LHC	SIBYLL2.3
η >10.94	98.1	98.0	96.4
9.22> η >8.99	93.9	95.0	96.4
8.99> η >8.81	92.2	93.7	95.5
8.81> η >8.66	90.5	92.3	94.6
8.66> η >8.52	88.8	90.7	93.6

however, becomes model dependent.

Figure 5.7(a) shows the energy flow distributions with or without the energy threshold. The efficiency can be defined as the fractional energy above the thresholds with respect to the energy without the threshold. The η dependence of the efficiencies for each model is shown in Fig. 5.7(b). The efficiencies dramatically decrease in lower η region, while two distributions are getting closer to each other in the higher η region for those three models. According to the obtained results in Fig. 5.7, we can evaluate the model-dependent efficiencies for each rapidity region. Within the range used in the study, $\eta > 8.52$, each interaction model predicts high efficiency, roughly 90 % with the energy threshold of 200 GeV, i.e. x_F=0.031. Model-dependent efficiencies at each rapidity region are summarized in Tab. 5.1. The factors to correct the low-energy photons are defined by using the average of the efficiencies calculated by the three models for each η region. The correction factors are 1.023, 1.052, 1.066, 1.081, and 1.098 for η >10.94, 9.22> η >8.99, 8.99> η >8.81, 8.81> η >8.66, and 8.66> η >8.52, respectively. The difference of the efficiencies among the models is considered as the systematic uncertainty of this correction for each η region.

5.1.4 Systematic uncertainties

The systematic uncertainty of the energy flow at the i-th pseudorapidity region, σ_i, is estimated by calculating the contribution of each systematic uncertainty independently. Systematic uncertainties we discuss here are the ones arising from energy scale, PID correction, beam center, multi-hit selection, unfolding, and luminosity as previously summarized in Sec.4.5.6. All of the systematic effects on the spectra are considered as bin-by-bin correlated, but independent each other contribution. We obtain the j-th contribution of the systematic uncertainty of the energy flow, σ_i^j, by shifting the observed photon spectra by upper and lower bands of the estimated systematic uncertainties at each energy bin. We assign the error in an alternative way for the energy scale which is the most influential uncertainty. The uncertainty on the energy flow from the energy scale is estimated by calculating the energy flows with the spectra having ±3.4 %-shifted energy scales.

Figure 5.8 shows each contribution of the uncertainty on the energy flow measurement. The total systematic uncertainty for each η region, σ_i, is calculated by adding all the errors quadratically. The uncertainty from the low-energy correction, which is already introduced in Sec. 5.1.3, is also considered and quadratically added. In Fig. 5.8 *Total* includes the contribution from the low-energy correction. Total systematic uncertainties are roughly ±10 % for the four η regions in $9.22 > \eta > 8.52$, while slightly larger uncertainty is obtained in $\eta > 10.94$.

5.2 Results

5.2.1 Comparison with the post-LHC model predictions

Measured photon energy flow in p–p $\sqrt{s}$ =13 TeV and the comparison with the model predictions are shown in Fig. 5.9. Energy flows are calculated above the energy threshold of 200 GeV corresponding $x_F = 0.031$ for both data and model predictions in Fig. 5.9. EPOS-LHC and SIBYLL2.3 are consistent with the observed results in the four η ranges, which are close to the peak of the energy flow distribution, within the estimated systematic errors. As is expected by the comparison between the pre-LHC and the post-LHC model predictions with the energy spectra in Fig. 5.4, the pre-LHC models give larger energy flow than those of the post-LHC models due to the difference in the energy spectra roughly below 2000 GeV.

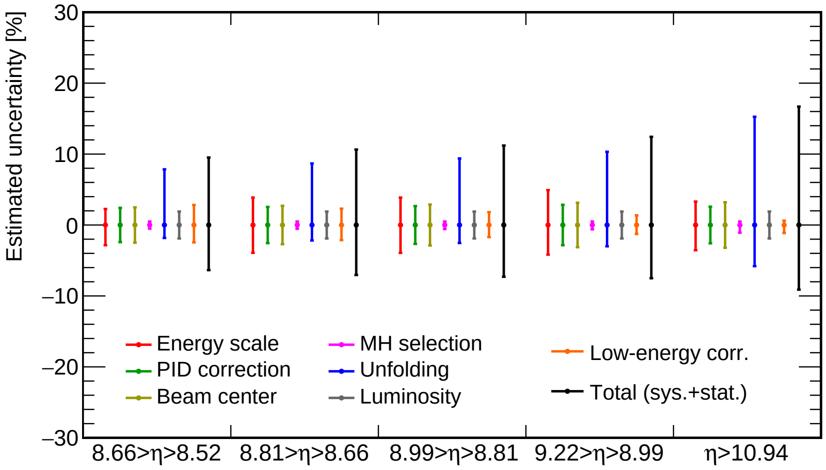

Figure 5.8: Estimated systeamtic uncertainties in each η region. *Total* is calculated by adding each uncertainty quadratically.

Table 5.2: The measured energy flows [GeV/$\Delta\eta$] and the model predictions. The energy flows are calculated above 200 GeV.

η range	LHCf Arm1	QGSJETII-04	EPOS-LHC	SIBYLL2.3
(13.0)> η >10.94	$4.1^{+0.7}_{-0.4}$	3.2	3.3	2.8
9.22> η >8.99	$219.3^{+27.1}_{-15.2}$	154.2	202.9	216.9
8.99> η >8.81	$252.9^{+28.0}_{-16.2}$	176.1	233.6	257.2
8.81> η >8.66	$269.8^{+27.4}_{-15.6}$	192.2	252.1	286.2
8.66> η >8.52	$279.0^{+25.4}_{-14.6}$	203.7	264.3	304.1

The calculated energy flow for the experimental results and corresponding model predictions are summarized in Tab. 5.2. The predictions of QGSJETII-04 are approximately 30 % smaller, ranging 27–32 %, than the measured results within all the η ranges. Although the contribution of the lower energy photons on the energy flow is the largest among three models as shown in Tab. 5.1, the difference of the efficiencies are just a level of few percent as discussed in Sec. 5.1.3 and thus the shortage of the energy flow is not able to be explained by the energy threshold.

The correction of inefficiency for the low energy photons is applied to the energy flow distribution, and the result is shown in Fig. 5.10. The peaks of the energy flow distributions of the model predictions slightly shift toward smaller η comparing to Fig. 5.9 because the contribution of lower energy photons of the energy flow increases in small η. The prediction of SIBYLL2.3 is consistent with the obtained data results in $9.22 > \eta > 8.52$. EPOS-LHC predicts slightly smaller energy flow than the observed

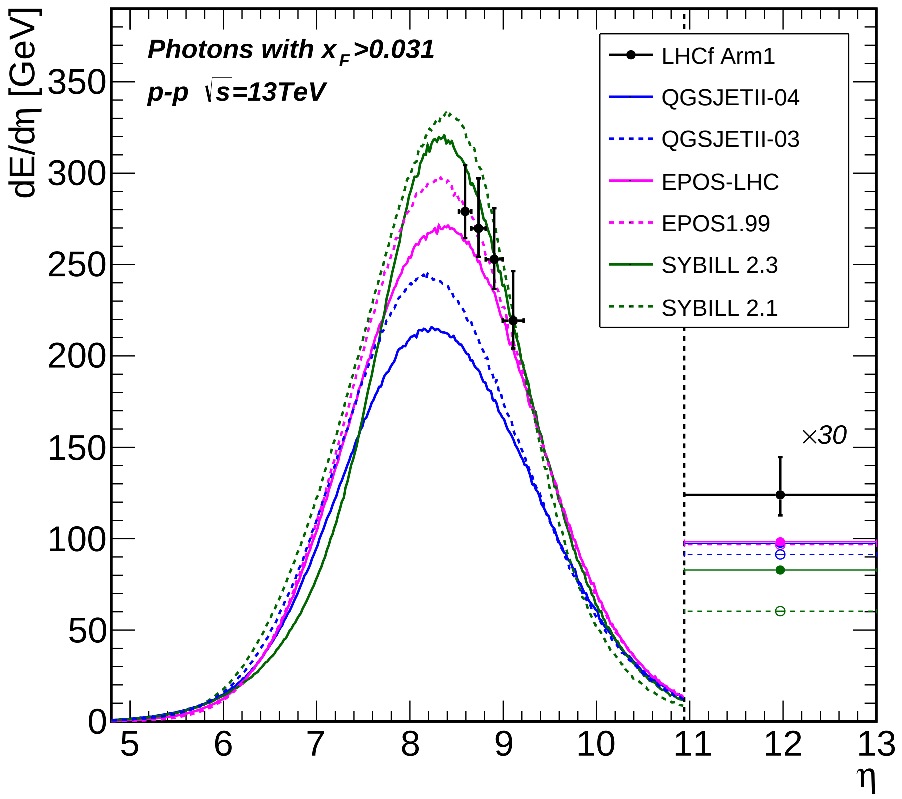

Figure 5.9: Measured photon energy flow and MC predictions in p–p $\sqrt{s}$=13 TeV. MC predictions are shown in colored lines, while measured data at each η region are shown in black points. Measured energy flows are plotted with estimated systematic and statistical errors. In the region of η >10.94, $\Delta\eta$ is assumed as $\Delta\eta$ =13-10.94.

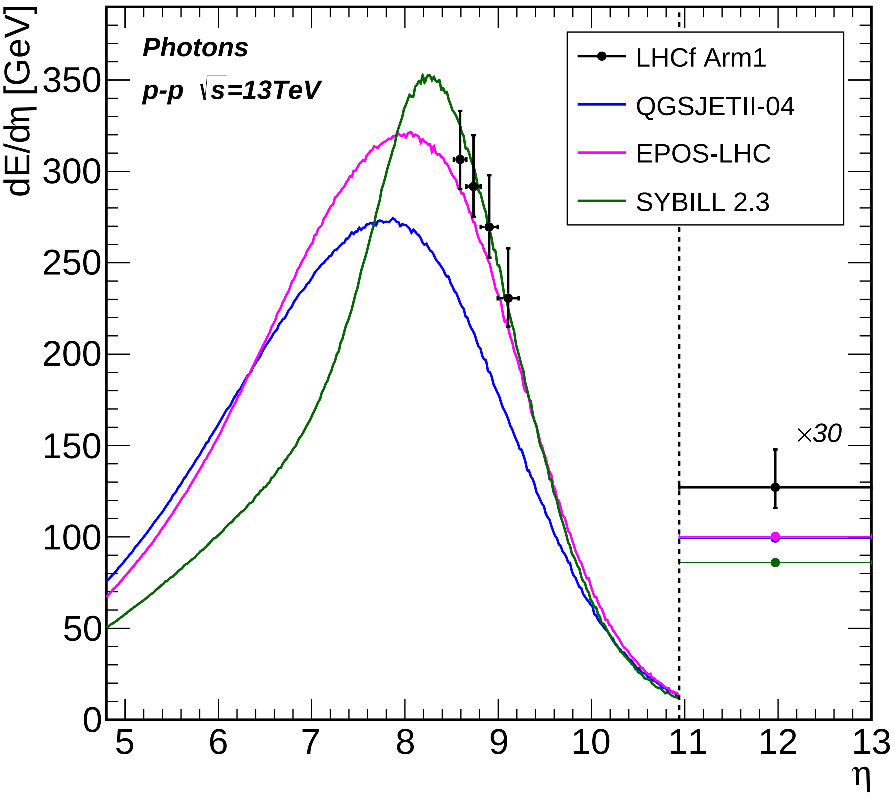

Figure 5.10: Measured photon energy flow after the correction for inefficiency of the low energy photons and corresponding MC predictions in p–p $\sqrt{s}$=13 TeV. MC predictions are shown in colored lines, while measured data at each η region are shown in black points. Measured energy flows are plotted with the estimated systematic and statistical errors. In the region of η >10.94, $\Delta\eta$ is assumed as $\Delta\eta$ =13-10.94.

results by 5–8 %. No models are consistent with the measured data at the highest η bin, $13 > \eta > 10.94$. The measured data results indicate that the photon energy flow by QGSJETII-04 is smaller in all measured η regions. The lack of the photon energy flow of QGSJETII-04 is a level of 30 %. The corrected results and the model predictions are summarized in Tab. 5.3.

5.3 Discussion

In this chapter, we summarize the obtained results of the very-forward photon production in terms of the energy spectrum and the energy flow measurement and the corresponding model predictions. Since the agreement of the results obtained with the Arm1 and the Arm2 detectors has been already confirmed in Sec.4.6.1, the discussion here is built on the obtained results of the wide η acceptance calculated with the Arm1 detector in this chapter. In order to consider the impact of this work

Table 5.3: The measured energy flows [GeV/$\Delta\eta$] and the model predictions corrected for the energy threshold.

η range	LHCf Arm1	QGSJETII-04	EPOS-LHC	SIBYLL2.3
(13.0)> η >10.94	$4.2^{+0.7}_{-0.4}$	3.3	3.4	2.9
9.22> η >8.99	$230.6^{+27.3}_{-15.5}$	164.2	213.6	225.0
8.99> η >8.81	$269.6^{+28.3}_{-16.8}$	191.0	249.3	269.3
8.81> η >8.66	$291.7^{+26.5}_{-16.1}$	212.4	273.1	302.5
8.66> η >8.52	$306.5^{+26.5}_{-16.1}$	229.4	291.4	324.9

on UHECRs measurement, we discuss the influence of the re-tuning of the existing models with the very-forward photon measurement on the description of the shower development such as X_{max}.

The difference of the photon production in the very-forward region between the pre/post-LHC model is seen in the energy region of less than 1000 GeV. The post-LHC models predict less photon yield there compared to that of the pre-LHC models in the lowest energy bins, and the obtained results support the predictions of the post-LHC models. No significant differences between the pre/post-LHC models are seen in the other high energy regions. All the predictions of the photon energy flow from the pre-LHC models exceed that of the post-LHC model within the η range of this work because the contribution of lower energy photons dominates a large fraction of the energy flow.

If one integrates the total photon energy flow in a hadron collision, QGSJETII-04, EPOS-LHC, and SIBYLL2.3 return 1083.6 GeV, 1191.2 GeV, and 1030.4 GeV, respectively. QGSJETII-04 particularly decreases its photon yield in the very-forward region, $\eta > 8.52$, approximately 30 % lower than EPOS-LHC and SIBYLL. Moreover, the spectral shape predicted by QGSJETII-04 is the softest among the three models. Such features of QGSJETII-04 is well consistent with shallow shower development as introduced in Fig. 1.7. The experimental results disfavor the behavior of QGSJETII-04, the modest photon energy flow and the soft spectral shape at the very-forward region.

SIBYLL2.3 has the hardest spectral shape among the three models, and the η-dependence of the spectral shape is very small. This can be explained by the high energy photons at high p_T up to about 3 GeV as shown in Fig. 5.2, which is unique for SIBYLL2.3. In addition to the very-forward photons which carry the large fraction of the total energy flow, a hard spectrum in the very-forward region explains the slowest shower development by SIBYLL2.3 as shown in Fig. 1.7.

The obtained results of the photon energy flow give the best agreement with SIBYLL2.3 around the peak of the energy flow distribution for $9.22 > \eta > 8.52$ as discussed in Fig. 5.10, while SIBYLL2.3 predicts 30 % lower at $\eta > 10.94$. The CASTOR calorimeter of the CMS experiment has reported the EM energy spectrum in $6.6 > \eta > 5.5$ at 13 TeV [64]. Their result indicates that SIBYLL2.3 underestimates EM energy flow in $6.6 > \eta > 5.5$. Therefore, the unique sharp peak of the energy flow distribution predicted by SIBYLL2.3 is perhaps unlikely. Furthermore, our work strongly disfavors the hard spectra and the small η-dependence of the spectral shape of SIBYLL2.3. If SIBYLL2.3 is re-tuned to reproduce the obtained results here, the prediction of X_{max} is expected to be smaller, thus uncertainty in X_{max} by the model predictions becomes improved.

The predictions of EPOS-LHC reproduce well the measured results both for the spectral shapes and for the energy flow in the very-forward region. Especially, EPOS-LHC succeeds to reproduce the measured spectra up to around 4000 GeV considering the systematic uncertainty. The agreement of the spectra leads good agreement of the energy flow as well.

The features of the photon production, especially the energy flow and the spectral shape in the very-forward region, from QGSJETII-04 and SIBYLL2.3 explain qualitatively their shallow and deep shower development, respectively. This work remarks that ambiguity of the model predictions on X_{max} measurement is expected to be reduced after the further re-tuning of the models for very forward rapidity region, the second generation of the post-LHC models, using the observed results of the photon production studied in this work. Constraining the shallow development predicted by QGSJETII-04 leads a picture of UHECRs as not protonic, but light composition.

Chapter 6

Conclusion

The LHC have proved its capability to reduce the uncertainty on the mass composition measurement by the hadronic interaction models re-tuned with the data observed at the LHC. There still remains critical uncertainty between even post-LHC model predictions. The very-forward measurement at the LHC gives us promising data to improve the reliability of the hadronic interaction models used in the air shower experiments because the phase space of the very-forward region is essentially relevant to the air shower development.

The upgraded LHCf detectors have been developed by adopting the Gd_2SiO_5 (GSO) scintillator, which is known as one of the best scintillators for radiation tolerance, to treat high radiation dose at the very-forward region in p–p $\sqrt{s}$ =13 TeV. After the dedicated beam tests at HIMAC and SPS for the calibration and the performance studies, we have confirmed that the upgraded detectors meet the requirement for the photon measurement having the energy and position resolutions of 2 % and better than 100 μm for 200 GeV electrons, respectively. The LHCf experiment has accomplished the measurement of the p–p 13 TeV collisions in the dedicated runs on 8–13th June 2015.

In Chap. 4, the inclusive photon spectra at $\eta > 10.94$ and $8.99 > \eta > 8.81$ are calculated by the LHCf Arm1 and Arm2 detectors independently. The spectra of Arm1 and Arm2 agree with each other within the estimated systematic uncertainty, and the combined spectra of Arm1 and Arm2 are compared with the MC predictions. For both $\eta > 10.94$ and $8.99 > \eta > 8.81$, EPOS-LHC and PYTHIA8.212 show good agreement, compatible with the systematic uncertainty, below 3000 GeV. The LHCf data disfavors softer and harder spectral shapes of QGSJETII-04 and DPMJET3.06, respectively, for both regions. SIBYLL2.3 underestimates and overestimates the photon production in $\eta > 10.94$ and in $8.99 > \eta > 8.81$, respectively.

Unlike the previous photon analyses in $\sqrt{s}$ =0.9–7 TeV, the obtained data at η in $\sqrt{s}$ =13 TeV covers a large fraction of the energy flow. The photon energy flow distribution has its peak at η =7–8, thus a large fraction of the flow concentrates on the very-forward region where LHCf covers. Therefore, in Chap. 5, we focused on the photon production in terms of the energy flow into the EM component of the hadron collisions. This is the first attempt to verify the photon energy flow at the peak of its η-distribution in $\sqrt{s}$ =13 TeV at the LHC. Simulation studies indicate that the features of each interaction model seen in the photon energy flow in the very-forward region can explain the difference of the shower development qualitatively.

In addition to the η regions studied in Chap. 4, the inclusive photon spectra in $9.22 > \eta > 8.99$, $8.81 > \eta > 8.66$, and $8.66 > \eta > 8.52$ are calculated with the Arm1 detector in order to cover the wide η region around a peak of the energy flow distribution. Pseudorapidity dependence of the photon energy flow at five η regions within $9.22 > \eta > 8.52$ and $\eta > 10.94$ is examined by calculating the differential photon energy flows using the obtained photon spectra.

In $9.22 > \eta > 8.52$, EPOS-LHC shows good agreement with the measured differential energy flows, while it is 5–8 % lower than the measured energy flows. The modest photon energy flow of QGSJETII-04 is disfavored by the measured results. On the other hand, the observed energy flows are consistent with the prediction of SIBYLL2.3, of which flow particularly concentrates on the very-forward, within the estimated systematic uncertainty. However, the result at $\eta > 10.94$ and the EM energy spectrum in $6.6 > \eta > 5.5$ by CASTOR disfavors such specific distribution. Regarding the spectral shapes, the obtained results disfavor the soft and hard trends of QGSJETII-04 and SIBYLL2.3, respectively, while EPOS-LHC shows a good agreement of the spectral shape with the obtained result. Especially, a weak η-dependence of the spectral shape described by SIBYLL2.3 is strongly disagreed with the results. Therefore, we conclude that EPOS-LHC reproduces well both the spectral shape and the energy flow especially in the very-forward region.

Observed features of the very-forward photon energy spectra and energy flow distributions of QGSJETII-04 and SIBYLL2.3 are qualitatively consistent with their shallow and deep air shower development, respectively. This work remarks that ambiguity of the model predictions in X_{max} measurement is expected to be reduced after the further re-tuning of the models, the second generation of the post-LHC models, using the observed results of the photon production in the very forward region. Constraining the shallow development predicted by QGSJETII-04 leads a picture of UHECRs as not protonic, but light composition.

Bibliography

[1] K.A. Olive et al. (Particle Data Group), Chin. Phys. C, **38**, 090001 (2014).

[2] M. Ackermann et al., *"Detection of the Characteristic Pion-Decay Signature in Supernova Remnants"*, Science **339** (2013).

[3] J. Hörandel, *"A review of experimental results at the knee"*, Journal of Physics Conf. Ser. **47** (2006) 41–50.

[4] M. Takeda, et al., *"Extension of the Cosmic-Ray Energy Spectrum beyond the Predicted Greisen-Zatsepin-Kuz'min Cutoff"*, Phys. Rev. Lett., **81** (1998) 1163.

[5] T. Abu-Zayyad et al., *"The surface detector array of the Telescope Array experiment"*, Nucl. Instrum. Meth. A **689** (2012); , *"New air fluorescence detectors employed in the Telescope Array experiment"*, Nucl. Instrum. Meth. A **676** (2012).

[6] J. Abraham et al. (Pierre Auger Collaboration), *"Properties and performance of the prototype instrument for the Pierre Auger Observatory"*, Nucl. Instrum. Meth. A **523** (2004); *"Trigger and Aperture of the Surface Detector Array of the Pierre Auger Observatory"*, Nucl. Instrum. Meth. A **613** (2010).

[7] T. Abu-Zayyad et. al, *"THE COSMIC-RAY ENERGY SPECTRUM OBSERVED WITH THE SURFACE DETECTOR OF THE TELESCOPE ARRAY EXPERIMENT"*, Astrophys. J. **768** (2013).

[8] Pierre Auger Collaboration, *"Measurement of the energy spectrum of cosmic rays above* 10^{18} *eV using the Pierre Auger Observatory"*, Phys. Lett. B **685** (2010) 239-246.

[9] G.T. Zatsepin, V.A. Kuzmin, *"Upper limit of the spectrum of cosmic rays"*, JETP Lett. **4** (1966) 78-80.

[10] K. Greisen, *"End to the Cosmic-Ray Spectrum?"*, Phys. Rev. Lett. **16** (1966) 748.

[11] A.A. Penzias and R. Wilson, *"A Measurement of Excess Antenna Temperature at 4080 Mc/s"*, Astrophys. J. **142** (1965) 419-412.

[12] K.H. Kampert, and M. Unger, *"Measurements of the cosmic ray composition with the air shower experiments"*, Astroparticle Physics **35** (2012) 660-678.

[13] CORSIKA homepage, https://www.ikp.kit.edu/corsika/

[14] R.U. Abbasi et al., *"Study of Ultra-High Energy Cosmic Ray composition using Telescope Array' s Middle Drum detector and surface array in hybrid mode"*, Astroparticle Physics **64** (2015) 49-62.

[15] A. Aab et al., *"Depth of maximum of air-shower profiles at the Pierre Auger Observatory. I. Measurements at energies above* $10^{17.8}$ *eV"*, Phys. Rev. D **90** 122005 (2014).

[16] R. Abbasi et al., *“Report of the Working Group on the Composition of Ultra High Energy Cosmic Rays”*, JPS Conf. Proc. **9** (2016) 010016.

[17] D. Allard, *“Extragalactic propargation of ultrahigh energy cosmic-rays”*, Astroparticle Physics **39–40** (2012) 33-43.

[18] R. P. Feynman, *“Very High-Energy Collisions of Hadrons”*, Phys. Rev. Lett. **23** (1969) 1415.

[19] W. Thomé et al., *“Charged particle multiplicity distributions in pp collisions at ISR energies”*, Nucl.Phys. B **129** (1977) 365.

[20] T. Stanev, *“High Energy Cosmic Rays”*, Springer (2004).

[21] D. Cline, F. Halzen, and J. Luthe, *“High-Transverse-Momentum Secondaries and Rising Total Cross Sections in Cosmic-Ray Interactions”*, Phys. Rev. Lett. **31** (1973) 491.

[22] T.K Gaisser, and F. Halzen, *““Soft”Hard Scattering in the Telaelectronvolt Range”*, Phys. Rev. Lett. **16** (1973) 54.

[23] V.N. Gribov, *“A Reggeon Diagram Technique”*, JETP **26** (1968) 414.

[24] T. Pierog, Iu. Karpenko, J. M. Katzy, E. Yatsenko, and K. Werner, *“EPOS LHC: Test of collective hadronization with data measured at the CERN Large Hadron Collider”*, Phys. Rev. C **92** (2015) 034906.

[25] S. Ostapchenko, *“Monte Carlo treatment of hadronic interactions in enhanced Pomeron scheme: QGSJET-II model”*, Phys. Rev. D **83** (2011) 014018.

[26] E.-J Ahn, R. Engel, T.K. Gaisser, P. Lipari, and T. Stanev, *“Cosmic ray interaction event generator SIBYLL 2.1”*, Phys. Rev. D **80** (2009) 094003.

[27] F. W. Bopp, J. Ranft, R. Engel, and S. Roesler, *“Antiparticle to particle production ratios in hadron-hadron and d-Au collisions in the DPMJET-III Monte Carlo model”*, Phys. Rev. C **77** (2008) 014904.

[28] T. Sjöstrand, et al., *“An introduction to PYTHIA 8.2”*, Comput. Phys. Commun. **191** (2015) 159177.

[29] H.J. Drescher, M. Hladik, S. Ostapchenko, T. Pierog, K. Werner, *“Parton-based Gribov–Regge theory”*, Phys. Rept. **350** (2001) 93-289.

[30] R. Ulrich, R. Engel, and M. Unger, *“Hadronic multiparticle production at ultrahigh energies and extensive air showers”*, Phys. Rev. D **83** (2011) 054026.

[31] T. Pierog, *“Review of Model Predictions for Extensive Air Showers”*, 2016 International Conference on Ultra-High Energy Cosmic Rays, Kyoto Japan, 11-14 Oct. (2016).

[32] F. Riehn, R. Engel, A. Fedynitch, T. K. Gaisser, T. Stanev, *“A new version of the event generator Sibyll”*, arXiv:1510.00568.

[33] The ATLAS Collaboration, *“The ATLAS Experiment at the CERN Large Hadron Collider”*, JINST **3** (2008) S08003.

[34] The CMS Collaboration, *“The CMS experiment at the CERN LHC”*, JINST **3** (2008) S08004.

[35] The LHCf collaboration, *“The LHCf detector at the CERN Large Hadron Collider”*, JINST **3** (2008) S08006.

[36] The LHC Foward Physics Working Group *"LHC Foward Physics"*, CERN-PH-LPCC-2015-001 (2015).

[37] The LHCf collaboration, *"Measurement of zero degree single photon energy spectra for* $\sqrt{s}$ *= 900 GeV proton-proton collisions at LHC"*, Phys. Lett. B **715** (2012) 298.

[38] O. Adriani et al., *"Measurement of zero degree single photon energy spectra for* $\sqrt{s}$ *= 7 TeV proton-proton collisions at LHC"*, Phys. Lett. B **703** (2011) 128.

[39] The LHCf collaboration, *"Measurement of forward neutral pion transverse momentum spectra for*$\sqrt{s}$ *= 7 TeV proton-proton collisions at the LHC"*, Phys. Rev. D **86** (2012) 092001.

[40] The LHCf collaboration, *"Transverse-momentum distribution and nuclear modification factor for neutral pions in the forward-rapidity region in proton-lead collisions at* $\sqrt{s_{NN}}$*=5.02 TeV"*, Phys. Rev. C **89** (2014) 065209.

[41] The LHCf collaboration, *"Measurements of longitudinal and transverse momentum distributions for neutral pions in the forward-rapidity region with the LHCf detector"*, Phys. Rev. D **94** (2016) 032007.

[42] K. Kawade et al., *"Study of radiation hardness of* Gd_2SiO_5 *scintillator for heavy ion beam"*, JINST **6** (2011) T09004.

[43] L. Evans and P. Bryant, *"LHC Machine"*, JINST **3** (2008) S08001.

[44] The LHCf collaboration, *"Measurement of very forward neutron energy spectra for 7 TeV proton-proton collisions at the Large Hadron Collider"*, Phys. Lett. B **750** (2015) 360-366.

[45] M. Tanaka et al., *"Applications of cerium-doped gadolinium silicate* Gd_2SiO_5*:Ce scintillator to calorimeters in high-radiation environment"*, Nucl. Instrum. Meth. A **404** (1998) 283.

[46] T. Suzuki et al., *"Performance of very thin* Gd_2SiO_5 *scintillator bars for the LHCf experiment"*, JINST **8** (2013) T01007.

[47] ATLAS Collaboration, *"Zero Degree Calorimeters for ATLAS"*, CERN-LHCC-2007-01, LHCC I-016 (2007).

[48] O. Adriani et al., *"The construction and testing of the silicon position sensitive modules for the LHCf experiment at CERN"*, JINST **5** (2010) P01012.

[49] MIDAS homepage, https://midas.triumf.ca/MidasWiki/index.php/Main_page.

[50] L. Bonechi et al., *"Development of the ADAMO detector: test with cosmic rays at different zenith angles"*, Proc. of 29th Int. Cosmic Ray Conf. Pune **9** (2005) 283.

[51] Cosmos home page, http://cosmos.n.kanagawa-u.ac.jp/cosmosHome/index.html

[52] EPICS home page, http://cosmos.n.kanagawa-u.ac.jp/EPICSHome/index.html

[53] G. Antchev et al. (TOTEM Collaboration), *"Luminosity-Independent Measurement of the Proton-Proton Total Cross Section at* $\sqrt{s}$*=8 TeV"*, Phys. Rev. Lett. **111** (2013) 012001.

[54] ATLAS collaboration, *"Luminosity determination in pp collisions at* $\sqrt{s}$*= 8 TeV using the ATLAS detector at the LHC"*, arXiv:1608.03953v1 (2016).

[55] A.A. Lednev, *"Electron shower transverse profile measurement"*, Nucl. Instrum. Meth. A **366** (1995).

[56] M.Morhac et al., *"Background elimination methods for multidimensional coincidence gamma-ray spectra"* Nucl. Instrum. and Meth. A **401** (1997) 113-132.

[57] I. Antcheva et al.,*"ROOT – A C++ framework for petabyte data storage, statistical analysis and visualization"*, Comp. Phys. Commun. **180** (2009) 2499-2512, https://root.cern.ch/

[58] G. D'Agostini, *"A multidimensional unfolding method based on Bayes' theorem"*, Nucl. Instrum. Methods Phys. Res. Sect. A **362** (1995) 292.

[59] T. Adye, *"Unfolding algorithms and tests with using RooUnfold"*, arXiv:1105.1160v1 (2011).

[60] G. D'Agostini, *"Improved iterative Bayesian unfolding"*, arXiv:1010.0632v1 (2010).

[61] G. L. Fogli, E. Lisi, A. Marrone, D. Montanino, and A. Palazzo, *"Getting the most from the statistical analysis of solar neutrino oscillations"*, Phys. Rev. D **66** (2002) 053010.

[62] T. Pierog, C. Baus, R. Ulrich, https://web.ikp.kit.edu/rulrich/crmc.html

[63] Q.D. Zhou et al., *"Monte Carlo study of particle production in diffractive proton-proton collisions at* $\sqrt{s} = 13$ *TeV with the very forward detector combined with central information"*, arXiv:1611.07483

[64] The CMS Collaboration, *"Measurement of the energy distributions in the very forward direction at 13TeV with CMS"*, CMS Physics Analysis Summary CMS PAS FSQ-16-002, 2016.

Acknowledgements

I would like to express my gratitude to my supervisor, Prof. Y. Itow for providing me with this opportunity to study this research, and giving me a lot of useful advice. I would also like to thank Dr. T. Sako and Dr. H. Menjo for taking time to give me many valuable advices, elaborated guidance and helps. They providing me the essential support for this thesis.

I am deeply grateful to Prof. Y. Muraki, Prof. K. Kasahara, Prof. O. Adriani, Prof. A. Tricomi, Prof. R. D’ Alessandro, Prof. K. Masuda, Prof. Y. Matsubara, Dr. L. Bonechi, Dr. M. Bongi, Dr. N. Sakurai, Dr. G. Mitsuka, and other LHCf collaborators to give me useful comments and suggestions. I would also like to thank Dr. A. Tiberio and Dr. E. Berti for very productive days in Firenze. I also show my appreciation to E. Matsubayashi, Q-D. Zhou, M. Ueno, M. Shinoda, K. Sato, and all members in CR lab for meaningful discussion and supports.

A special thanks to my family. Words cannot express how grateful I am to my parents for all of the sacrifices that you have made on my behalf.

Appendix A

All layer of light collection efficiency maps

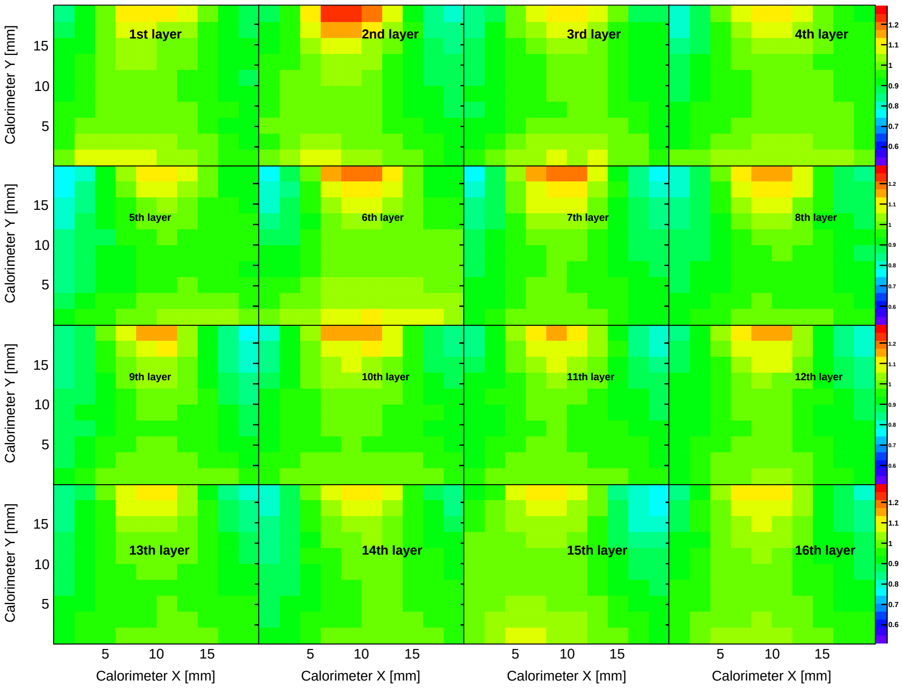

(a) 20 mm tower

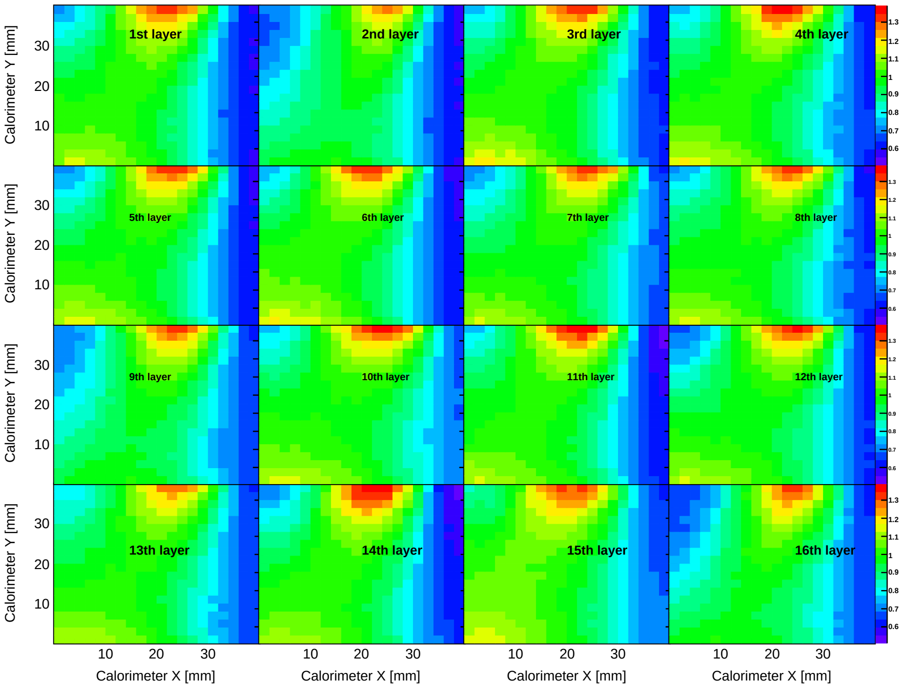

(b) 40 mm tower

Figure A.1: Light collection efficiency maps for the Arm1 a) 20 mm and b) 40 mm calorimeters. The results are based on the data taken at HIMAC.

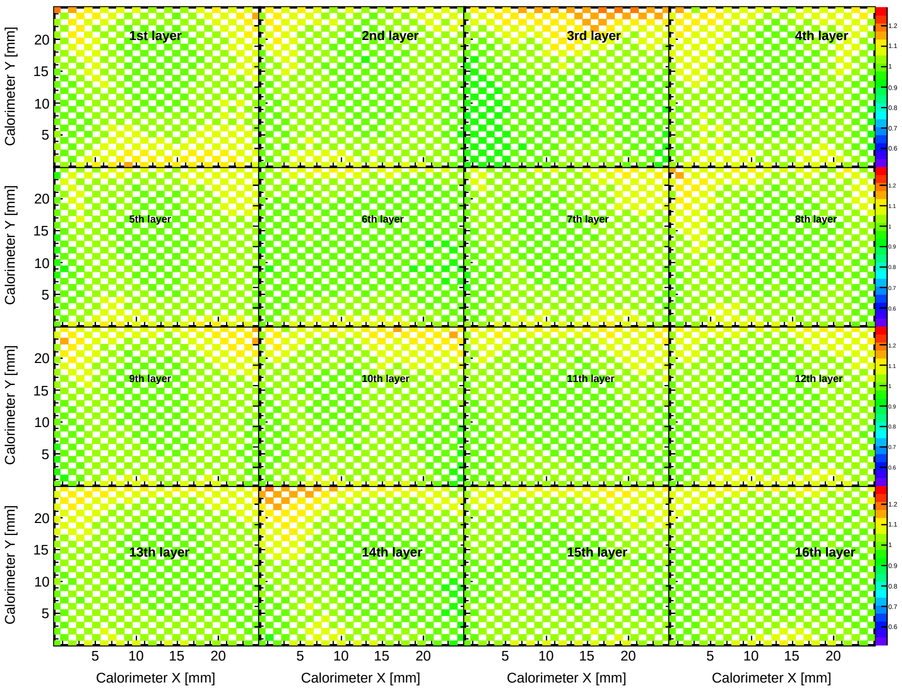

(a) 25 mm tower

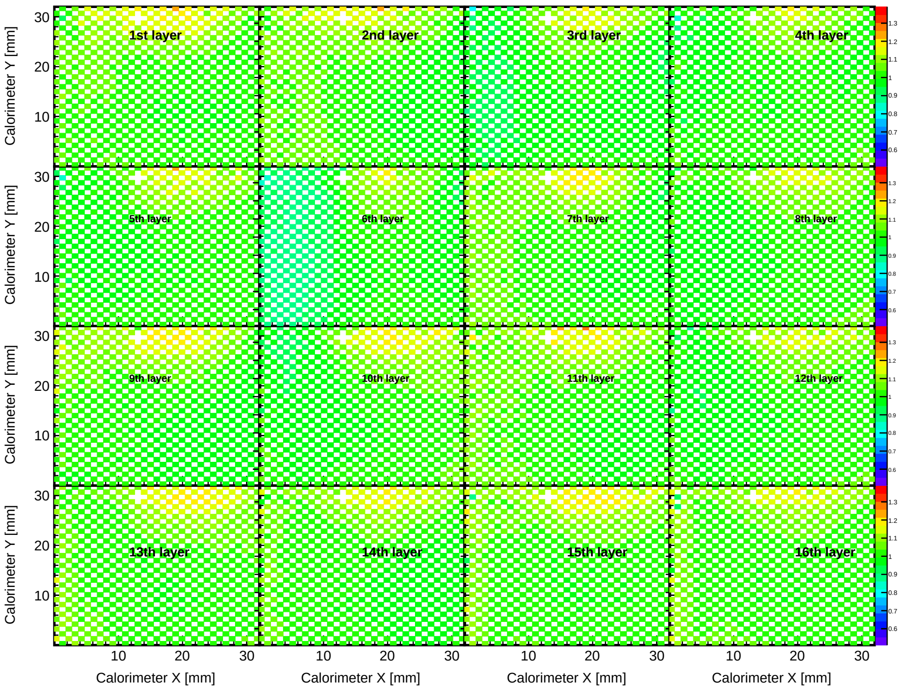

(b) 32 mm tower

Figure A.2: Light collection efficiency maps for the Arm2 a) 25 mm and b) 32 mm calorimeters. The results are based on the data taken at HIMAC.

Appendix B

Systematic uncertainties for the additional acceptace regions

B.1 The energy scale

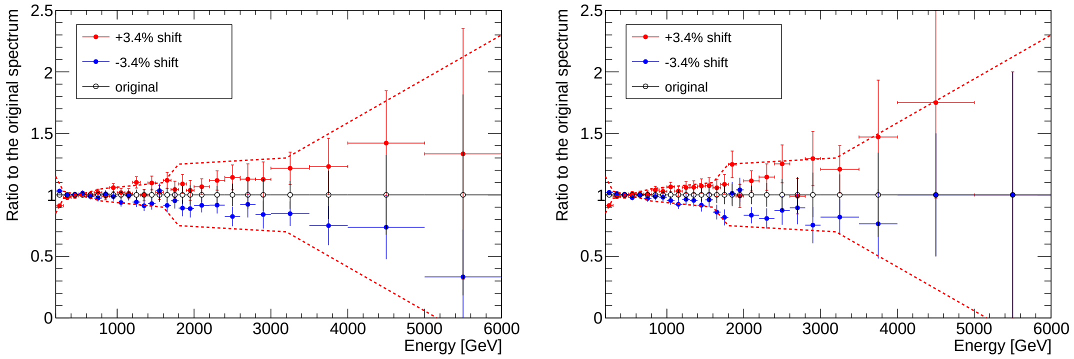

(a) 9.22> η >8.99 (b) 8.99> η >8.81

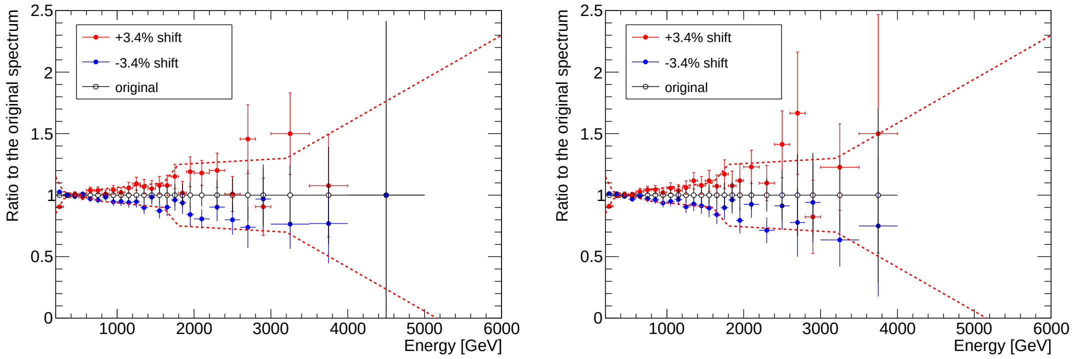

(c) 8.81> η >8.66 (d) 8.66> η >8.52

Figure B.1: Energy scale uncertainty of a) 9.22> η >8.99, b) 8.99> η >8.81, c) 8.81> η >8.66, and d) 8.66> η >8.52. Shown red lines were same as Fig. 4.31.

B.2 Multi-hit correction

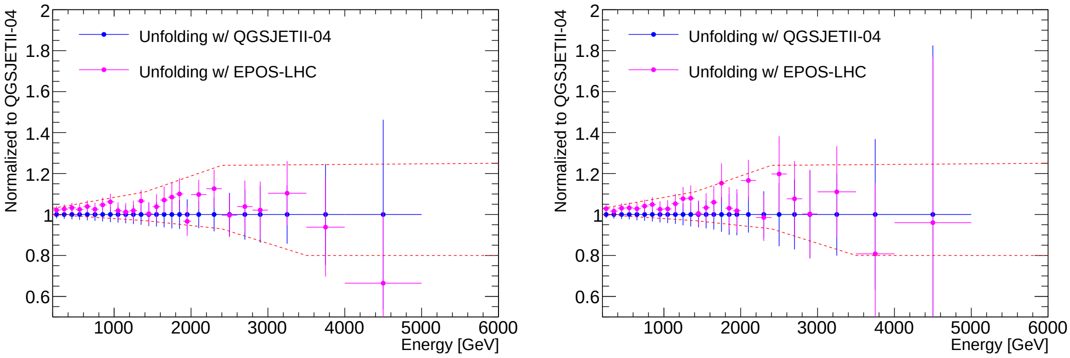

(a) 9.22> η >8.99 (b) 8.99> η >8.81

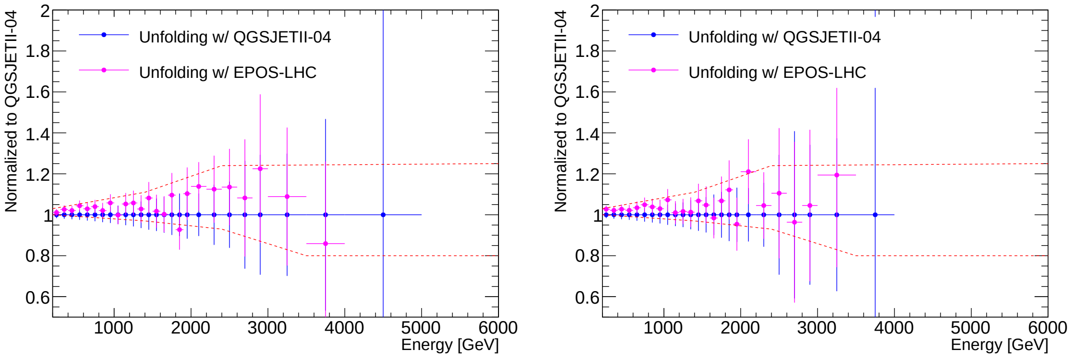

(c) 8.81> η >8.66 (d) 8.66> η >8.52

Figure B.2: Multihit correction uncertainty of a) 9.22> η >8.99, b) 8.99> η >8.81, c) 8.81> η >8.66, and d) 8.66> η >8.52. Shown red lines were same as Fig. 4.31.